THE INFLUENCE OF THERMAL DAMAGE AND PHASE TRANSITION ON IMPACT AND SHOCK SENSITIVITY IN HMX SYSTEMS

by

Nicholas Cummock

A Dissertation

Submitted to the Faculty of Purdue University

In Partial Fulfillment of the Requirements for the degree of

Doctor of Philosophy

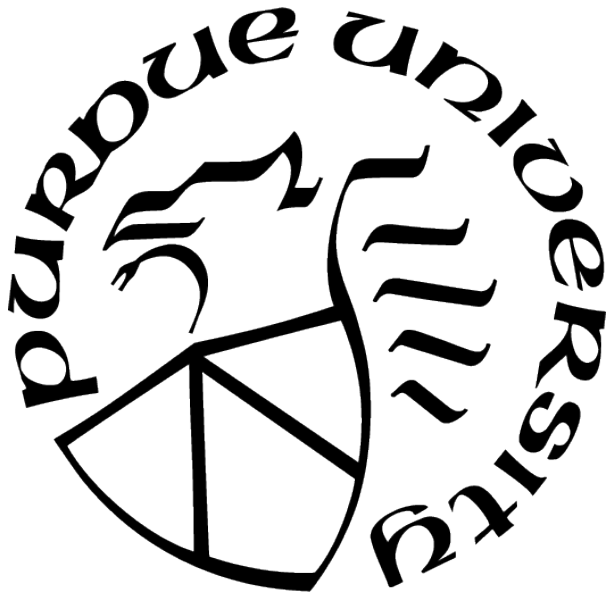

School of Mechanical Engineering

West Lafayette, Indiana

May 2021

THE PURDUE UNIVERSITY GRADUATE SCHOOL
STATEMENT OF COMMITTEE APPROVAL

Dr. Steven F. Son, Chair

School of Mechanical Engineering

Dr. Jeffrey F. Rhoads

School of Mechanical Engineering

Dr. Davin G. Piercey

School of Materials Engineering

Dr. Metin Örnek

School of Mechanical Engineering

Dr. Vasant S. Vuppuluri

School of Mechanical Engineering

Approved by:

Dr. Nicole L. Key

This work is dedicated first and foremost to Brynlee, Benson, and Jett, who provide me a shimmer of light in this sometimes dark, dark world. My intent is to use my experience and education to become a useful enough scientist to earn a decent living and thus have the ability to provide my children with a safe, happy, and memorable childhood.

ACKNOWLEDGMENTS

My Wife deserves particular kudos, as she allowed me the time and provided necessary encouragement, as well as an ear for commiseration when needed. This work could not have been completed without her.

I further would like to acknowledge the help, patience, critiques, and encouragement of my Advisor, Dr. Steve Son. He was particularly supportive when certain others who were supposed to be my mentors turned their backs on me.

Also, my fellow research group peers, which include but were not limited to: David Kittell, who was my first peer mentor, and was a true and caring friend, and an incredibly thorough, intelligent, integrous, and dedicated researcher. Gabriel Montoya was an instant friend caught up in the same web of technical questions and struggles as myself. Vasant Vuppuluri was always, always willing to lend a helping hand. Jesus Mares was often willing to give constructive criticism, technical ideas, and occasionally a well placed word of encouragement. Dakota Scott was always willing to go to Dairy Queen with me, and that was oh so needed. He often lent a breath of fresh air by teaching me about the paper mill, and he quickly learned more about the systems that I originally set out to mentor him in than I myself knew. I miss spending time with Andrew Justice, one of the more charismatic engineers I've encountered. Christian Sorensen knew more about the practical aspects of explosives engineering when he began in our research group than I likely will when I finish my Ph.D., and was always worthwhile to consult on that topic, and perhaps politics. He also designed and built the PDV system, of which I reaped the benefits when I used it for my shock experiments. Alex Casey became a teacher and a friend to both myself and my kids. Joey Lawrence recently joined our research group and was willing to spend many late nights assisting me in finishing time sensitive tests.

After all this is over, I expect that distance will, in fact, make the heart grow fonder between myself and my friends made in the midst of graduate school research; to take an excerpt from my friend Mr. Scott's thesis dedication, I wish them the best across the sea of years.

Funding for this work, in part, was provided by the Air Force Office of Scientific Research through Award No. FA9550-15-1-0102. Funding for this work was also provided, in part, from ONR contract 000062867 Predictive Chemistry & Physics at Extreme Temperature and Pressure: molecules, crystals and microstructure (PCP@Xtreme). I also wish to acknowledge support from the Science, Mathematics and Research for Transformation (SMART) Scholarship for Service Program under grant No. 2016-99534.

PREFACE

…don't forget the bigger picture[1].

Chapter 3 contains data acquired at a DoD facility which is DISTRIBUTION A. Approved for public release; distribution unlimited [96TW-2019-0443]. Chapter 4 also contains data acquired at a DoD facility which is DISTRIBUTION A. Approved for public release; distribution unlimited [96TW-2019-0444].

[1]See The Illustrated Guide to a Ph.D., by Matt Might (http://matt.might.net/articles/phd-school-in-pictures/)

TABLE OF CONTENTS

LIST OF TABLES

LIST OF FIGURES

LIST OF SYMBOLS

α a polymorphic phase of HMX with a limited range of stability; this symbol is also used to represent the scale parameter of the log-logistic distribution

β a metastable polymorphic phase of HMX; this symbol is also used as the shape parameter for the log-logistic distribution

δ a metastable polymorphic phase of HMX

μ the mean of the normal or logistic distribution

σ the standard deviation of the normal distribution

s the spread parameter of the logistic distribution; this symbol is also used to represent the slope of the U-u Hugoniot plane

$\hat{\mu}$ the estimated mean of the normal or logistic distribution

$\hat{\sigma}$ the estimated standard deviation of the normal distribution

$\hat{s}$ the estimated spread parameter of the logistic distribution

n the number of samples used to estimate the parameters of a distribution

H_0 the null hypothesis of some test

C_0 the bulk sound speed of a given material, calculated from the y-intercept of the U-u Hugoniot plane

ABBREVIATIONS

IUPAC	International Union of Pure and Applied Chemistry
PDF	Probability density function
CDF	Cumulative distribution function
PBX	Polymer bonded explosive
SSGT	Small-scale gap test
BAM	Bundesanstalt für Materialforschung und -prüfung (federal institute for materials research and testing)
MLE	Maximum likelihood estimation
AFRL	Air Force Research Labs
AP	Ammonimum perchlorate
PETN	Pentaerythritol tetranitrate
SSE	Sum of squared estimate of errors
SHG	Second harmonic generation
FIB	Focused ion beam
SEM	Scanning electron microscopy
μCT	Micro-computed tomography
Nd:YAG	Neodymium-doped yttrium aluminum garnet
Laser	Light amplification by stimulated emission of radiation
FEM	Fluid energy milled
DSC	Differential scanning calorimetry
XRD	X-ray powder diffraction
TGA	Thermogravimetric analysis

NOMENCLATURE

HMX	'High Melting Explosive'; also known as octogen; preferred IUPAC name: 1,3,5,7-Tetranitro-1,3,5,7-tetrazoctane
RDX	'Research Department Explosive'; also known as cyclonite, hexogen, T4; preferred IUPAC name: 1,3,5-Trinitro-1,3,5-triazinane
PBX 9501	95% HMX (by volume) in a bimodal distribution of ∼120 and 30 μm diameter particles plus 2.5% Estane plus 2.5% a 50/50 eutectic mixture of bis(2,2-dinitropropyl) acetal (BDNP-A) and bis(2,2-dinitropropyl) formal (BDNP-F)
L50	The stimulus level at which 50% of samples are expected to react, often reported as a drop-weight height
SS_{tot}	the total sum of squares, proportional to the variance of a dataset
R^2-value	the coefficient of determination

ABSTRACT

Information on the sensitivity of explosives is highly valuable, and the short time scales in which chemical reactions occur in explosives, along with the ability of microstructure to have significant effects on sensitivity, often make this information difficult and expensive to acquire and interpret. Significant changes in impact and shock sensitivity are expected as a result of inducing structural damage in an explosive sample, and thermally damaged HMX-based samples can incur a solid-solid phase transition from $\beta \rightarrow \delta$ with non-extreme thermal inputs. Changes in sensitivity due to this phase transition, as well as the simultaneously induced damage, and their relative influence on sensitivity, are of interest to determine experimentally.

Drop-weight impact tests are a commonly used measure of explosive impact sensitivity. Often, simply the L50 of a given material is reported and compared with that of other materials to give a sense of its impact sensitivity. The practice of reporting the impact sensitivity as a single number, the L50, is likely inadequate. It is important to additionally report a measure of the spread of the distribution of reaction probabilities in order to assess the hazard of reaction in situations that may induce a stimulus level well below the L50 of a material. Additionally, multiple distribution forms have been suggested previously for fitting of binary sensitivity data; these distributions typically deviate from each other most near the tails (low and high stimulus levels). The consequences of choosing one distribution form over another in the analysis of explosive drop-weight impact results is explored.

Changes in impact sensitivity due to phase change have received some previous exploration, though the phase change influence is generally conflated with the induced damage upon said phase transition; however, sensitivity changes in the shock regime due to $\beta \rightarrow \delta$-phase change have received little attention. Work is shown which includes methods to isolate variables of HMX phase transition and damage typically incurred upon said phase transition.

1. REVIEW OF IMPACT STUDIES OF δ-PHASE HMX

A summary of the available literature on impact tests which involve δ-phase HMX is provided for the purpose of exhibiting current knowledge regarding the impact sensitivity of HMX in its several polymorphic forms, and to show a path forward for work studying the change in impact sensitivity of thermally damaged HMX based energetic materials. Much work has been dedicated to understanding the sensitivity increase of δ-HMX in particular, yet evidence of the mechanisms behind the sensitization is lacking. Below gives brief backgrounds on a number of relevant subjects, and a review of previous work on comparisons of impact sensitivity of various phases of HMX, particularly those of β and δ. Future work to come from this review of the literature may consider: (1) pressing pellets and then deconsolidating them to compare with non-pressed powders and (2) direct synthesis to δ-HMX and then sieving out particles similar to available β-HMX particles. Specific questions of interest which this review hopes to answer include:

- what is the scope of work that has been done on δ/β-phase HMX in dropweight tests?
- do historical data account for differences in morphology between δ/β-phase HMX?

1.1 Background

1.1.1 Phases of HMX

α Has a limited range of stability and has not been observed during the heating of β-HMX [1]; forms at an evaporating solvent-container interface [2]; orthorhombic needles [3], [4]

β The stable phase at room temperature and pressure; monoclinic massive [3], [4]

γ H_2O-HMX complex [1] under some conditions [5], [6] which forms during steam distillation of HMX solutions in various solvents, and on precipitation of HMX from water-miscible solvents by dilution with water [2]; monoclinic massive, platy [3], [4]

δ Usually formed by heating any of the other phases, and has been observed to be more impact sensitive than β-phase HMX [7], [8]; hexagonal rods, needles [3], [4]

ϵ Only observed under very high pressure conditions [9]

ϕ Only observed under very high pressure conditions [9]

1.1.2 HMX phase transition

A phase transition from β to δ HMX can occur with heating; however, δ-HMX may also be synthesized directly [1]. The lowest temperature at which a phase change from β to δ HMX has been observed is 158 °C [1]. The rate of transition and the temperature at which it occurs have been observed by a number of authors to depend both on the heating rate and the particle size, with smaller particles having higher transition temperatures [10]–[12]. It was concluded by Karpowicz and Brill that δ-phase HMX is the more stable form at temperatures above 248 °C [10]. The extent of surface changes in an HMX crystal during transition from β to δ were studied by Weeks et al. but isolation of these changes to determine the role of each variable (the phase change or the change in geometry) regarding impact or shock sensitivity was not conducted [13]. In the presence of a binder containing a plasticizer, conversion of β-HMX to δ occurs at lower temperatures than if the HMX is in its pristine state [14].

1.1.3 The dropweight impact regime

Field et al. [15] provides a description of how stress varies with time in a typical PBX sample undergoing drop-weight impact. The overall response is illustrated by Fig. 1.1. The first peak in Fig. 1.1a corresponds to brittle failure of the sample into fragments, followed by a region of lower stress while the fragments are compacted, after which the thin layer of material is pinched between the anvils causing the second peak. In thinner samples (Fig. 1.1b), the compaction phase is shorter or absent altogether, where brittle failure is evident as a small inflection of the leading edge of the pulse. It has been observed that ignition occurs after the rapid flow phase, which follows brittle failure of the sample [15], [16]. Additionally, the hot spot radius for ignition is a function of the explosive, the temperature, and its duration [17], and Bowden and Gurton showed that hot spot radii are typically 0.1 to 10 μm for initiation by friction or impact [18], [19].

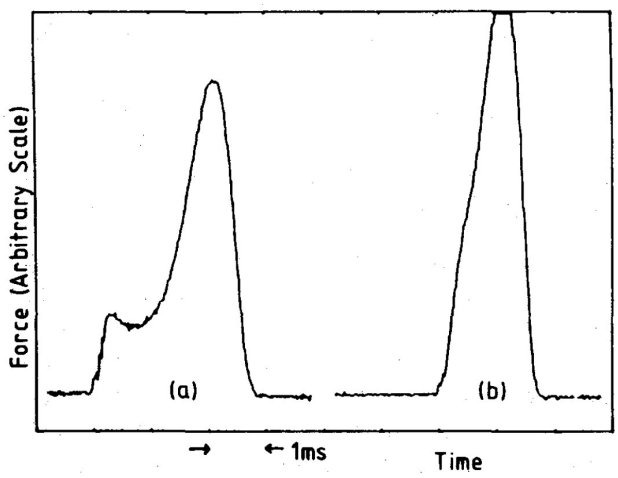

Figure 1.1. Force-time records for impact at 1 m/s on mock PBX samples for different aspect ratios: (a) sample diameter 6 mm, height 2.5 mm; (b) diameter 6 mm, height 1.5 mm. Reproduced from [15].

1.1.4 Energetic material geometries during impact tests

Czerski et al. found that δ-HMX was produced during impact tests on HMX pellets before and after ignition where a transparent anvil dropweight apparatus was used to measure the ignition delay time in HMX pellets, and δ-phase HMX produced during impact was probed using a Nd:YAG laser [1] at 1064 nm in order to detect Second Harmonic Generation (SHG), an indicator of the presence of δ-phase HMX [14], [20], [21]. The samples tested by Czerski et al. were UK β-phase HMX with an average particle size of 175 μm. Each HMX pellet was hydraulically pressed to 90%$\pm$1.5% of TMD (1.91 g/cm^3) with a diameter of 6 mm and a thickness of 1 mm. Metzner et al. [22] used cast PBX samples of a ring geometry rather than disk in order to allow inward and outward deformation, where evidence was seen that the beginning of the 'rapid flow phase' during impact is dominated by hoop stresses and strains near the outer edge of the sample. Herrmann et al. [7] did not make sample geometry clear for their performance of impact sensitivity testing, although it may reasonably be assumed that loose powders were used, as there is no mention of pressing or casting, and 'ground' and 'unground' samples are referred to. In that work, it is concluded that δ-HMX impact sensitivity reaches that of primary explosives, while acknowledging the work of Meyer et al. [23], which observed considerably higher required impact energies for violent reaction.

1.2 Select HMX phase impact sensitivity comparison studies

1.2.1 δ-phase HMX impact sensitivity is independent of crystal size and preparation method

It has been reported that δ-HMX samples containing crystals in the process of undergoing polymorphic transformation are more sensitive than samples of pure δ-HMX [2], [24]. Cady and Smith conclude that the sensitivity of δ-HMX is independent of the crystal size and the method by which the sample is prepared [2], agreeing with previous works [25], [26]; four preparation methods of δ-HMX were used in Cady's work: (1) heating β-HMX at temperatures between 159 and 165 °C, where the crystal size was controlled by the crystal size of the β-HMX, (2) recrystallization from a slurry of β-HMX, producing massive crystals of δ-HMX over 1 mm in diameter, (3) heating β-HMX at 190 °C to form fine crystals

of δ-HMX and (4) rapid recrystallization from acetic acid as described by Blomquist [25] to form fine δ-HMX crystals. However, Cady also concludes in the same work that the impact sensitivity of β-HMX is independent of particle size; this statement has since been contradicted by more recent observations [27]. It is somewhat difficult to determine exactly the geometry and sample preparation used by Cady (we are referred to [24] and others, of which reports I have not been able to find a copy), outside of the synthesis and phase conversion, but it is likely that a fixed amount of loose powder was used in impact tests, as no mention of pressing or casting is found in the report.

1.2.2 Increase in δ-phase HMX impact sensitivity is not due to physical difference from β phase

Asay et al. [8] concluded that the physical differences between samples containing β and δ-HMX are not the important factor in the increased sensitivity of the δ-phase to planar impact. Experiments used to draw this conclusion were gas gun impact experiments at 230–260 m/s on thin disks (5 mm x 1 mm) of PBX 9501 (density undisclosed) impacted between a sapphire surface (for optical access) and a polyethylene (PE) projectile. Three types of samples were tested: (1) pristine PBX 9501 pellets, (2) PBX 9501 samples heated to 172 °C at 5 °C/min and held for one hour, then rapidly cooled to lock in δ-phase, and (3) similarly heated PBX 9501 disks, and then were cooled at a prescribed cooling curve of 3 °C/min to 123 °C and held until reversion from δ to β was complete. Phases were verified using SHG and Raman spectroscopy. Representative image sequence for each of the three described cases are shown in [8]. Of note in these images is that the initiation of reaction begins first in a ring around the outside of the High Explosive (HE) disk and proceeds toward the center in cases (1) and (3); the reaction in the δ-phase sample, case (2), exhibits an ignition that appears simultaneously throughout. These observations show that β-HMX ignites in the region of highest shear (the edges of the specimen under compression [15], [22]), where the δ-HMX ignites spontaneously (consistent with shock-induced ignition); or else the δ-HMX ignites at lower levels of shear compared to β-HMX.

1.3 Some remaining research questions

Recent work at Purdue University has had the goal of obtaining a better understanding in the changes in sensitivity of PBXs which are subjected to damage. The primary focus of the type of damage input has been thermally induced for simplicity, and particular regimes of interest for sensitivity are impact and shock. As previous work has been examined, and experiments surrounding this topic have been performed, a number of questions in need of further research have arisen:

1. Is there a meaningful way to quantify and characterize the change in microstructure in a PBX which has been damaged?

2. For PBXs which include HMX, what role does the phase change from β to δ play in the material's sensitivity when it is heated; and similarly, what role does the change in porosity and cracks due to thermal expansion play?

3. Given that the phase change is significant (see point 2), is this change in sensitivity due to the crystal structure itself, or due to the physical damage, which changes the density and surface topology [13], that occurs in the HMX crystal upon undergoing this phase change, or some combination of the two?

4. Does the Probability Density Function (PDF) of drop-weight impact tests follow more closely a normal curve or a logistic curve, or some other form?

2. A REVIEW OF THE WORKS SURROUNDING δ to β-PHASE REVERSION IN HMX

Investigations involving phases of HMX have been ongoing for decades. More recently, a small number of studies have given attention to the effects of phase reversals on the properties of HMX and HMX-based PBXs. Below, a brief review of experimental methods and conclusions is presented for four key reports relating to $\delta \rightarrow \beta$-phase transitions in HMX.

2.1 Phase change observations in PBX 9501 pellets

The work of Smilowitz et al. [28] makes some key observations:

- In a 4 x 4 x 1 mm PBX 9501 pellet, radial gradients across the sample of less than 0.5 K can be maintained using heating rates of 4.8 K/min
- In the same pellet, cooling at $\sim$3 K/min allows $\delta \rightarrow \beta$ reversion to occur
- Assuming that the mechanism of harmonic generation is volumetric and fully coherent yields acceptable results, and as such Second Harmonic Generation (SHG) intensity normalized from zero to one (where one is a fully δ-phase PBX 9501 pellet) is interpreted as being proportional to the square of the δ mole fraction present in the sample
- Half time conversions ranged from 2 min. to 167 min., with environment temperatures ranging from 171 to 144 °C, respectively[1]

2.2 Phase changes in dry HMX powder and reversions in varying environmental conditions

Peterson et al. [29] use HMX-C dry powder and heat in a vacuum oven to make phase transitions from β to δ. Three different storage conditions are noted, and Raman spectra are measured periodically to monitor the phase state. Initial Raman spectra were measured

[1]Conversion half times at temperatures outside this range were observed, but the vast majority of β-δ transitions observed were in this range.

immediately after heating and indicated δ-phase for all three of the sample sets. Noteworthy points for each condition:

- Dessicator (no temperature/humidity monitoring reported)
  - All reported measurements indicated full δ phase (days 2, 3, 4, and 8)
- Ambient (22±2 °C; 30±10% relative humidity)
  - On day 2, 1/2 δ, 1/2 α-phase was indicated
  - All subsequent measurements (days 3, 4, and 8) indicated full α
- Humidified environment (22±2 °C; 96.5±1.5% relative humidity)
  - All subsequent measurements indicated full β-phase (days 2, 3, 4, and 8)

Scanning Electron Microscope (SEM) images were taken of four different groups of the HMX: (1) the starting material, β, (2) δ-HMX, (3) converted α-HMX, and (4) reverted β-HMX. Individual crystals, however, were *not* tracked, and the shapes of the δ-HMX seem to be inconsistent with literature, which indicate that δ-HMX particles are expected to be needle-like [3], [4]; however, as indicated by Cady [2], the size of the δ crystals may be controlled by the size of the β crystals if the temperature used to transition to δ is between 159 and 165 °C, but temperatures over 190 °C produce fine particles of δ-HMX. Peterson et al. reports heating samples at 184 °C for 14 hours.

Sensitivity testing was performed (friction and impact), of which no indication of sample sizes was given. L50 values were reported and compared, and Probability Density Functions (PDFs) for impact sensitivity were assumed to be rectangular (also known as a continuous uniform distribution). It was concluded that the starting material and the β reverted HMX exhibited similar L50s and σs, while α and δ HMX were about 20% more impact sensitive than β, and similar to each other.

It was observed that adding in fine HMX particles at 3:1 C/F (coarse = class 1, fine = class 2) significantly narrowed the distributions (σ decreased), and lowered the L50 in the case of the α (significantly) and δ (marginally), while β-HMX L50 remained largely the same.

It is worth noting the following in regards to the work by Peterson et. al.:

1. The sample sizes (i.e., number of samples tested) used were not indicated, and as such it is impossible to determine if the noted differences are statistically significant, or for that matter, the likelihood of Type II errors. As is discussed below, Yan et al. [30] concludes that reverted β-HMX develops a significant number of small voids (< 80 nm) within the crystal upon reversion. If the reversion to β-HMX plays an insignificant role in its impact-sensitivity, then this may provide a minimum pore size for effect lower bound.

2. Uniform PDFs were assumed, which are not realistic.

3. Individual crystals were not tracked through the process of phase transition and reversion. As such, features induced by each process can't be observed. Note that if the majority of the pores are of the sizes indicated by Yan et al. [30] (< 80 nm), then a CT scan will not be sufficient to resolve these important features. However, cracks may be resolvable.

However, the polymorph change during storage is a particularly helpful observation, although a more detailed analysis with higher time resolution, better volume fraction resolution, etc., would be of use. Additional detail to this end is reported by Yan et al. [30].

2.3 Phase change measurement techniques

Phase transition pathways are noted in [31] and shown in Fig. 2.1. There have been a number of apparent inconsistencies between δ-phase measurement/observation techniques, SHG, Raman spectroscopy, and Differential Scanning Calorimetry (DSC). Smilowitz [32] analyzed past data from a number of sources and compared the techniques. Comparison of these techniques with a nucleation and growth model are shown in [33].

It was concluded that the δ-phase observation techniques under question were all in agreement, assuming that the technique probed a representative volume element; e.g., for an integral SHG signal, this is done by using a beam spot size large enough to sample a volume

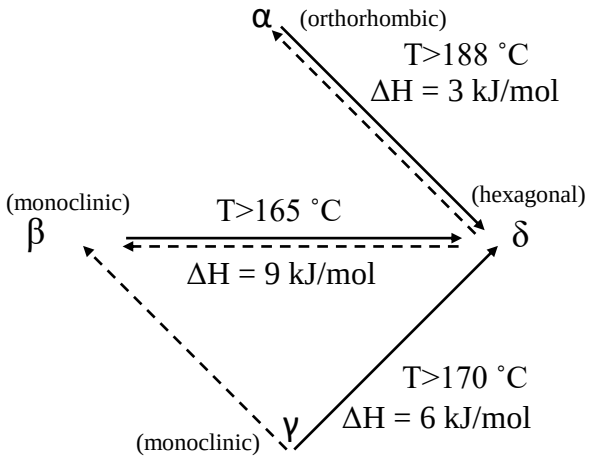

Figure 2.1. A summary of the temperature and pressure-induced phase transitions of the α, β, γ, and δ polymorphs of HMX. The solid lines are transitions with slow heating and the dashed lines are transitions with pressure. (R) indicates reversibility with cooling. Reproduced from [34] and [32], which reproduced the figure with low quality from the elusive [31].

large compared to the spatial heterogeneity of the sample [33]. Certain pros/cons of each technique were noted:

SHG provides the highest sensitivity (it is a zero background integral measure of the fraction of sample converted to the final phase), but it is not an absolute measurement due to light scattering properties and changes in light scattering and absorption. Additionally, it is only useful for symmetry changing solid phase transitions.

Raman spectroscopy is generally applicable and provides an integral progress variable; sensitivity is lost upon spatial integration, but the technique allows for distinguishing of non-centrosymmetric phases. It is also difficult to use as an absolute measurement due to the baseline flourescence and change in optical properties.

DSC is not an integral measure, so it's less sensitive and rate dependent, but it's best for use as an absolute measure (can be integrated to give the total fraction of the enthalpy of the phase transition). There is a minimum conversion rate needed for observation (dependent on baseline thermal stability).

Control of the reversion from δ to β-phase is also demonstrated in Fig. 2.2.

2.4 Phase reversion due to humidity

In a humid environment of about 60% relative humidity, and room temperature, $\sim$100% δ-HMX reverted to $\sim$65% β-HMX in 180 min., and reached 72% β-HMX within 18 hours [30]; however, it is indicated measurements were taken on only one sample which was subjected to this environment.

Volume fraction of voids is deduced with quasi-invariant integration [I *think* on Small-Angle Neutron Scattering (SANS) data], and the deduced volume fraction and pore size distributions for select storage times are shown in [30]. Note that the void size distributions were estimated assuming spherical voids.

It was noted that with the SANS measurements the added voids during storage could be (1) within the HMX crystals, (2) due to the interaction of binders with moisture, or (3) at the binder-crystal interface. It was concluded based on further SANS measurements of

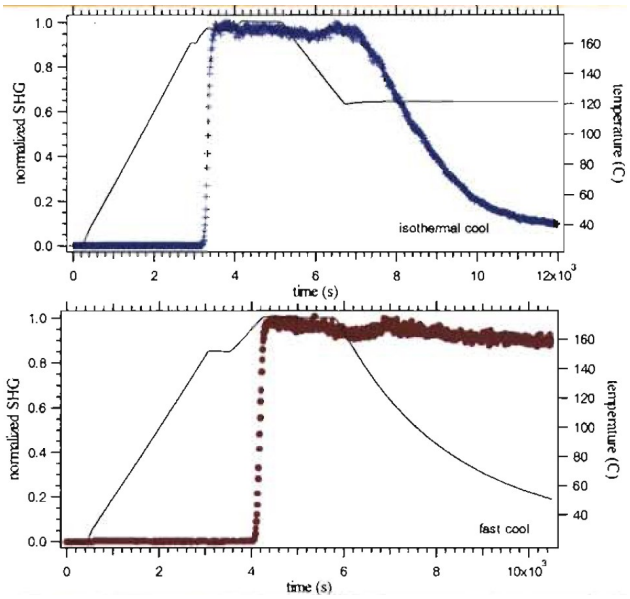

Figure 2.2. Inducing a transition to δ and subsequent reversion to β is shown (top), as well as a transition to δ and kinetic locking in of δ-phase (bottom). Reproduced from [32].

pure HMX particles that the increase in voids dude to storage in humid environment occurs primarily in the crystals of the HMX-based PBXs. The suggested process of void creation is illustrated in [30].

3. THE EFFECT OF THE CHOSEN DISTRIBUTION FORM ON REACTION PROBABILITY ESTIMATES FROM DROP-WEIGHT IMPACT RESULTS

3.1 Background

The sensitivity of explosives cannot be described by a single parameter, but is highly of interest to the explosives community in regards to both safety and intentional initiation [35], [36]. Sensitivity is treated probabilistically in each of its subcategories including sensitivity to friction, impact, heat, shock, and electrostatic discharge. Complex factors which can be difficult to control, such as variations in microstructural morphology, constituent properties and distribution, and loading, bring about the non-deterministic nature of sensitivity [37]. The sensitivity of an energetic material to mechanical insult in the form of weak impact, also known as impact sensitivity, is often measured using a drop-weight impact apparatus, and is the focus of this work. Impact sensitivity evaluation is used as a means for screening novel energetics and evaluating safety concerns during transportation or stimuli from dropping, rough handling, and/or poor protection of explosives in industry and research laboratories [38], [39]. Although this test has been performed for decades, the statistical treatment is generally quite limited.

The sensitivity of an explosive to some stimulus (e.g., drop-weight impact) is evaluated by a statistical test often referred to as a sensitivity test or a 'go/no-go' testing procedure. The origins of these sensitivity tests date back to the late 1940s [40], [41] and stem from research conducted to determine the drug dosage required to observe a response in the subject. These tests are generalized to any field by referring to 'dosage' as stimulus level and noting whether the expected response (a 'go') occurred or did not occur (a 'no-go').

After performing sensitivity tests, often an L50 stimulus level is reported alone; i.e., for drop-weight impact tests, often the height at which 50% of the samples are expected to react is reported [38]. Consequently, attempting to rank two materials against each other in terms of impact sensitivity, only the L50s of each are compared, which can introduce significant error and may be inadequate or misleading. Guymon [42] indicates one problem of comparing L50s alone with an example relating to drop-weight impact sensitivity: given

a particular population of RDX with a true L50 drop height of 45.9 cm, testing 30 samples from that population would yield an L50 between 40.9 and 50.9 cm with 95% confidence. Thus, a novel material undergoing sensitivity testing which yields an L50 of 41 cm cannot, with statistical significance, be ranked as more sensitive than RDX at every stimulus level. In order to provide a meaningful ranking of sensitivity, it is important to report the parameters that allow estimation of a Probability Density Function (PDF).

It is assumed that every sample produced has a specific drop-height (or stress/strain input) threshold, which, if exceeded, will cause a given sample to react. This is known as a latent threshold, because it cannot be measured directly by any means currently known. The latent thresholds are determined by a number of factors, including the sample microstructure, density, composition, constituent ratio, particle size distribution, etc., in addition to uncertainties in the input stimulus. Due to the variability in these determining factors, a population of samples will have a distribution of latent thresholds, again, which cannot be measured directly. In the case of the normal (also known as Gaussian or bell curve) distribution, the parameters μ and σ are used to estimate the characteristics of a population of samples in terms of latent thresholds to a drop-height stimulus. A straightforward method for making relative sensitivity comparisons or rankings in a statistically significant manner using just μ and σ is presented by Guymon [42].

An additional shortcoming to considering only the L50 of a substance is that it provides no insight on safety concerns regarding stimuli at levels lower than the L50, and likewise does not provide information for evaluating reliability when the substance is insulted at stimulus levels higher than the L50. Estimating the latent threshold distribution provides a method to predict material sensitivity at any prescribed stimulus level. The accuracy of the estimation generally increases with the number of tested specimens used in its calculation.

In order to estimate and fit a distribution, an assumption about the form of the distribution must first be made. Some distribution forms are better suited for certain applications; e.g., bacteria growth naturally follows an exponential distribution [43], and the log normal distribution is particularly well suited to describe many particle size measurement samples [44]–[46]. The most common form used, however, is the normal distribution. Upon reviewing previously performed Small-Scale Gap Test (SSGT) work [47]–[53], the distribution form

followed by sensitivity tests came into question. It has been suggested that it is sometimes more suitable to estimate the go/no-go probability of SSGTs using a logistic distribution rather than a normal distribution [48], [54]. The primary reasons given for making this change were that the logistic distribution, in comparison with the normal distribution, (1) is more conservative at the tails, (2) may more accurately represent SSGT datasets, and (3) is more computationally efficient to use. A logistic distribution has a similar shape to a normal distribution, but exhibits higher kurtosis (heavier tails). In contrast, Guymon [42] reported that Safety Management Services, Inc. (SMS) and Alliant Techsystems Inc. (ATK, formerly Hercules Inc.) assume a log-logistic distribution for standard test levels, which doesn't allow negative stimulus levels and is asymmetric.

Here, it is suggested that additional attention be given to the risks associated with exciting materials below or above their estimated L50 stimulus levels. Doing so will allow researchers to more adequately assess risks of transport, experimentation, and the practical use of energetic materials.

In this work, two different distribution forms are assumed (normal and logistic) prior to performing impact sensitivity tests. Statistical analysis is performed on the results of the drop-weight impact experiments to gather evidence on the importance of the assumed distribution form. The objective of this study is to explore the practical differences incurred on estimation of reaction probability when choosing between the distribution forms mentioned above for test design and analysis of drop-weight impact tests.

3.2 Sample Preparation

PBX 9501 (Batch: 9501B-32; Lot: BAE12M145-028) was pressed into cylindrical samples, 3.2 mm diameter by 1.0 mm height, yielding 94±2.3% Theoretical Maximum Density (TMD), all with mass of approximately 14.3 mg. Care was taken to mark the pellets in order to distinguish the dynamic face (the face of the pellet closest to the pressing die's ram) and the static face (the face of the pellet closest to the bottom of the die, opposite of the ram) to control for density variations due to wall friction.

3.3 Experimental methods

The pressed PBX 9501 samples were manufactured for use as an example dataset of drop-weight impact results. The samples were tested in a drop-weight impact apparatus under BAM [55] configuration, where the sample was oriented consistently such that the dynamic face of the pellet would receive first contact with the drop-weight. Because a relatively small amount of information is obtained after testing an individual sample in a drop weight test due to difficulties in estimating a latent threshold distribution based on a binary outcome (go/no-go), it is necessary to choose an optimized method for obtaining parameter estimates about the population of samples undergoing testing. The Neyer SenTest^{TM} was chosen here as a means to provide a sequential test design which minimizes the number of samples necessary to accurately estimate the true distribution parameters of the representative samples being tested. The Neyer SenTest^{TM} estimates the distribution parameters via Maximum Likelihood Estimation (MLE). A major benefit of the Neyer algorithm, contained within the Neyer SenTest^{TM}, is that it provides a sequential design. Sequential design is defined as the ability of the algorithm to suggest a stimulus level at which to test. Sequential designs attempt to propose stimulus levels such that the observed outcome will provide valuable information to better estimate the parameters. Neyer's sequential design proposes the stimulus level which maximizes the determinate of the Fisher information matrix [56], [57].

Within the Neyer SensTest^{TM} software, either normal or logistic distribution functions may be assumed, which accordingly provide different sequential test designs. In an effort to avoid providing favorable circumstances to one distribution form over the other, samples were randomized and assigned to one of two groups, with $\sim$25 samples in each dataset:

1. PBX 9501 samples tested assuming a normal distribution, and accordingly using a normal sequential design given by the Neyer method [57] — (Group A),

2. PBX 9501 samples tested assuming a logistic distribution, and accordingly using a logistic sequential design given by the Neyer method — (Group B),

Prior to acquiring data for the above outlined datasets, a smaller initialization dataset was used to approximate μ and σ for a normal distribution, which were used as initial guesses

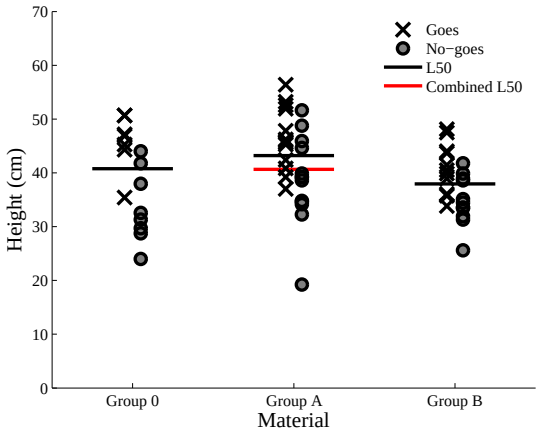

Figure 3.1. Impact test results, including initialization results, labelled as 'Group 0'. The 'Group A' followed the sequential design of the Neyer method where a linear normal response was assumed. 'Group B' followed the sequential design of the Neyer method where a linear logit response was assumed. The 'Combined L50' line represents μ, the height at which 50% of the population of samples is expected to react, after combining the three related sample sets, namely 'A', 'B', and '0'.

for the datasets (1) and (2) above. This initialization data is shown alongside datasets (1) and (2) in Fig. 3.1, and is labelled 'Group 0'.

3.4 Analysis

From the results shown in Fig. 3.1, a PDF and Cumulative Distribution Function (CDF) for each dataset can be constructed using Maximum Likelihood Estimation (MLE) [40], [58]. The CDF is given by integrating the PDF from negative infinity through all stimulus levels, and is particularly convenient for the observer in relation to drop-weight impact test results, because it provides a direct estimate of the percent chance (vertical axis) that a sample will react to any given stimulus level (horizontal axis). The percent chance henceforth is referred to as the reaction probability.

The mathematical form of the normal PDF is

$$P_{\text{norm}} = \frac{1}{\sigma\sqrt{2\pi}} \exp\left[\frac{-(x-\mu)^2}{2\sigma^2}\right], \tag{3.1}$$

Table 3.1. Parameters for the estimated PDFs based on results given in Fig. 3.1, where n is the number of samples tested for each dataset, $\hat{\mu}$ is the estimated location parameter, $\hat{\sigma}$ is the estimated scale parameter using a normal assumption, and $\hat{s}$ is the estimated scale parameter using a logistic assumption.

PDF	$\hat{\mu}$ **(cm)**	$\hat{\sigma}$ **(cm)**	$\hat{s}$ **(cm)**	n (-)
Group 0	42.21	6.44	(–)	15
Group A	44.60	8.79	(–)	27
Group B	39.34	(–)	2.98	24

where μ and σ are the characteristic parameters estimated from the dataset using MLE. The logistic PDF is of the form

$$P_{\text{logistic}} = \frac{1}{4s}\left[\text{sech}\left(\frac{x-\mu}{2s}\right)\right]^2, \tag{3.2}$$

where μ and s are parameters for the logistic distribution estimated from the dataset, again using MLE. The stimulus level, or drop height in the case of drop-weight impact tests, is represented by x in Eq. 3.1 and 3.2. Note that in Table 3.1, only the parameters corresponding to the assumed distribution during testing are given in order to avoid confusion; however, optimal parameters could be estimated for any given two-parameter distribution function using MLE.

The normal distribution form is often used to fit drop-weight impact results (although typically only the L50 is considered and/or reported), while the logistic distribution form has been suggested as potentially a more accurate fit [48], [54] for drop-weight impact results. An additional distribution form, the log-logistic distribution, was reported to be in use by companies involved in sensitivity testing [42]; thus, three curves are given for the dataset using MLE for three different distribution forms to assess goodness of fit. The log-logistic PDF is unique from the normal and logistic PDFs, in that it is not inherently symmetric, and is constrained to yield a reaction probability of zero at the stimulus level of zero. This is a realistic constraint in the case of drop-weight impact tests, and thus it may be desirable,

but whether the response of energetics to impact testing tends to be symmetric is not well known, and is outside the scope of this study. The log-logistic PDF is of the form

$$P_{\text{log-logistic}} = \frac{(\beta/\alpha)(x/\alpha)^{\beta-1}}{[1+(x/\alpha)^{\beta}]^2}, \tag{3.3}$$

where α is the scale parameter and β is a shape parameter.

3.5 Results and discussion

After noting the estimated parameters for each individual group (Table 3.1), the drop-weight impact results for 'Group A' and 'Group B' were aggregated. The PDFs and CDFs for these aggregated results are shown in Fig. 3.2 and 3.3, respectively. Further discussion of the curves shown in Fig. 3.2 and 3.3 will refer to them as reaction 'probability PDF' and 'reaction probability CDF', respectively. The values for the parameters of these PDFs are given in Tables 3.2 and 3.3.

It was found that the Neyer SenTest$^{\text{TM}}$ software did not achieve the optimum fit when estimating parameters for the logistic distribution, although the software's normal distribution fit agreed exactly with the calculations made in this work.

'Group 0' was not included in the aggregate data (Fig. 3.2 and 3.3) in order to represent the normal and logistic sequential design evenly, since the initialization group was tested using a normal assumption; it was verified, however, that including the initialization data causes very little difference in the overall scale and location of the distribution shown in Fig. 3.2 and 3.3, due to the fact that the initialization dataset was smaller and consistent relative to the datasets used for distribution estimation.

3.5.1 Assessment of the difference between the distribution forms

Fig. 3.2 and 3.3 show three different functional forms of reaction probability PDFs fit to the same dataset, which appear to predict very similar reaction probabilities at any given stimulus level. This is consistent with work showing that the normal and logistic forms are structurally and predictively equivalent for univariate systems [59], such as drop-weight impact sensitivity.

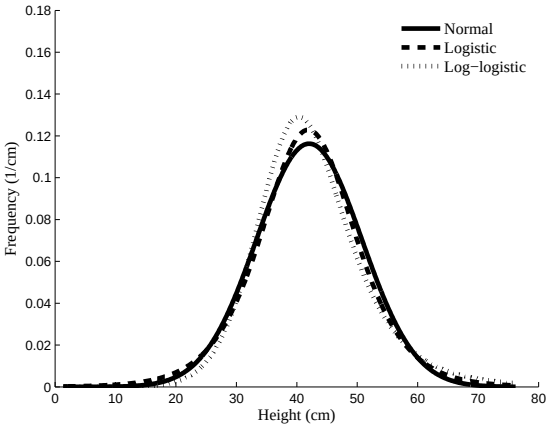

Figure 3.2. Estimated PDFs of combined 'Group A' and 'Group B' data. Maximum Likelihood Estimation was performed using three different distribution forms on the same set of results.

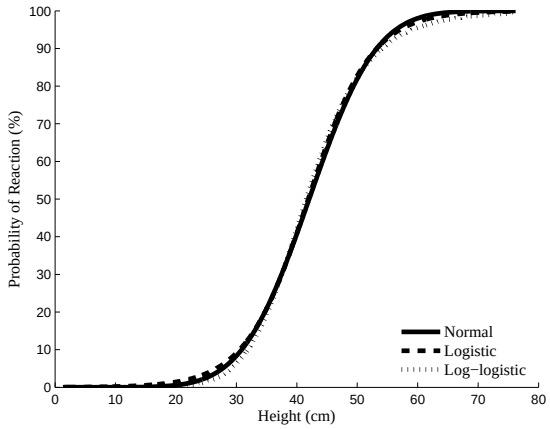

Figure 3.3. Estimated CDFs of combined 'Group A' and 'Group B' data. Maximum Likelihood Estimation was performed using three different distribution forms on the same set of results.

Table 3.2. Parameters for the PDF/CDFs given in Fig. 3.2 and 3.3. The spread parameters, σ and s are separated and given for normal and logistic forms, respectively, in order to reiterate that two different forms of PDFs are shown.

PDF	$\hat{\mu}$ **(cm)**	$\hat{\sigma}$ **(cm)**	$\hat{s}$ **(cm)**	n (-)
Normal	42.05	8.72	(–)	51
Logistic	41.89	(–)	5.17	51

Table 3.3. Parameters for the log-logistic PDF/CDFs given in Fig. 3.2 and 3.3. Here, α is the scale parameter and β is a shape parameter.

PDF	$\hat{\alpha}$ **(cm)**	$\hat{\beta}$ **(cm)**	n (-)
Log-logistic	41.55	21.15	51

Although the reaction probability estimates for each form are quite similar amongst themselves, they are not exactly the same, and the largest difference in probability of reaction tends to be near the tails, as is most clearly shown by the reaction probability CDFs (Fig. 3.3.

One might desire to design an experiment to test which distribution is most accurate at a particular stimulus level, in which case the most convenient and efficient method would be to choose the stimulus level which exhibits the largest difference in reaction probability, and test a number of samples at that stimulus level until reaching sufficient confidence and precision in the measured reaction probability to distinguish one distribution form reaction probability estimate from another.

In the case of this dataset of PBX 9501 tested samples, it is shown by the CDF (Fig. 3.3), that the largest difference between the normal and logistic distributions occurs at a drop-height of 24.4 cm, where the normal estimates a 2.8% reaction probability, and the logistic estimates a 4.0% reaction probability. Assuming that the distribution estimates are well-founded on a sufficient number of samples, the number of samples needed to achieve the precision necessary to determine which distribution form more accurately represents the data can be ascertained with the use of a Monte Carlo type simulation, or an analytical approximation using two normal distributions may be used. The distributions obtained using the Monte Carlo type simulation are representative of the possible outcomes of an experiment using a chosen number of samples, and are separate from the reaction probability distributions; henceforth these distributions are referred to as the binomial distributions, although they are approximated by normal distributions. The relationship between the Monte Carlo simulated binomial distributions and the reaction probability distributions (Fig. 3.3) is simply that the probability of reaction is obtained at a chosen stimulus level from a CDF such as that shown in Fig. 3.2, and that probability of reaction is used in the Monte Carlo simulations to obtain two binomial distributions, which are centered on the reaction probabilities obtained at the chosen stimulus level.

3.5.2 Use of a Monte Carlo type simulation

Assuming that a given stimulus level yields either a 2.8% or 4.0% reaction probability, a certain number of samples may be input into a simple Monte Carlo simulation, which are

tested using a pseudo-random number generator, where the percent of reacted samples is calculated and recorded, at which point the simulation repeats itself. A schematic showing the flow of such a simulation is shown if Fig. 3.4.

Repeating this simulation for both reaction probabilities (2.8% and 4.0% in this case) yields two histograms which may be approximated by normal distributions. With a low number of samples, the two histograms are indistinguishable, and often non-normal (see Fig. 3.5). Additionally, at very low reaction probabilities, even higher numbers of samples are required in order for the histograms to be approximated accurately by a normal distribution (see Fig. 3.6). The area of overlap can be calculated relative to the area of the two normalized histograms, and may be interpreted as the probability of a Type I error. In this case, a Type I error refers to concluding erroneously that one of the distribution forms is the better fit at this stimulus level when in fact the other distribution form is actually the better fit.

For example, in the case of testing 2,500 samples (Fig. 3.6), if the samples truly have a 2.8% reaction probability at a 24.4 cm drop-height (as given by the normal reaction probability distribution in Fig. 3.3), there is a 4.7% chance that the experimenter would determine, erroneously, that the samples have greater than a 2.8% reaction probability, and thus would choose the logistic reaction probability distribution which predicts a 4.0% probability of reaction at a drop-height of 24.4 cm. Likewise, if the samples truly have a 4.0% reaction probability, there is a 5.8% chance that the experimenter would determine, again erroneously, that the samples have less than a 4.0% reaction probability, and thus would choose the logistic reaction probability distribution which predicts a 2.8% chance of reaction. The total Type I error is the total area of the overlap region, 10.5%, divided by the total area of the two histograms, 200%, yielding $\alpha = 5.2\%$, where α is the probability of a Type I error. This is, of course, assuming that the experimenter is highly confident that the population of samples follows one of the two distributions very closely.

3.5.3 Using an analytical approximation

An analytical solution for finding the overlap between the two Monte Carlo simulated distributions is presented below using two normal distributions. The form of the normal

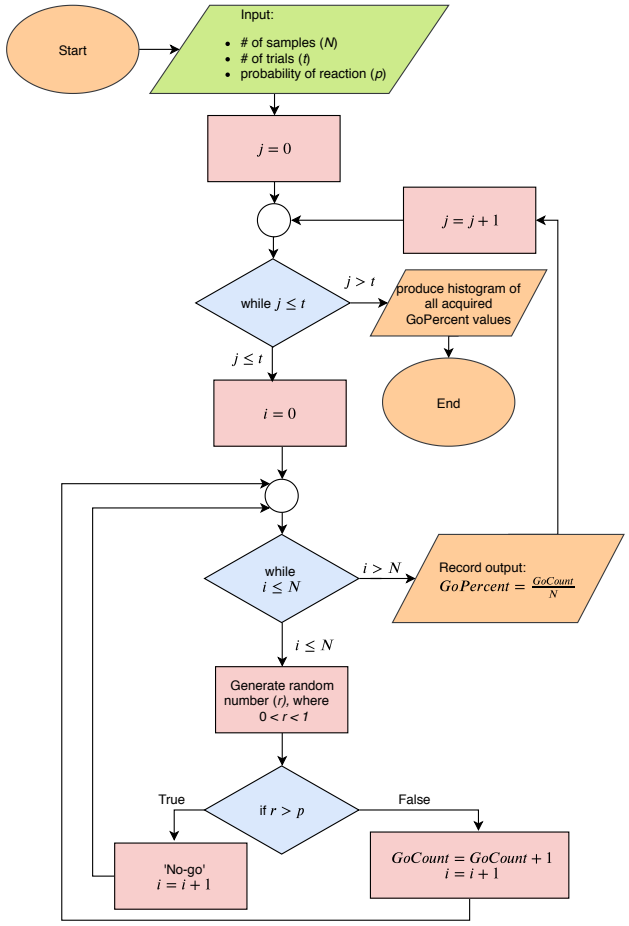

Figure 3.4. Flow chart of a simple Monte Carlo type simulation intended to assist in determining the number of samples necessary to distinguish between two different reaction probabilities experimentally.

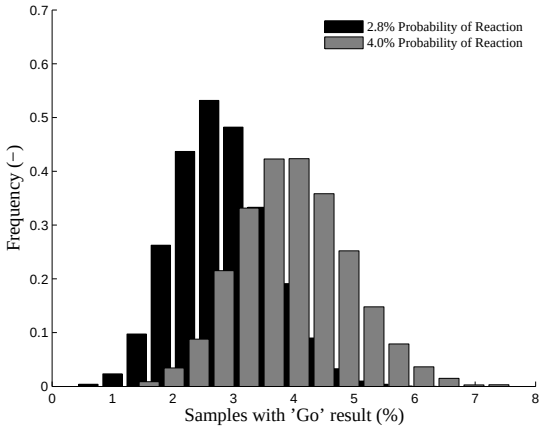

Figure 3.5. Results of the Monte Carlo type simulation where an experiment using 500 samples was simulated 10,000 times. Note the significant region of overlap, indicating that this number of samples insufficient for distinguishing between the two distribution forms.

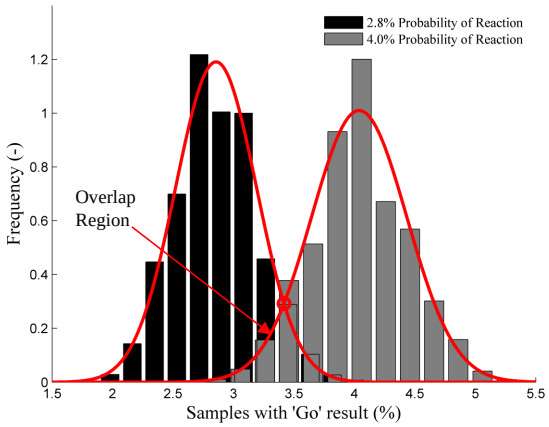

Figure 3.6. Results of the Monte Carlo type simulation where an experiment using 2500 samples was simulated 10,000 times. For demonstration, a normal distribution curve is fit to each of the histograms using a red line, and the overlap region is indicated. The overlap region decreases in area as the number of samples is increased, in turn increasing the confidence that the experiment will yield results which may distinguish between the two distribution reaction probabilities.

distribution is given in Eq. 3.1. The intersection point between two normal distributions with differing parameters can be found by equating them accordingly:

$$P_1(\mu_1, \sigma_1) = P_2(\mu_2, \sigma_2) \tag{3.4}$$

where P_1 is designated here as the distribution with the lower reaction probability, and P_2 as that with the higher reaction probability, i.e., $\mu_2 > \mu_1$. The intersection point is used to determine the portion of each distribution area to be designated as part of the overlap region. Manipulating Eq. 3.4 into a form for which x may be solved yields

$$\begin{gathered}\left(\sigma_2^2 - \sigma_1^2\right) x^2 + 2\left(\mu_2\sigma_1^2 - \mu_1\sigma^2\right) x + \\ \left[\mu_1^2\sigma_2^2 - \mu_2^2\sigma_1^2 - 2\sigma_1^2\sigma_2^2 \log\left(\frac{\sigma_2}{\sigma_1}\right)\right] = 0.\end{gathered} \tag{3.5}$$

The quadratic equation can be used to solve for the intersecting x in Eq. 3.5, which yields two solutions, of which the positive term is taken in this case.

Now, if enough samples are taken for each trial, a normal distribution of 'percentage of samples with go result' is yielded, which is referred to here as the binomial distribution. As is exhibited by the Monte Carlo simulation results (Fig 3.5 and 3.6), the binomial distributions are centered around $\mu = p$, where p is the probability of reaction for each case, and with $\sigma = \sqrt{p(1-p)/n}$, where n is the number of samples used in the simulation. Then, a normal CDF is used to acquire the analytical solution to α, the probability of a Type I error, and is

$$\alpha = \frac{1}{2} + \frac{1}{4}\left[\operatorname{erf}\left(\frac{x - \mu_2}{\sigma_2\sqrt{2}}\right) - \operatorname{erf}\left(\frac{x - \mu_1}{\sigma_1\sqrt{2}}\right)\right]. \tag{3.6}$$

Further, the confidence that the result will not lead to a Type I error can be expressed as conf. $= 1 - \alpha$. Note that under Eq. 3.6, the Type I error probability is a minimum of 50%, which is intuitive, considering that two options are tested using this method, and with zero information, there is a 50% chance of choosing the more accurate representation.

Fig. 3.7 shows the increasing confidence as the number of samples is increased using both the analytical solution and the Monte Carlo simulation.

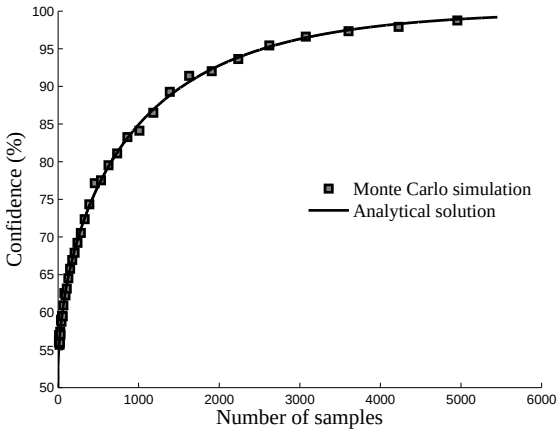

Figure 3.7. Confidence in the experimental result as number of samples is increased.

The above analysis shows that the normal, logistic, and log-logistic distribution forms are so similar in this case that an inordinate number of samples would need be required for testing at one stimulus level in order to measure the difference between the two distributions. In the case of the PBX 9501 samples used in this study, it would be necessary to perform drop-weight testing at 24.4 cm with ∼2540 samples to determine which distribution more closely estimated the population at that stimulus level with 95% confidence. For demonstration that this is not unique to this dataset, and rather that a univariate system such as the drop-weight impact test generally yields results which can be estimated nearly equivalently by any one of the three distribution forms considered in may cases, the above analysis on data acquired by the Air Force Research Laboratory (AFRL) is presented below.

3.5.4 Analysis of additional drop-weight impact results

The analysis presented above was applied to drop-weight impact results tendered by AFRL on a number of materials in both pure powder and binderized form. Some of the results shown are from 'standards', which are regularly tested on the AFRL drop-weight impact apparatus in order to verify the consistency and reliability of results. The records on 'standards' are numerous, although since multiple experimenters are involved, and conditions which may affect the results, such as relative humidity, vary widely from day to day, the variance in such results tends to be large. Other materials only show the results from one set of tests (typically 25 samples). It should be noted that the AFRL experiments used a Bruceton 'up and down' method, as described in [60]. This method is generally less efficient at providing an accurate estimate of σ relative to the Neyer Method. The results from these differing conditions were analyzed in order to demonstrate the ability and limitations of the three distribution forms to fit differing datasets.

Estimated distributions for powdered materials are shown in Fig. 3.8, and those for PBXs, named 'PBX A' through 'PBX D' for proprietary purposes, are shown in Fig. 3.9.

Material types and the number of samples analyzed to estimate the distributions are given by Table 3.4. For concision, only the normal Maximum Likelihood Estimates (μ and σ) are shown for each material in Table 3.4.

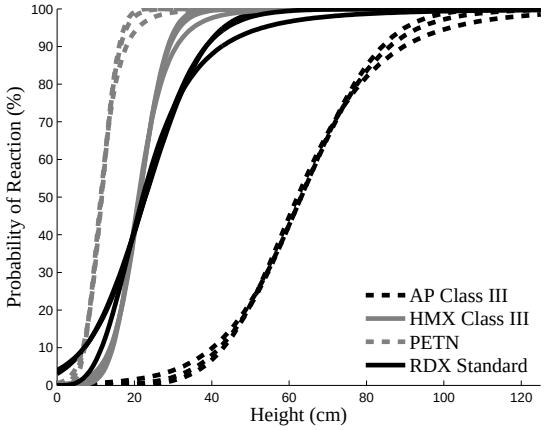

Figure 3.8. Estimated CDFs for data analyzed from powdered materials which received drop-weight testing at AFRL. Note that three CDF forms are shown for each material: the normal, logistic, and log-logistic form.

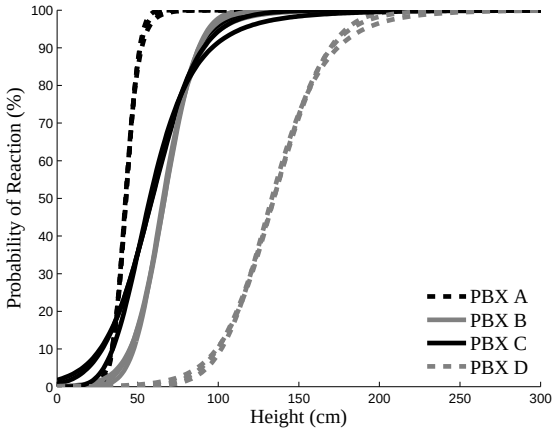

Figure 3.9. Estimated CDFs for data analyzed from binderized materials which received drop-weight testing at AFRL. Note that three CDF forms are shown for each material: the normal, logistic, and log-logistic form.

Table 3.4. A wide range of material compositions were analyzed from AFRL data, some of which had several years worth of data compiled, which was aggregated for analysis in this work. Other materials only received one day's worth of testing (25 samples). The estimated Maximum Likelihood Estimates for the normal distribution and the number of samples used in the analysis (n) are shown here.

Material	$\hat{\mu}$ **(cm)**	$\hat{\sigma}$ **(cm)**	n
AP Class III	63.1	16.3	25
HMX Class III	21.3	5.7	25
PETN	11.5	3.6	25
RDX Stand.	22.8	12.2	1497
PBX A	42.7	6.7	100
PBX B	66.7	16.6	349
PBX C	59.1	24.2	200
PBX D	134.5	27.3	25

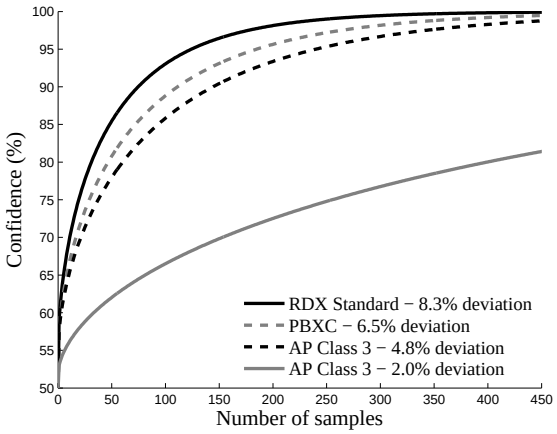

Figure 3.10. Number of samples required for drop-weight impact testing to distinguish from the log-logistic distribution reaction probability at a stimulus with maximum deviation. The log-logistic form for 'RDX Standard' and 'PBX C' exhibited the largest reaction probability deviations from the normal and logistic forms among the results analyzed. The log-logistic form for 'AP Class 3 - 4.8% deviation' exhibited a typical maximum reaction probability deviation from the normal and logistic forms. The logistic form for 'AP Class 3 - 2.0% deviation' exhibited the largest reaction probability deviation from the normal form among the results analyzed.

In all of the cases, the difference in reaction probability between the normal and logistic form was no more than 2.0% at any given stimulus level, which would require over 1,530 samples of drop-weight impact testing to distinguish the two forms with 95% confidence (see Fig. 3.10).

The log-logistic distribution form, however, tends to deviate further from the other two forms, especially in cases where the estimated normal μ is very low (impact sensitive materials), or the estimated normal σ is large (materials which exhibit highly varied responses to impact, or that have had low numbers of samples tested) such that the estimated probability of reaction at a stimulus of zero is not near zero. This is the case for RDX Standard and PBX C (see Fig. 3.8 and 3.9), and indeed, for these materials the log-logistic distribution differs from the normal and logistic distribution by up to 8.3% and 6.5%, respectively; these deviations are the largest among the estimates made, and the number of samples required to achieve varying confidence levels is shown in Fig. 3.10.

The deviation of the log-logistic form is caused by its constraint to have a zero percent reaction probability at a stimulus of zero, while the normal and logistic forms do not have this constraint. This bound on the log-logistic distribution is realistic for the drop-weight impact test. In cases where the normal and logistic distributions predict a near-zero reaction probability, the maximum deviation of the log-logistic distribution from the other two tends to be below 5%, similar to that of AP Class III (shown in Fig. 3.10).

3.5.5 Simulations to assess the sampling efficiency of two sequential designs

The above analysis shows that the three distribution forms, normal, logistic, and log-logistic, collapse onto each other so closely that the worst fit among the data analyzed (which is between the normal distribution and the log-logistic distribution in the RDX Standard) would require over 120 samples to be tested at one stimulus level to distinguish between the two distributions. The worst fit between the normal and logistic distribution would require over 1,500 samples to be impact tested to measure the difference. This indicates that for most scenarios, Maximum Likelihood Estimation on drop-weight impact test data using any one of these three distributions is sufficient.

Additionally of interest is the efficiency of the sequential design in choosing stimulus levels which yield results where the Maximum Likelihood Estimates reach a reasonable estimate of the true distribution; i.e. the number of samples required to have confidence in the estimated distribution.

The efficiency of the sequential design using a normal or logistic distribution form assumption was assessed using a simulation within a sequential design method which was developed based on the Neyer SenTest^{TM}, where sample thresholds were randomly drawn according to an assigned population distribution.

Prescribing a true population distribution allowed a 'goodness of fit' measure to be calculated for each estimated distribution after a number of simulated samples had been simulated using the sequential design with either a normal assumption or a logistic assumption. The chosen 'goodness of fit' measure in this case was the coefficient of determination, also known as the R^2-value. The method used for calculating the R^2-value for each estimated distribution is given below.

The Sum of Squared Estimate of Errors (SSE) is calculated by

$$SSE = \sum_{\mathrm{i}}^{d} \left(y_{\mathrm{i}} - t_{\mathrm{i}}\right)^2, \tag{3.7}$$

where y_{i} is the estimated reaction probability at a given stimulus level, and t_{i} is the reaction probability from the prescribed distribution; i.e., t_{i} represents the true reaction probability. The total sum of squares (SS_{tot}) is also calculated with

$$SS_{tot} = \sum_{\mathrm{i}}^{d} \left(y_{\mathrm{i}} - \bar{y}\right)^2, \tag{3.8}$$

where

$$\bar{y} = \frac{1}{d} \sum_{\mathrm{i}}^{d} y_{\mathrm{i}},$$

where d is the number of discrete stimulus levels used to represent the continuous CDF. Finally, the coefficient of determination is calculated as

$$R^2 = 1 - \frac{SSE}{SS_{tot}}. \tag{3.9}$$

Each chosen number of samples was simulated 200 times, and the R^2-value that 95% of the trials exceeded was labeled the minimum R^2-value (with 95% confidence). A plot showing these values where the true distribution was either normal or logistic, and estimated using either a normal or logistic distribution assumption, is shown in Fig. 3.11.

The true distributions used for the simulation results shown in Fig. 3.11 were $\mu = 52.1$ cm for both the normal and logistic case, and $\sigma = 5.3$ cm for the normal case, and a roughly equivalent $s = 5.3/1.6 \approx 3.3$ for the logistic case. Fig. 3.11 qualitatively shows that a normal distribution function can fit an underlying true logistic distribution function equally as well as a logistic distribution function can fit an underlying true normal distribution function. Additionally, using the Neyer Method for sequential design, either assumption, normal or logistic, tends to fit the underlying true distribution as efficiently (in terms of number of samples tested) as the other assumption, regardless whether the form of the underlying true distribution is normal or logistic.

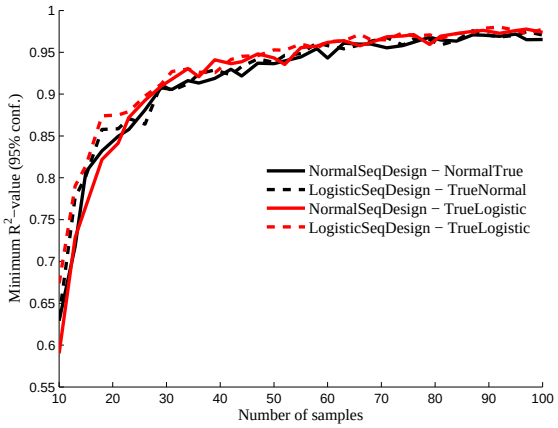

Figure 3.11. Measure of the minimum 'goodness of fit' (with 95% confidence) of the estimated probability of reaction distribution relative to the true probability of reaction distribution as the number of samples tested is increased. In this example, estimated normal distributions are fit to both true normal and logistic distributions ('NormalSeqDesign - NormalTrue' and 'NormalSeqDesign - TrueLogistic', respectively), and estimated logistic distributions are fit to both true normal and logistic distributions ('LogisticSeqDesign - TrueNormal' and 'LogisticSeqDesign - TrueLogistic', respectively).

Twelve additional prescribed true population distributions were simulated in this fashion, with 25 cm $< \mu <$ 77 cm, 2.5 cm $< \sigma <$ 13 cm, and 1.5 cm $< s <$ 8 cm. For clarity, only one prescribed distribution simulation is shown in Fig. 3.11, but the results are similar in that the normal sequential design highly overlaps with the logistic sequential design in every case, although, different prescribed distributions incur different rates of convergence to $R^2 = 1$.

3.6 Limitations

The drop-weight impact test is historically vexed in both indicators of go/no-go and quantified sensitivity values. It is well known that comparison of 50% probability of reaction heights for a given material between different drop-weight apparatuses tends to fail in consistency; as such, rankings are formed on a given machine at a given laboratory. This is likely a result of a lack of diligent statistical analysis and reporting and consistency in variables encountered from apparatus to apparatus. Both L50 heights and σ values for a given material should be reported in order for an audience to understand the spread and variability for the material and the machine used for testing. Additionally, an absolute minimum of 25 samples should be tested, though this number of samples for one material often yields unwieldy confidence regions on both μ (L50) and σ. Reasonable 95% confidence regions can be achieved with $\sim$50 samples. Higher quality reporting and higher volume of samples tested on the standard impact sensitivity drop-weight tester could increase the value of the results of this test significantly, despite the test's other inherent flaws.

3.7 Conclusions

A total of 66 pristine PBX 9501 samples were drop-weight impact tested in the BAM configuration using two different sequential test designs suggested by the Neyer method. Although a number of different distribution forms have been suggested in the past to represent sensitivity data, it was found that between the normal, logistic, and log-logistic distribution forms, the chosen functional form of the distribution to fit the data made no practical difference in the reaction probabilities at any stimulus level for the drop-weight impact test in

the cases analyzed. Additional drop-weight impact data tendered by AFRL was analyzed to confirm that this result wasn't unique to the one case of PBX 9501.

The Maximum Likelihood Estimates for some explosives yield reaction probabilities which are not near zero at the stimulus level of zero in the normal or logistic distribution form. This tends to be the case when a material exhibits highly varied responses to impact, or when a material is very sensitive. This additionally may be the case if too few samples were tested, or a non-efficient sequential design was used. In these cases, the log-logistic form deviates most significantly from the normal and logistic distribution forms. Even in these cases, the maximum deviation required over 120 samples to measure a difference between the distribution forms with 95% confidence. Obviously, the log-logistic distribution provides a more realistic reaction probability prediction (0%) at the zero stimulus level in these cases, but further testing of these cases is required to determine if the reaction probability predicted by the log-logistic distribution at non-zero stimulus levels is more realistic than that of the normal and logistic distributions.

The efficiency of sequential design type between the normal and logistic forms was explored by applying a measure of 'goodness of fit' to an estimated distribution relative to a prescribed population distribution and running a sequential design simulation for varying numbers of samples. It was observed qualitatively that the normal and logistic assumption are roughly equivalent in terms of sampling efficiency.

Each of the distribution forms analyzed, the normal, logistic, and log-logistic, are in use to predict reaction probabilities. It is apparent from this study that there is no real benefit to the use of the normal over the logistic distribution or vice versa, and that is often the case for the log-logistic form as well; however, it is unknown if the log-logistic or normal and/or logistic forms provide a more realistic reaction probability estimate in the cases where the log-logistic form deviates significantly, and further exploration is suggested to that end. Thus, for many cases, the most computationally efficient and/or convenient distribution form is suggested when fitting univariate data, such as impact sensitivity tests, until a strong physical bases for a particular distribution form is ascertained.

3.8 Publication disclosure

The majority of the work shown in this chapter was published in the Journal of Energetic Materials in Aug. 2020, with authors Cummock et al. [61].

4. THE INFLUENCE OF MICROSTRUCTURE AND CONFORMATIONAL POLYMORPH ON THE DROP-WEIGHT IMPACT SENSITIVITY OF δ-PHASE HMX

The influence on HMX impact sensitivity resulting from damage due to phase transition versus that of the polymorphic conformer and crystal lattice change in δ-HMX are quantified in this work. Microstructural imaging techniques are used to characterize 30 crystals from three groups of distinctly large and small HMX crystals which have undergone a thermally induced phase transition, as well as some which have undergone spontaneous reversion from $\delta \rightarrow \beta$-phase. It is found that large HMX crystals incur a significant increase in cracks during the transition from $\beta \rightarrow \delta$, while much smaller crystals appear to have no distinguishable increase in voids after undergoing a $\beta \rightarrow \delta$-phase change. Drop-weight impact experiments were performed on 46 to 68 samples from each of six sample types of HMX, three types of which are composed of very small HMX crystals and three of which are composed of large HMX crystals. It is found that small HMX crystals, which do not appear to incur a significant increase in voidspace after undergoing the phase transition, do not have statistically distinguishable changes in drop-weight impact sensitivity between β, δ, or β-reverted phase HMX; however, large crystal HMX impact sensitivity increases significantly when transitioned to δ-phase and furthermore when allowed to revert to β-phase. This indicates that the morphological change is the dominant effect of $\beta \rightarrow \delta$ transformation on impact sensitivity, and that the δ conformer (boat molecular configuration) has little or no effect on the impact sensitivity of HMX.

4.1 Background

The explosive compound, octahydro-1,3,5,7-tetranitro-1,3,5,7-tetrazocine (HMX), is used in numerous applications, and, as such, the understanding of its sensitivity to varying stimuli is of utmost importance. It has been observed in six distinct polymorphic phases:

α has a limited range of stability and has not been observed during the heating of β-HMX [1]; it forms at an evaporating solvent-container interface [2]; its crystal system has been observed as orthorhombic [3], [4].

β is a stable phase at room temperature and pressure, and is the phase usually referred to by the term "HMX" when a polymorphic phase is not specified; its crystal system has been observed as monoclinic [3], [4].

γ is an H_2O-HMX complex [1], also known as a solvomorph, under some conditions [5], [6]; it forms during steam distillation of HMX solutions in various solvents, and on the precipitation of HMX from water-miscible solvents by dilution with water [2]; its crystal system has been observed as monoclinic [3], [4].

δ is usually formed by heating any of the other phases, and has often been observed to be more impact sensitive than β-HMX [2], [7], [8]; its crystal system has been observed as hexagonal [3], [4], although cases where the overall shape is similar to that of β-HMX are not uncommon, e.g., particles produced and imaged by Peterson et al. [29].

ϵ is only observed under very high pressure conditions ($\sim$12 GPa) [9].

ϕ is only observed under very high pressure conditions ($\sim$27 GPa) [9].

Depending on the temperature ramp rate [9], [62] and particle size [63], the phase change from $\beta \rightarrow \delta$ in HMX occurs between 165 and 210 °C at ambient pressures. The $\beta \rightarrow \delta$-phase change includes both a conformational change in the molecule, and a change in crystal packing, which leads to a volume increase and often crystal defects [30], [34], [64]. Some effort has been given to isolating these two changes in order to understand whether the driver in sensitivity difference between δ and β HMX is due to differences in the conformers (boat and chair, respectively [34]), or the microstructural changes caused by the phase change [8], [29]. However, the isolation of the effect from the conformer change on sensitivity and the effect from microstructural changes caused by the phase change has not been successfully carried out.

The increase in impact sensitivity of HMX in its δ-phase has been clearly demonstrated [2], [7], [8]. In a study by Asay et al. [8], β and δ-HMX samples were prepared using several

different methods and were impacted with nominally the same stimulus. The results included high speed images showing the geometry of sample initiation and the radial propagation speed of the reaction front. It was concluded that changes in planar impact sensitivity in a pellet made up of primarily β-HMX relative to a pellet made up of primarily δ-HMX are not due to the physical differences which occur during the phase transition (lattice change, surface damage, void production, etc.). On the other hand, recent studies show that both the morphology and particle size of HMX play a significant role in its impact and friction sensitivity [27], [65], [66]. The influence of morphology is likely due to changes which occur in ease of fragmentation [27], while the influence of particle size has been attributed to a decrease in particle defects with decreased particle size [65], [66]. The idea that the physical defects and microstructural changes incurred by the phase change from β to δ have little or no role in the increased sensitivity of HMX [8] appear to be inconsistent with these findings. This inconsistency could be attributed to the fact that the study by Asay et al. did not vary the stimulus level when performing impact tests, or that another diagnostic would be better adapted to capturing the changes in sensitivity due to changes in morphology.

Additionally, it is important to note that the results shown by Asay et al. [8] conflate the change in bulk porosity and the change in phase in the HMX crystals; i.e., a change in porosity occurred (and perhaps persisted due to some amount of plastic deformation which occurred within the pellet during heating) in both the case where a temporary phase change to δ was induced and where a temporary phase change to δ and then reversion to β was induced. One method for isolating the bulk porosity from the phase change may be to test loose powders.

In summary, upon a thermally induced $\beta \rightarrow \delta$-phase transition in HMX, three changes occur in a particle: (1) the HMX conformer changes from chair to boat, (2) the crystal lattice structure changes from monoclinic to hexagonal, and (3) a volume increase occurs, inducing defects. A fourth change to be considered regards particles within a polymer matrix, as in the case with HMX-based polymer bonded explosives (PBXs), where binder-HMX interface pores may be produced. Yan et al. [30] points out that the added void space from these pores is likely insignificant, although they can grow significantly if a reversion from $\delta \rightarrow \beta$-HMX occurs via storage in a humid environment. Yan et al. observed that β-HMX has been found

to be hydrophobic due to nearly homopolar surfaces [67], while δ-HMX has polar surfaces [68], on which dipole attraction of water could occur [30]. In [30], it is suggested that water was absorbed on the surfaces of the particles or incorporated into microporous regions of the crystalline lattice by capillary condensation. Interfaces between water and HMX may play a significant role in the sensitivity of HMX. It is worth noting that Yan et al. additionally observed that the majority of voids produced in the $\delta \rightarrow \beta$ reversion were of 80 nm diameter or less, assuming spherical pores, and that the increase in total void volume was significant ($\sim$400%).

Although changes (1), (2), and (3) outlined above are closely related, they are likely to be distinct in their effects on the sensitivity of the HMX particle. The objective of this study is to determine the influence on sensitivity of the combined conformer and crystal lattice changes incurred during a $\beta \rightarrow \delta$ phase transition, as well as, independently, the influence of the void space produced during the phase transition, within the weak impact regime (drop-weight tests). Three types of observations are made for each crystal state: (1) features and morphology of a pristine β-HMX crystal, (2) defects, volume increase, and damage incurred upon transition from $\beta \rightarrow \delta$, and (3) any healing or additional cracks, defects, or other damage incurred upon reversion from $\delta \rightarrow \beta$.

4.2 Sample preparation

4.2.1 Comparison of defects induced in small versus large HMX particles

It has been suggested that HMX particles of size 2 μm or less incur fewer and smaller defects upon undergoing a phase change from $\beta \rightarrow \delta$ [27], [65], [66]. One method for verifying this may be to compare drop-weight results of powder from nonbindarized pristine HMX to HMX which has undergone a phase change to δ and then a reversion to β. Another method is to visually compare the microstructural features of small particles of β-HMX to the same crystal after it has undergone transition and reversion. For very small particles, such as Fluid Energy Milled (FEM) HMX, the resolution of a Scanning Electron Microscope (SEM) is needed; with larger particles, this may be done with micro-Computed Tomography (μCT). Specifically, the following procedures were proposed:

1. **Select** a small number of HMX particles in two groups: (1) FEM HMX, and (2) large particle HMX[1]

2. **Perform** CT (on large particles), optical microscopy, and SEM (on small particles) on each selected particle

3. **Thermally induce** a phase transition to δ in half of the samples from each group with a slow heat ramp ($\sim$0.7 K/min) to 180 °C and hold for 1 hour, then rapidly cool to kinetically lock in the δ-phase [14].

4. **Perform** CT (on large particles), optical microscopy, and SEM (on small particles) on each selected particle

5. **Slowly heat** the remaining half of the pristine samples to 180 °C and hold for 1 hour, then slowly cool the particles ($|\text{ramp}| \approx 2.2$K/min) to 120 °C, holding for 3 hour, then allow cooling to room temperature, inducing the $\delta \rightarrow \beta$ reversion (see Fig. 4.4)

6. **Perform** CT (on large particles), optical microscopy, and SEM (on small particles) on each selected particle

7. **Compare** the differences in features between small particles throughout transition and reversion to the differences in large particles throughout transition and reversion

Two DSC trials were run for two different samples of both C3-Upper HMX and FEM-R10 HMX, provided by the AFRL at Eglin AFB. The thermal profile input for the DSC trials was a ramp from room temperature to 180 °C at a rate of 0.6 K/min, and then an 8 hour isotherm at 180 °C. The pans were hermetically sealed once the sample was placed inside. Each DSC sample was $\sim$0.3 mg of HMX. The time traces of each DSC trial are shown in Fig. 4.5.

It was observed that the FEM-R10 HMX requires roughly a 5 hour isotherm after the $\sim$4.2 hour heating ramp from room temperature to 180 °C, while the C3-Upper HMX only

[1]Class 1, 3, or 4 HMX would all be sufficiently larger than the FEM material to expect a significant difference, see Fig. 4.1, 4.2, and 4.3, where PDF indicates the truncated Probability Density Function, and CDF indicates the Cumulative Distribution Function, showing the fraction of particles that are finer than a given sieve mean diameter.

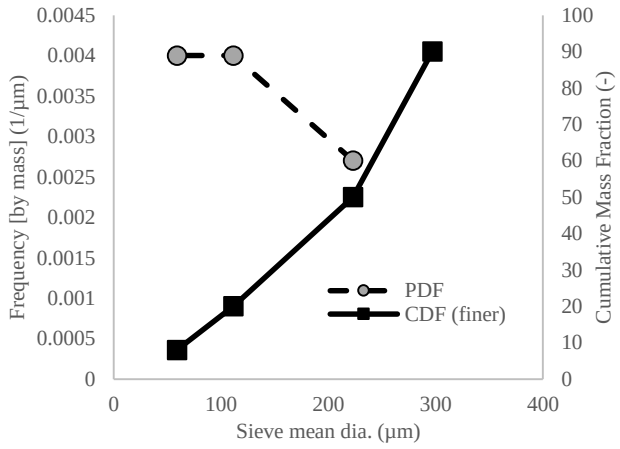

Figure 4.1. HMX class 1 particle size distribution details, based on [69].

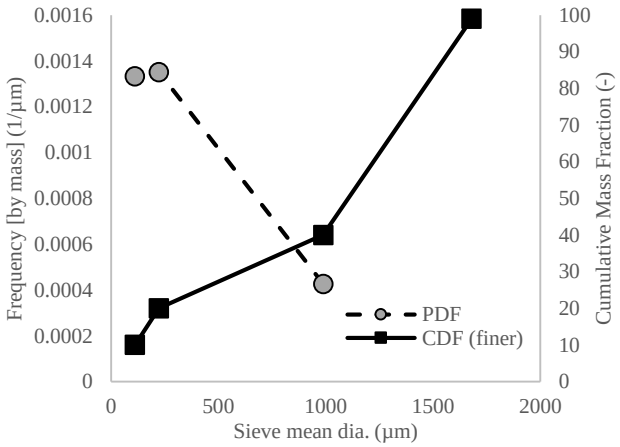

Figure 4.2. HMX class 3 particle size distribution details, based on [69].

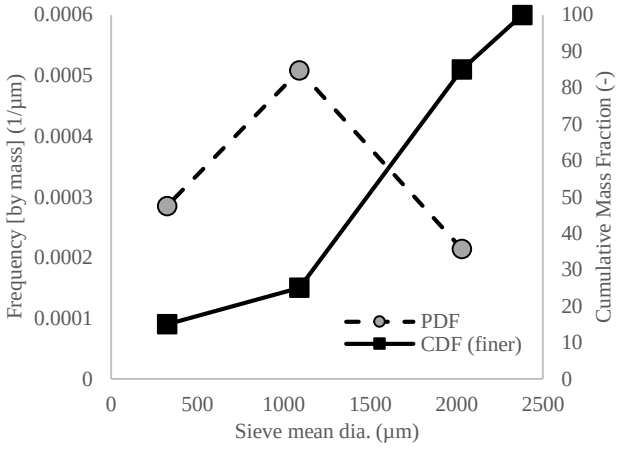

Figure 4.3. HMX class 4 particle size distribution details, based on [69].

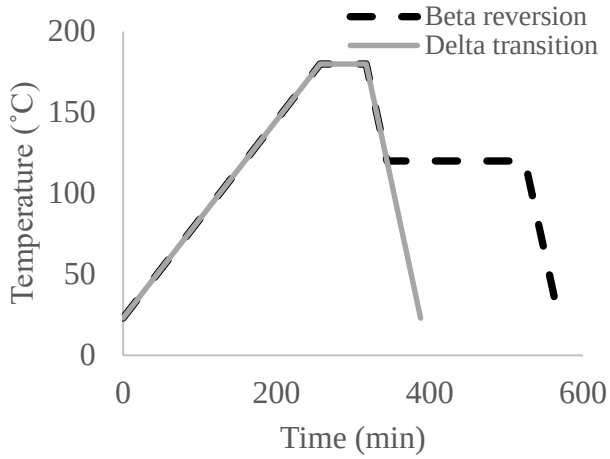

Figure 4.4. Target temperature profiles for inducing a $\beta \rightarrow \delta$ transition (solid grey line) and a $\delta \rightarrow \beta$ reversion (dashed black line).

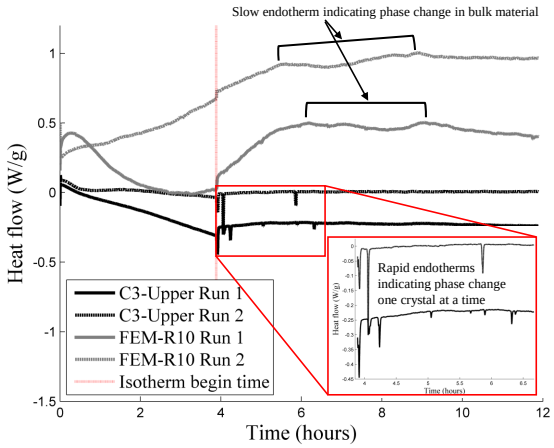

Figure 4.5. DSC traces for two separate samples of C3-Upper HMX and FEM-R10 HMX. Note that in run 2 of C3-upper HMX, exactly three large particles were placed in the DSC pan, where its corresponding trace indicates three distinct endotherms.

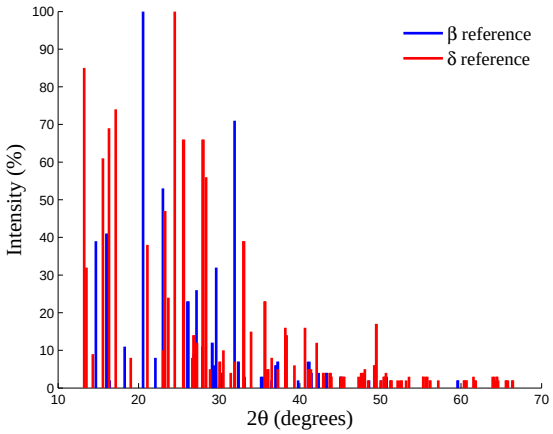

Figure 4.6. Reference XRD peaks for β and δ-phase HMX

requires a ∼2.5 hour isotherm under the same conditions. The FEM-R10 HMX endotherm also tends to be quite slow compared with those of C3-Upper HMX. The samples of C3-Upper HMX had much fewer particles in it, due to its large particle size. In the first run, it was not noted how many particles were a part of the sample, but the second run, precisely three large particles were used as the sample in order to determine if each endotherm 'spike' corresponded to a particle, which appeared to be the case.

The C3-Upper HMX appears to reach a high ratio of δ-phase much earlier on then the FEM-R10 HMX; however, it is proposed that the thermal input for inducing a phase change be defined by the longer required input of the two materials, and then defined and given to all tested materials. This is in order to avoid inputting different amounts of energy into different materials, which may bias the amount of damage induced before and after phase change occurs.

Evidence of the $\beta \rightarrow \delta$-phase change was obtained using X-Ray powder Diffraction (XRD), where FEM-R10 HMX was given similar thermal profiles, but with one varied parameter, the length in time of the isothermal segment at 180 °C. These XRD results are qualitative, but provide a good indication of the phase of the HMX. Future work can include quantifying the amount of each phase indicated by each XRD trace.

Prior to making inferences on each XRD trace, it is informative to take a look at the reference peaks for β [70] and δ-phase [71] HMX. These reference peaks are shown in Fig. 4.6.

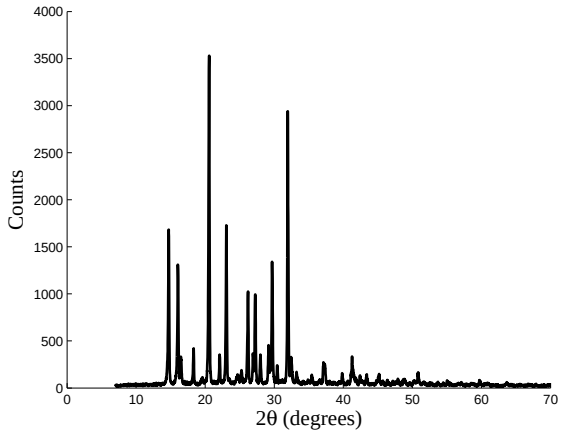

Figure 4.7. Full XRD trace of FEM-R10 HMX after undergoing a one hour isotherm profile and subsequently a slow quench.

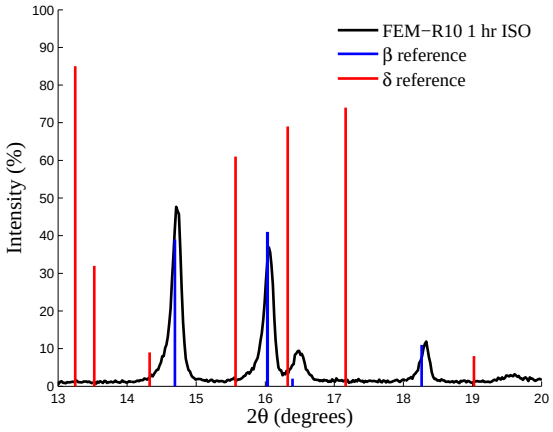

Figure 4.8. Region of interest XRD trace of FEM-R10 HMX after undergoing a one hour isotherm profile and subsequently a slow quench.

Note from Fig. 4.6 that many of the β and δ are very close to overlapping. Most informative may be to pay closest attention to XRD peaks within the range $13° \leq 2\theta \leq 20°$, where fewer nearly overlapping peaks are found. The XRD trace of FEM-R10 HMX after undergoing a thermal profile (see Fig. 4.4) where the quench was slow, such that a $\delta \rightarrow \beta$-phase reversion is expected, is shown in Fig. 4.7 and 4.8. Very little, if any, δ-phase HMX is expected to be detected in this trace, not only due to the short isotherm, but also because much of any δ-phase transition which occurred is expected to revert to β-phase upon the slow quench.

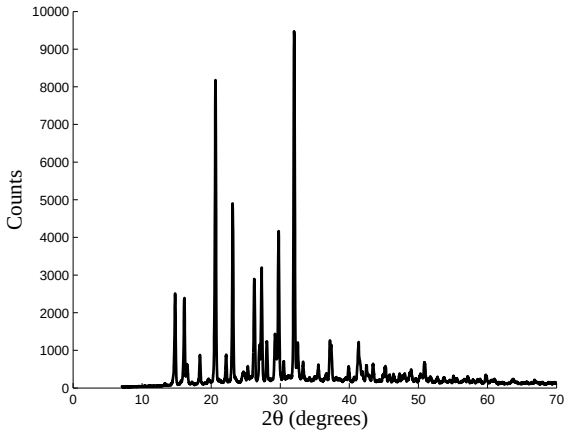

Figure 4.9. Full XRD trace of FEM-R10 HMX after undergoing a one hour isotherm profile and subsequently a rapid quench.

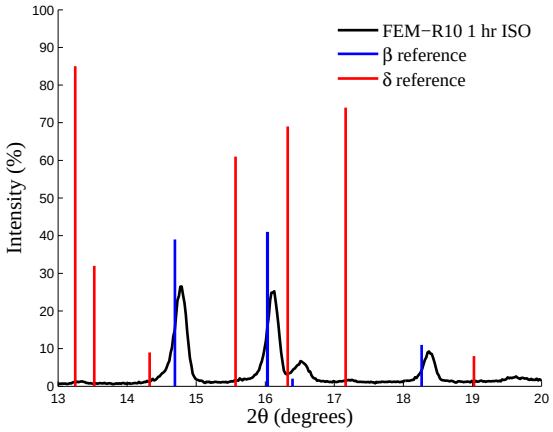

Figure 4.10. Region of interest XRD trace of FEM-R10 HMX after undergoing a one hour isotherm profile and subsequently a rapid quench.

The XRD traces of FEM-R10 HMX after undergoing varying lengths of isotherms are shown in Fig. 4.9, 4.10, 4.11, 4.12, 4.13, and 4.14.

Initially, however, a thermal profile using only a one hour isotherm was used as an input to C3-Upper HMX and FEM-R10 HMX. That thermal profile is shown in Fig. 4.4. Comparison SEM images were taken of the pristine HMX, post heating and rapidly quenching to induce δ-phase and kinetically lock in the phase, and post heating and slowly quenching to induce a phase change to δ and then a phase reversion to β.

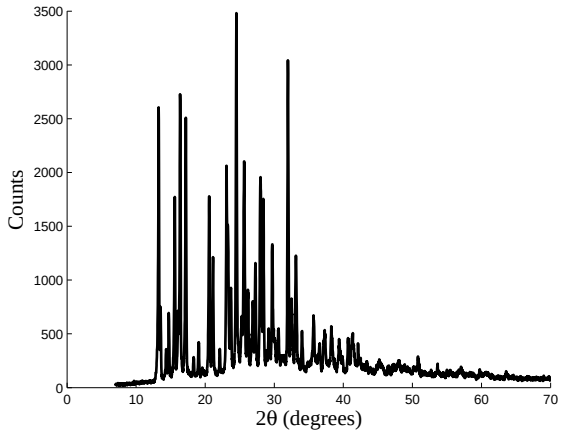

Figure 4.11. Full XRD trace of FEM-R10 HMX after undergoing a three hour isotherm profile and subsequently a rapid quench.

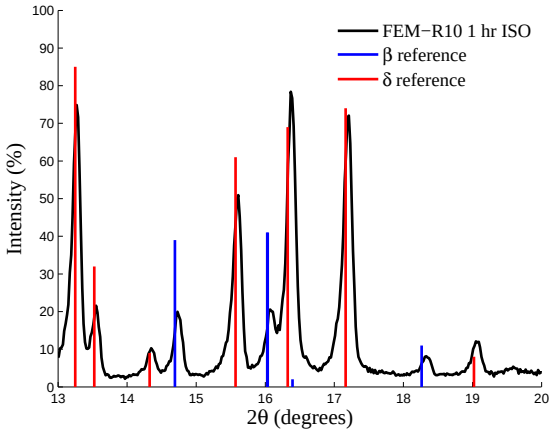

Figure 4.12. Region of interest XRD trace of FEM-R10 HMX after undergoing a three hour isotherm profile and subsequently a rapid quench.

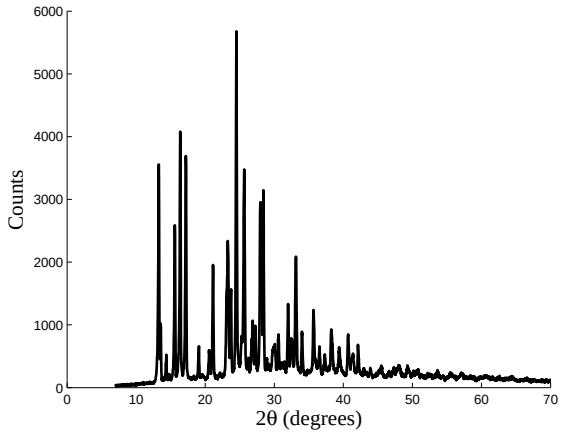

Figure 4.13. Full XRD trace of FEM-R10 HMX after undergoing a five hour isotherm profile and subsequently a rapid quench.

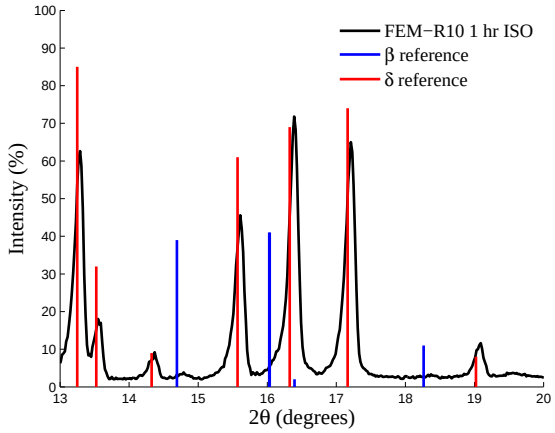

Figure 4.14. Region of interest XRD trace of FEM-R10 HMX after undergoing a five hour isotherm profile and subsequently a rapid quench.

Table 4.1. Description of each sample type used in this work.

Description	Particle size	Label
Pristine β-HMX	small	$\beta_{0,sm}$
Thermally induced δ-HMX	small	δ_{sm}
Thermally induced β-HMX reverted from a short-lived δ-phase transition	small	$\beta_{r,sm}$
Pristine β-HMX	large	$\beta_{0,lg}$
Thermally induced δ-HMX	large	δ_{lg}
Thermally induced β-HMX reverted from a short-lived δ-phase transition	large	$\beta_{r,lg}$

4.2.2 Characterization of a new set of particle size distributions

Because Eglin AFRL failed to provide any materials for this study as originally planned, FEM HMX was acquired at Purdue and characterized. Pure HMX powder was chosen for study. The advantage of using a pure powder form of HMX in this work was that inter-facial defects (crystal-crystal and crystal-binder) are mitigated or eliminated during the phase-transition heating cycles, relative to binderized samples that undergo a heating cycle. Thus, the effects on an individual crystal during phase transition were reduced to (1) a conformer change, (2) a lattice change, (3) a volume change, and (4) internal crystal stresses potentially producing internal voids. Six sample groups were prepared, and they are described in Table 4.1 and given a label which will be used henceforth when referring to a particular sample type.

The two particle size distributions referred to as 'small' and 'large' come from fluid energy milled (FEM) HMX (BAE 4HFEM14-11) and class III HMX (BAE 74BC314-8), respectively, where the class III HMX used had particles smaller than 355 μm excluded via sieving with a number 42 sieve. The particle circular equivalent (CE) diameter distributions of sieved class III HMX and FEM HMX are given in Fig. 4.15. The particle size distributions shown were measured using a Malvern Morphologi G3-ID Particle Shape Analyzer, which measured ~1.2 million FEM particles and ~2,000 sieved class III particles.

The thermal profile used to induce a phase transition in the HMX includes a slow ramp from room temperature to 180 °C at 0.6 K/min, as suggested by Smilowitz et al. [14], to

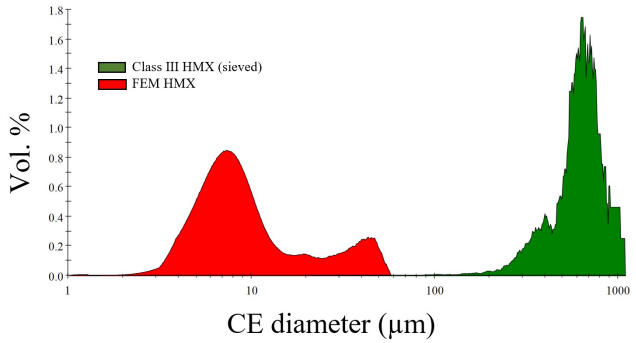

Figure 4.15. Estimated particle size distribution (volume based) of FEM HMX and sieved ($> 355\ \mu m$) class III HMX.

mitigate thermally induced stresses, an isotherm at 180 °C for 10 hours, and a quench to room temperature at 6 K/min. The 10 hour isotherm is excessive for the large particle size of HMX to reach a phase change, but as noted previously [63], the smaller particles require significantly more time at a given temperature to complete a transition to δ-phase, and it was desirable to keep constant the thermal energy input to all of the samples. The thermal input for samples prepared for impact testing was produced by a Tenney TJR Temperature Chamber.

It is of note that samples which underwent a δ-phase transition via the above outlined thermal profile spontaneously reverted to β-phase when left in ambient conditions despite the rapid cooling portion of the heating profile, which has been described as a method to kinetically lock in the metastable δ-phase [14]. This is likely due to contrasting ambient conditions, as it is apparent that humidity has a significant influence on the rate of β-phase reversion from samples that have been kinetically locked in the δ-phase [29], [30]. Thus, samples $\beta_{r,sm}$ and $\beta_{r,lg}$ were heated with the same profile as outlined above, then stored in ambient conditions for 72 hours to allow reversion from δ to β-phase. The β-reverted samples were then heated at 50 °C for 24 hours, and then allowed to cool for 24 hours before impact testing in order to remove any water that may have been trapped within the particles upon reversion from $\delta \rightarrow \beta$-phase. Mitigating the interfacing of external voids with water in the reverted HMX likely inhibited impact sensitivity gains in a study by Peterson et al. [29], where it was observed that β-reverted HMX had a very similar impact sensitivity to pristine β-HMX.

Evidence that samples were successfully transitioned to δ-phase, remained δ-phase during impact testing, and reverted to β-phase when expected was crucial. Several samples were treated with the thermal profile discussed above and their diffraction patterns were collected at different points in time in order to assess the reversion rate to β-phase under vacuum desiccated conditions and ambient conditions, where ambient relative humidity exceeded 60%. Diffraction patterns were collected via powder X-Ray Diffraction (XRD) using a Panalytical Empyrean Powder X-Ray Diffractometer. Crystallographic Information Files (CIFs) from the Cambridge Crystallographic Data Centre (CCDC) were used to quantify the ratio of β, δ, ϵ, and γ -phases represented in each XRD pattern via Rietveld refinement, and the

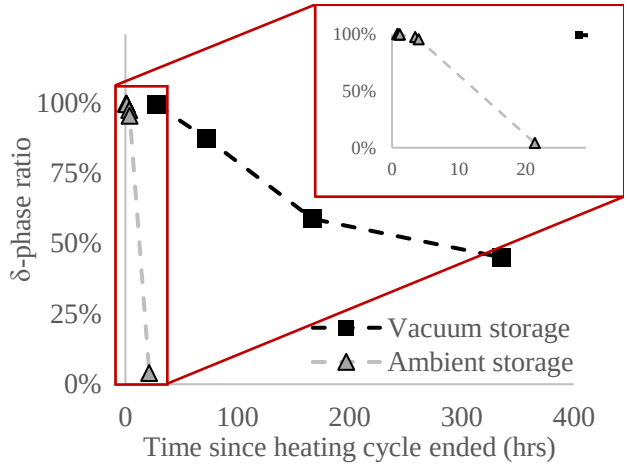

Figure 4.16. δ-phase ratio within HMX powders as determined by Rietveld refinement conducted on XRD patterns.

resulting ratio of δ-phase HMX estimated to be in each sample is shown in Fig. 4.16. It was found that the only phases that were present in significant amounts were β and δ, as was expected; i.e., of the other phase ratios estimated, the amount present was typically well below 1%. The CIF codes associated with the phase ratio estimates made were β, δ, ϵ, and γ -phases are found in Cambridge Structural Database (CSD) OCHTET04, OCHTET03, OCHTET22, and DEDBUJ, respectively.

It is clear from Fig. 4.16 that vacuum desiccated storage extends the life of the δ-phase HMX relative to storage in humid ambient conditions. Further XRD measurements of δ-HMX samples that were transitioned using a thermal profile with varied isotherm lengths provided further evidence that samples stored in a vacuumed desiccator remained primarily δ-phase for at least 28 hours after the heating cycle ended; however, samples stored in ambient conditions began to revert to β-phase in significant amounts only four hours after the heating cycle ended. Thus, samples which were intended to be in the δ-phase upon impact testing were tested within six hours of the heating cycle ending, and each sample was stored under vacuum in a desiccator until immediately before being subjected to its impact test.

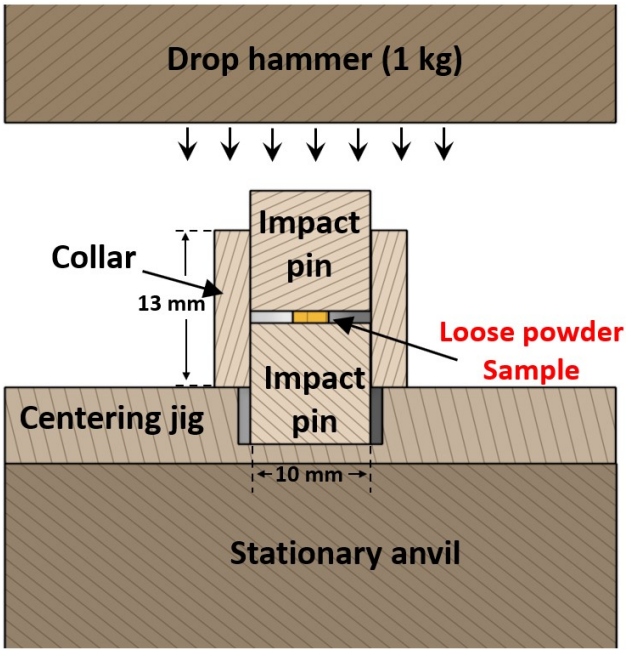

Figure 4.17. Schematic of BAM drop-weight impact test design, where the sample is a loose HMX powder.

4.3 Experimental methods

The six sample types referred to in Table 4.1 were prepared for impact testing with a BAM Fall Hammer-10 impact sensitivity tester (see Fig. 4.17 for a schematic of the BAM configuration). Large particle samples ($\beta_{0,lg}$, δ_{lg}, and $\beta_{r,lg}$) were prepared for X-ray computed tomography (XCT) imaging using a Bruker Skyscan 1272, and small particle samples ($\beta_{0,sm}$, δ_{sm}, and $\beta_{r,sm}$) were prepared for focused ion beam (FIB) sectioning and polishing and subsequent scanning electron microscopy (SEM) imaging of FIB polished cross-sections using a Thermo Fisher Scientific Helios G4 UX DualBeam. The XCT resolution is too limited (approximately 1.0 μm/pixel) to distinguish defects in the small HMX crystals, but was a cost effective method for imaging large crystals, while the SEM is capable of imaging at $<$ 1.7 nm/pixel, which was sufficient for microstructural analysis of the small particles.

It was expected that the small particles would undergo relatively less void production when compared with large particles upon $\beta \rightarrow \delta$-phase transition and $\delta \rightarrow \beta$ reversion [65], [66]; a carefully designed set of impact experiments would be able to do both of the following:

a) Determine if small particle void production was in fact less significant (at least in the case of voids which influence impact sensitivity) than their larger particle counterparts and

b) Quantify the influence of the δ-conformer on impact sensitivity relative to the change in microstructure which occurs upon heating and phase transition.

The hypothesis test matrix that was designed to explore the above points is shown in Table 4.3, where the test descriptions operate under the assumption that there is not significant void production in small particles upon heating and phase transition, while large particles undergo significant void production both upon heating to δ-phase and reversion to β-phase. Non-significant void production here refers to a case where (1) relatively fewer voids are produced upon phase transition, or (2) voids that are produced upon phase transition which are likely too small to have an influence on the sample's impact sensitivity.

Note that there is importance in the particle size and the system (powdered or binderized) chosen for testing. Assuming that very small HMX crystals will experience little increase in defects upon phase transition [27], [65], [66], see Table 4.2, which details the expected changes which a particle or system undergoes upon phase transition and reversion. In Table 4.2, 'pre' under 'Phse. Trans.' indicates that the powder undergoes the phase change before pressing into pellet form, and 'post' under the same column indicates that the powder undergoes the phase change after pressing into pellet form. Also note that it has been concluded that an insignificant amount of void production occurs in a binderized HMX system upon β-δ transition, but that a significant amount of voidspace is created near the binder-HMX interface and within HMX crystals upon $\delta \rightarrow \beta$ reversion via storage in a humid environment. Note that inducing reversion via slow cooling in a dry environment could induce different behavior. A test matrix is suggested in Table 4.3 based on the assumptions shown in Table 4.2. In Table 4.3, hypothesis testing is also noted, where H_0 represents the null hypothesis.

A minimum of 46 loose HMX powder samples, and up to 68 samples, were impact tested for each sample type shown in Table 4.1. Previous experiments using the same impact apparatus showed that the impact sensitivity of loose powder class III HMX samples with masses of 10, 13, and 20 mg had statistically indistinguishable impact sensitivity, based on

Table 4.2. A list of the effects of $\beta \rightarrow \delta$-phase transition/reversion in varying systems of HMX

System	**Partic. size**	**Phse. Trans.**	**Conformer chng.**	**Vol. chng.**	**Cryst. defects**	**Interfacial defects**
Pure powder	small	$\beta \rightarrow \delta$	chair to boat	$\uparrow$	insig. chng.	N/A
Pure powder	small	$\delta \rightarrow \beta$	boat to chair	$\downarrow$	insig. chng.	N/A
Pure powder	large	$\beta \rightarrow \delta$	chair to boat	$\uparrow$	sig. chng.	N/A
Pure powder	large	$\delta \rightarrow \beta$	boat to chair	$\downarrow$	further sig. chng.	N/A
Binderized	small	$\beta \rightarrow \delta$	chair to boat	$\uparrow$	insig. chng.	insig. chng.
Binderized	small	$\delta \rightarrow \beta$	boat to chair	$\downarrow$	insig. chng.	some increase
Binderized	large	$\beta \rightarrow \delta$	chair to boat	$\uparrow$	sig. chng.	insig. chng.
Binderized	large	$\delta \rightarrow \beta$	boat to chair	$\downarrow$	further sig. chng.	sig. increase

Table 4.3. Test matrix of impact sensitivity experiments.

Label	**Phase history**	**Test description**	**Hypothesis test**
$\beta_{0,sm}$	β	Control	N/A
δ_{sm}	$\beta \rightarrow \delta$	Compare with $\beta_{0,sm}$ results and test for sensitivity difference due to chair (β) and boat (δ) conformers	$H_{0,1}$: $L50_{\beta_{0,sm}} = L50_{\delta_{sm}}$
$\beta_{r,sm}$	$\beta \rightarrow \delta \rightarrow \beta$	Compare with $\beta_{0,sm}$ results to determine if insignificant void production occurs in small particles	$H_{0,2}$: $L50_{\beta_{0,sm}} = L50_{\beta_{r,sm}}$
$\beta_{0,lg}$	β	Control	N/A
δ_{lg}	$\beta \rightarrow \delta$	Compare with $\beta_{0,lg}$, then compare the difference between $\beta_{0,lg}$ and δ_{lg} to the difference between $\beta_{0,sm}$ and δ_{sm} to quantify influence of voids produced by the phase change	$H_{0,3}$: $L50_{\beta_{0,lg}} = L50_{\delta_{lg}}$, $H_{0,4}$: $L50_{\beta_{0,lg}} - L50_{\delta_{lg}} = L50_{\beta_{0,sm}} - L50_{\delta_{sm}}$
$\beta_{r,lg}$	$\beta \rightarrow \delta \rightarrow \beta$	Compare with $\beta_{0,lg}$ to verify that significant void production occurs in large HMX crystals during phase transition & reversion	$H_{0,5}$: $L50_{\beta_{0,lg}} = L50_{\beta_{r,lg}}$

their probability density functions (PDFs); however, similar HMX samples with a mass of 35 mg exhibited a statistically significant decrease in impact sensitivity compared with their lower mass counter parts. The precision of each mass measurement was ±1.0 mg, and 25 samples of each mass were tested. The decrease in impact sensitivity with increased mass may be a result of a larger number of particles being wedged between the BAM impact pins and their collar, increasing the sliding friction of the pins and thus decreasing the energy input into the bulk of the sample for the same drop-weight heights.

For this reason, all of the samples shown in Table 4.1 were measured to a mass of 15 mg ± 2.5 mg for impact testing. An image of a sample prior to impact is shown in Fig. 4.18, and post-impact images of examples of a 'go' and a 'no-go' result are shown in Fig. 4.19 and 4.20, respectively. All of the samples were impact tested with the 1 kg drop-weight, as shown in Fig. 4.17, and the BAM impact pins are cleaned using acetone and Kimwipes™ between each test. Because the results of the drop-weight test are inherently binary (go/no-go), the Neyer SenTest™ [57], [72] was used to sequentially determine the stimulus heights at which to test in order to efficiently determine the statistical estimators (μ and σ) used to construct a normal distribution for each sample type. The confidence level that each sample type's impact sensitivity L50 (μ) was different from the L50 of any other sample type was calculated, and a confidence of greater than 95% between any two sample's μ estimator was assumed to be statistically significant. However, it is well known that particle size has a significant influence on impact sensitivity, thus, direct comparisons between the small particles' PDFs and the large particles' are not made in this study, rather indirect comparisons which stem from differences between samples of the same particle size are examined.

The Neyer SenTest™ was used both to sequentially determine the stimulus levels (heights) from which to drop the 1 kg weight for each sample, and to calculate the CDF estimators, confidence intervals, and p-values which determine whether there was a statistical difference between the population or not.

Figure 4.18. An HMX sample placed on a BAM pin surrounded by its collar prior to impact testing. The BAM pin diameter is 10 mm.

Figure 4.19. An example of a 'go' after an impact test.

Figure 4.20. An example of a 'no-go' after an impact test.

4.4 Results and discussion

4.4.1 X-ray computed tomography

Large particle HMX (sieved class III) takes significantly more time to mill via FIB than do the fine particles (FEM). Use of XCT for the identification of void and damage production during the phase transition and reversion process was useful for large particles and their associated microstructural changes throughout phase changes, as this technique is a nearly non-intrusive method for obtaining three-dimensional volume information about the sieved class III particles being measured.

For the $\beta_{0,lg}$ sample, a small container holding a few hundred sieved class III HMX crystals at a poured density were XCT imaged and a two-dimensional cross-section was randomly chosen from each of six separate segments of the sample via a random number generator. Five crystals in each of these cross-sectional images were then randomly chosen for quantitative analysis, resulting in quantitative analysis of the microstructure of 30 HMX crystals.

An identical method was followed for the δ_{lg} and $\beta_{r,lg}$ samples, except after scanning the δ_{lg} sample, it was allowed to remain undisturbed in the XCT apparatus for 120 hours—enough time for a β-reversion to occur—before beginning another XCT scan. In this way, a direct comparison of the same crystals in δ-phase and β-reverted phase could be attempted. As such, the images and crystals chosen for analysis from δ_{lg} were randomly selected, and images and crystals selected from $\beta_{r,lg}$ were chosen to be the same crystals at the same cross-sectional height selected in δ_{lg}. It should be noted, however, that significant changes in shape, spatial shifting, and breakage of the crystals appeared to occur during the reversion from δ to β-phase, sometimes to the point that the crystal was not recognizable, and as such a best guess was made using the centroid location of the crystals in each image to determine which crystal corresponded to which; i.e., if the centroid of a δ-phase crystal was close enough to that of a β-reverted crystal and had a shape and size that appeared to be a feasible derivative of the δ-phase crystal and if nearby crystals exhibited similar shifting or were newly visualized near breakage sites in β-reverted crystals, a crystal may be assumed to be the same in the δ and β-reverted image slices. An example is shown in Fig. 4.21, where

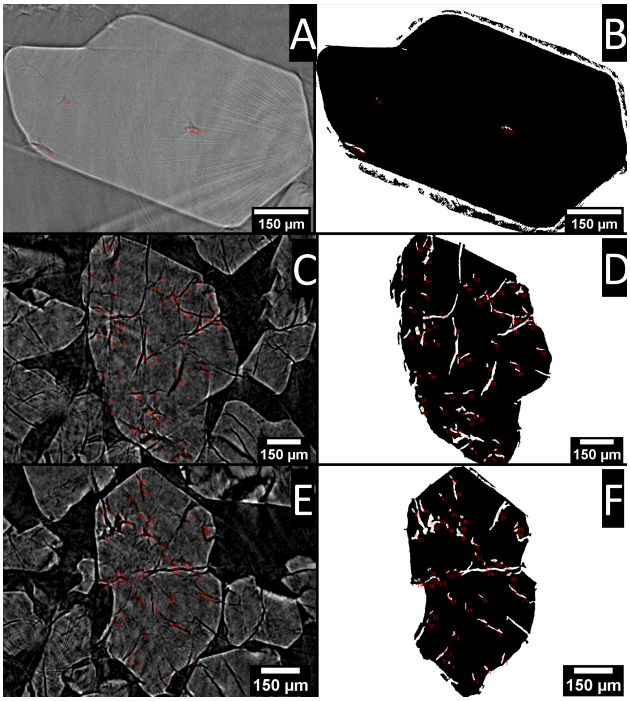

Figure 4.21. Select reconstructed cross-sectional images from XCT scans, where A, C, and E show the originally reconstructed images of $\beta_{0,lg}$, δ_{lg}, and $\beta_{r,lg}$, respectively. Images B, D, and F represent the binarized versions of A, C, and E, respectively. The red crosses and corresponding numbers show the centroids of each void, which were used in labelling the voids as either pores or cracks.

the centroid shift was approximately 42 μm down and to the right in the XCT cross-sectional image upon reverting from δ to β-phase.

Analysis of each randomly selected cross-section of a given crystal followed the workflow shown in Fig. 4.22, where some of the steps shown are manual (grey boxes) and others were automated (blue boxes). A binarization threshold was manually chosen for each randomly selected image, to best reflect apparent voids seen in the raw reconstructed images. Because the scanning parameters were kept constant across the scans for each dataset, the threshold value for binarization did not need much adjustment from image to image (40 kV voltage, 250 μA current, 5.5 second exposure time), but there are other less-easily controlled parameters which can have a slight effect on image brightness, such as ambient temperature and relative humidity, and thus, the appropriate threshold value.

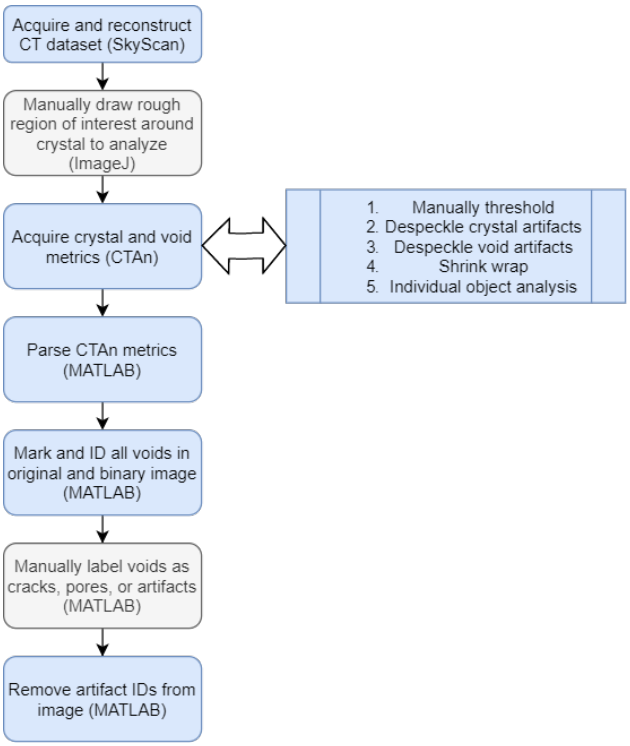

Figure 4.22. The flow of the microstructural analysis used in this work, where the software used for each step is shown in parentheses. Any voids labelled as artifacts are not included in the porosity calculations; i.e., they're treated as solid portions of the crystal.

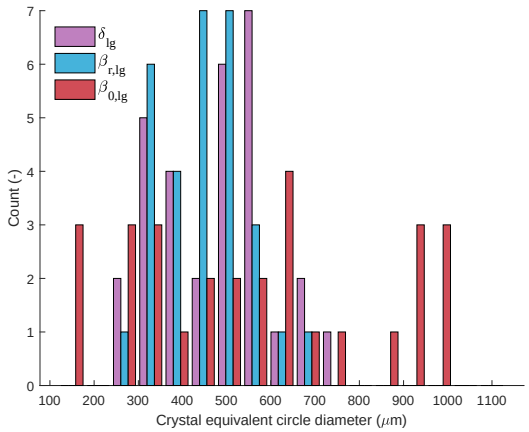

Figure 4.23. Representation of the area of the crystal cross-sections which were randomly selected from datasets $\beta_{0,lg}$ and δ_{lg} (where crystals selected for analysis of $\beta_{r,lg}$ were chosen based on the random selections of δ_{lg}). There appears to be little difference between the sizes of crystals selected on average.

The sizes of all the crystals analyzed were compared (Fig. 4.23) in order to verify that similarly sized crystals were scrutinized across each sample type. Again, each distribution in Fig. 4.23 represents 30 different randomly selected crystal cross-sections. The porosity due to voids labelled as pores (Fig. 4.24) and the porosity due to voids labelled as cracks (Fig. 4.25) were then compiled, where there appears to be minimal increase in the proportional area of pores when a crystal transitions to δ or incurs a reversion from δ to β, but a clear increase in proportional crack area occurs upon the transition to δ-phase.

4.4.2 Scanning electron microscopy

In order to obtain information about the small (FEM) HMX particle microstructure, crystals from this particle size distribution were aerated onto double-sided carbon tape and sputter-coated with an approximately 50 nm thick layer of Pt/Pd mixture, and then imaged via SEM. It was found that the majority of the particles resided in large agglomerate groups; these groups were sectioned and polished using a FIB at 30 kV and 0.44–9.1 nA in order to efficiently obtain a number of cross-sections from which to gather microstructural information. In order to avoid charging and SEM interaction with the small particles, which proved to be sensitive to the electron beam, SEM imagine parameters were 2–3 kV at 0.1–0.2 nA.

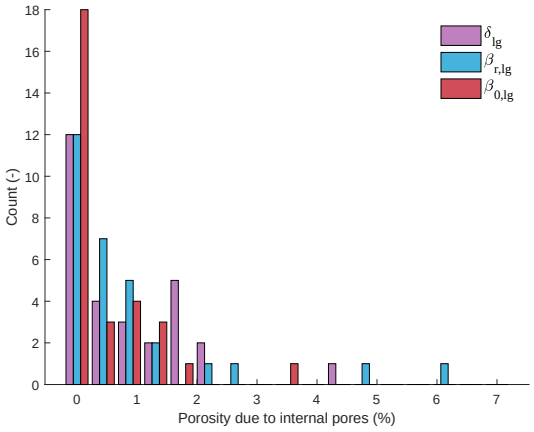

Figure 4.24. Porosity due to voids labelled as pores appears to undergo very little change upon transition to δ-HMX or reversion to β-HMX in large HMX crystals.

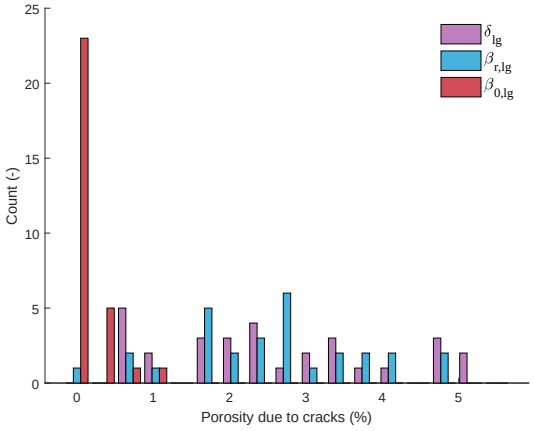

Figure 4.25. A significant increase in porosity due to cracks in both δ crystals and β-reverted crystals occurs in large HMX crystals.

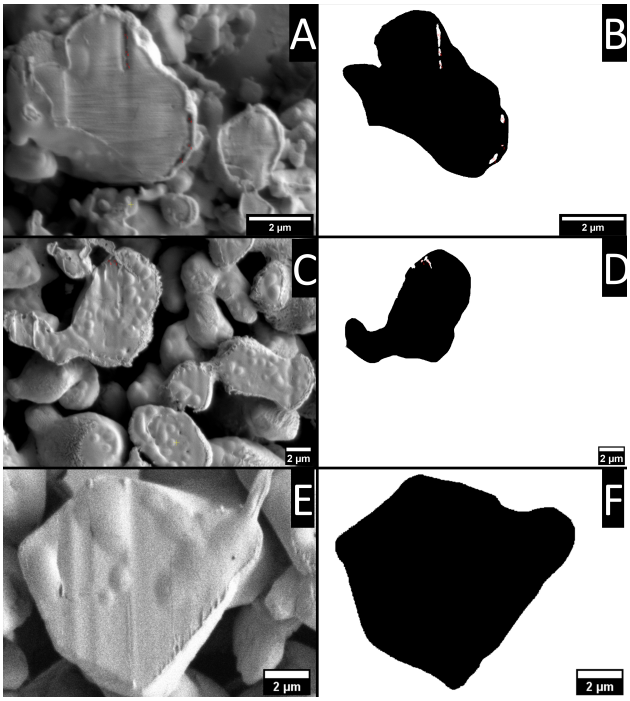

Figure 4.26. Select FIB polished cross sections of FEM HMX, imaged via SEM, where A, C, and E show the raw SEM images (Everhart-Thornley Detector) of $\beta_{0,sm}$, δ_{sm}, and $\beta_{r,sm}$, respectively. Images B, D, and F represent the binarized versions of A, C, and E, respectively. The red crosses and corresponding numbers show the centroids of each void, which were used in labelling the voids as either pores or cracks.

A similar workflow was used to analyze FEM HMX microstructural features as is shown in Fig. 4.22. Example SEM images of FIB polished cross-sections and their associated binarized crystal cross-section of interest are shown in Fig. 4.26.

The sizes of the FEM crystals analyzed are shown in Fig. 4.27, where it can be seen that the size of the 30 analyzed δ_{sm} and $\beta_{r,sm}$ crystals tended to be slightly larger than those of $\beta_{0,sm}$, though still within the expected size range based on particle size distribution data shown in Fig. 4.15. Additionally, the porosity due to pores and cracks is shown in Fig. 4.28 and 4.29, respectively, where it is clear that there is minimal difference in pore or crack porosity between any of the three sample types.

A noteworthy difference between the small (FEM) HMX crystals and the large (sieved class III) HMX crystals is exhibited in Fig. 4.30, where the ratio of perimeter to diameter of each crystal is calculated, which is similar to a measure of roughness for a given crystal.

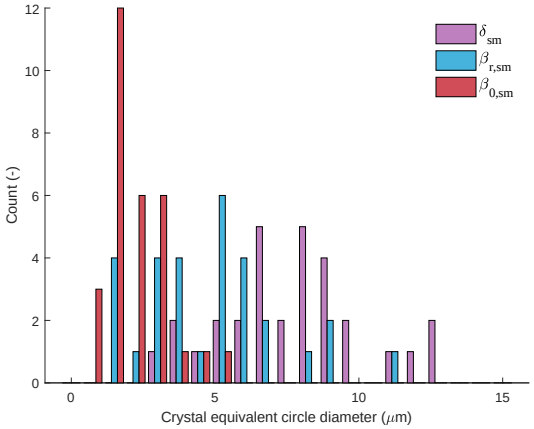

Figure 4.27. Representation of the area of the crystal cross-sections which were randomly selected from images of $\beta_{0,sm}$, δ_{sm}, and $\beta_{r,sm}$. A slight increase in cross-sectional area is apparent between the pristine sample and its corresponding thermally insulted samples.

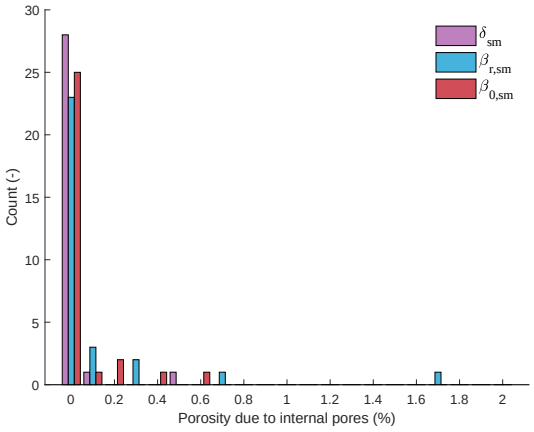

Figure 4.28. Porosity of small HMX crystals due to voids labelled as pores, where no significant difference is noted between sample types.

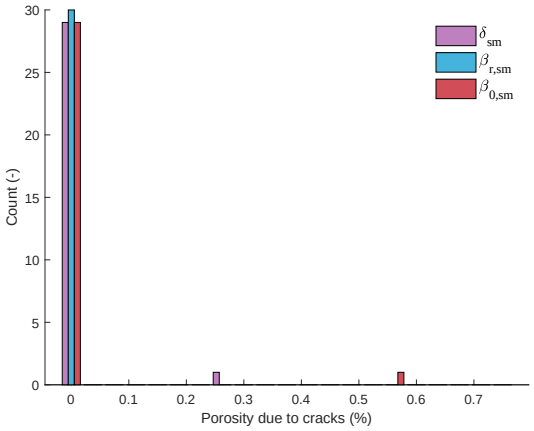

Figure 4.29. Porosity of small HMX crystals due to voids labelled as cracks, where no significant difference is noted between sample types.

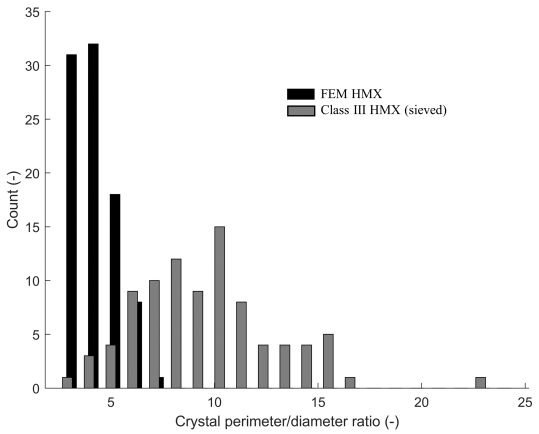

Figure 4.30. Perimeter to diameter ratio of small (FEM) HMX crystals compared with that of large (sieved class III) HMX crystals.

No notable difference was seen between pristine β, δ, or β-reverted samples, however, large crystals appear to have an increased perimeter/diameter ratio, which may play a significant role in sensitivity.

4.4.3 Drop-weight impact tests

The cumulative distribution functions (CDFs) resulting from impact tests of all of the samples described in Table 4.1 with their corresponding 95% confidence regions for the small HMX crystal samples and the large HMX crystal samples are shown in Fig. 4.31 and 4.32, respectively. Very little difference in the μ (also known as the L50) or σ is apparent in the small HMX crystal impact sensitivity distributions, while statistically significant differences in impact sensitivity are clear in the large HMX crystal impact sensitivity distributions, showing a sensitivity ranking of $\beta_{r,lg} > \delta_{lg} > \beta_{0,lg}$. A standard α level of 0.05 was chosen for each hypothesis test shown in Table 4.3, meaning that a p-value less than $\alpha = 0.05$ resulted in rejection of the null hypothesis, H_0. The p-values corresponding to these differences are shown in Table 4.4.

These results are in contrast to work by Peterson et al. [29], where it was found that pristine β-HMX and reverted β-HMX had very similar impact sensitivities, with the β-reverted sample yielding the higher L50 (5% decrease in impact sensitivity by height). Notable dif-

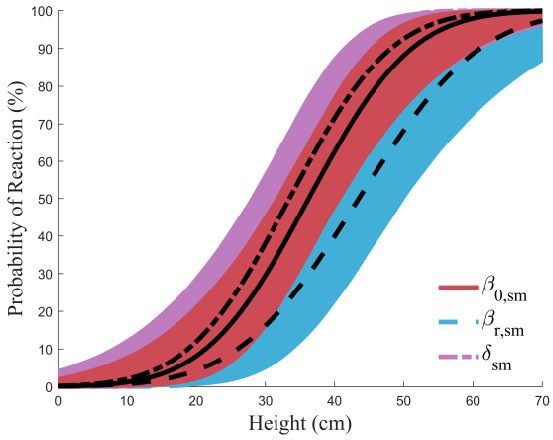

Figure 4.31. CDFs for the small crystal HMX impact results. Black lines represent the center of each CDF, while colored regions represent the 95% confidence region for the associated sample and center CDF. All drop tests were performed with a 1 kg drop-hammer.

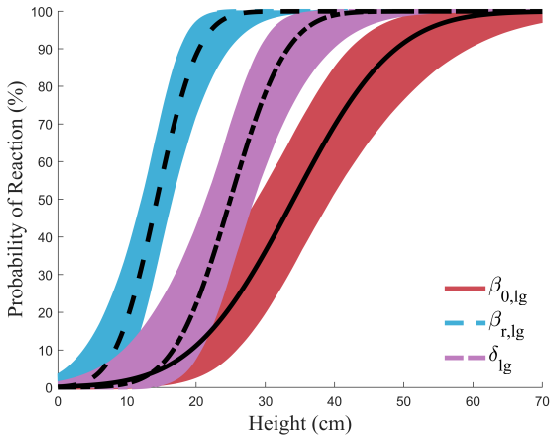

Figure 4.32. CDFs for the large crystal HMX impact results, with their corresponding 95% confidence regions. All drop tests were performed with a 1 kg drop-hammer.

Table 4.4. Hypothesis test results with their corresponding p-values. The p-value of $H_{0,4}$ is assumed to be equal to that of $H_{0,3}$ because $H_{0,1}$ was not rejected, and thus $L50_{\beta_{0,sm}} - L50_{\delta_{lg}} \approx 0$.

Hypothesis test	**Result**	**p-value**
$H_{0,1} : L50_{\beta_{0,sm}} = L50_{\delta_{sm}}$	Not rejected	0.254
$H_{0,2} : L50_{\beta_{0,sm}} = L50_{\beta_{r,sm}}$	Not rejected	0.172
$H_{0,3} : L50_{\beta_{0,lg}} = L50_{\delta_{lg}}$	Rejected	0.00271
$H_{0,4} : L50_{\beta_{0,lg}} - L50_{\delta_{lg}}$ $= L50_{\beta_{0,sm}} - L50_{\delta_{sm}}$	Rejected	$\sim$0.00271
$H_{0,5} : L50_{\beta_{0,lg}} = L50_{\beta_{r,lg}}$	Rejected	$\sim$0

ferences between this work and that of Peterson et al. are that the particle size distribution used was not reported in [29], though it was reported that HMX-C was used, and SEM images were taken of bulk samples, which appeared to indicate that most of the particles were roughly 100 μm or less, which is significantly smaller than the large particles used in this study, and significantly larger than the small particles used in this study. Additionally, Peterson et al. stored pure HMX powder in varying conditions after forcing phase transition to δ and kinetically locking the phase by rapid cooling. It was shown using Raman spectroscopy that the HMX which was stored in an environment with high relative humidity and ambient temperature reverted to β-phase within 24 hours. This conclusion was confirmed in a more recent study by Yan et al. [30]. It was also found by Yan et al. [30] that water was present in the reverted β-HMX samples. This was likely due to the sample storage in humid environments. It is expected that the presence of water in the reverted β-HMX samples had a significant effect on the impact sensitivity results. In this study, samples were allowed to revert to β-phase under ambient conditions, after which they were dried for 24 hours at 50 °C in order to remove water from the β-reverted samples before impact testing. Additionally, it appears that a uniform PDF, also known as a rectangular distribution, was assumed for the distributions estimated in [29]; a more realistic distribution function would be a Gaussian, logistic, or log-logistic, which have all been suggested in the literature [42], [48], [54]. Note that it has been shown that for impact sensitivity of many pure and binderized explosives, often the type of distribution function chosen between Gaussian, logistic, and log-logistic has little to no effect [61].

No direct comparisons are attempted in hypothesis testing between the large HMX crystal samples and the small HMX crystal samples, since it is well known that the bulk microstructure is altered with a change in particle size. It is notable, however, that $\beta_{0,lg}$ had no statistically distinguishable difference in impact sensitivity compared to all of the small crystal HMX sample types. This can be seen clearly in Fig. 4.33, where the 95% confidence region of both μ and σ is displayed via a single contour for each sample type.

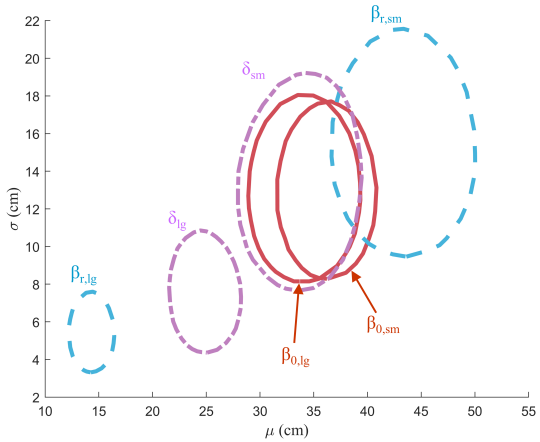

Figure 4.33. Each contour represents the 95% confidence region; any μ-σ combination that falls within a given contour represents a normal PDF that is considered here to be a viable option for representing the true distribution of the population of samples. All drop tests were performed with a 1 kg drop-hammer.

4.5 Limitations

Although implicit bias for analysis of CT and SEM images was mitigated via slice and particle randomization, there are areas where bias could not be avoided. For instance, manual labelling of voids as cracks or pores was performed, based on the shape of voids, and the author's intuition was relied upon for proper labelling of these voids. Because this metric of whether or not a void is a crack or a pore is fairly simple, the voids tend to be easily distinguished as such; however, as volume of the analysis increases and parameter characterization becomes more complex, implicit bias could certainly become a significant factor. This is an opportunity for machine learning to be of use both in terms of analysis efficiency and elimination of human bias in labelling and other forms of characterization.

Additionally, the surface roughness of BAM impact pins may play a role in these results. Prior to this work, a brief attempt was made to test the effects of brand new, smooth surface impact pins versus pins which had been used for many impact tests, and it appeared that the effect was marginal. As such, impact pins were cleaned thoroughly with acetone and tissue between tests, but not exchanged for new pins. A more detailed study on the effect of the surface roughness of the impact pins on impact sensitivity results would certainly be useful.

4.6 Conclusions

X-ray diffraction results indicated that a ten hour isotherm at 180 °C was sufficient to induce a near 100% $\beta \rightarrow \delta$-phase transition in FEM HMX, where its particle size distribution was centered at approximately 10 μm; however, under ambient conditions ($\sim$24 °C, $\sim$60% relative humidity), significant phase reversion to β-HMX occurred within four hours. Placing the δ-HMX in a vacuum desiccated environment resulted in slowing the phase reversion such that the samples remained approximately 100% δ-phase for more than 23 hours.

X-ray Computed Tomography (XCT) and microstructural analysis were performed on 30 large crystals of HMX from each of three sample types ($\beta_{0,lg}$, δ_{lg}, and $\beta_{r,lg}$), and it was found that a statistically significant increase in porosity due to cracks formed upon the δ-phase transition occurred, while porosity due to voids labelled as pores remained approximately

the same for all three large of the sample types. Significant spatial shifting, changes in shape, and damage appeared to occur in a δ-phase sample when allowed to revert to β-phase without disturbance over the course of 120 hours, but void analysis did not show a significant increase in porosity due to pores or cracks in the crystals which underwent the reversion. It is of note that Yan et al. [30] concluded that pores of 80 nm on average were produced in crystals upon reverting from δ-phase to β-phase, but it would appear from these results that the assumption of spherical pores would not be appropriate, as most of the voids produced are in the form of cracks rather than roughly spherically shaped pores.

The small crystal HMX samples were imaged via focused ion beam (FIB) sectioning and polishing, and subsequent imaging via scanning electron microscope (SEM), due to the increased resolution required both to distinguish the crystals themselves and the voids within the crystals. It was found, as was hypothesized in [65], [66], that these very small particles produced few distinguishable voids when thermally induced to undergo a δ-phase transition, in contrast to the behavior of the large crystal HMX samples which received the same thermal treatment. This was true as well for the samples which had been transitioned to δ-phase and subsequently allowed to spontaneously revert to β-phase.

Finally, five hypotheses were tested via an impact sensitivity study of large and small crystal HMX samples in the pristine β, thermally induced δ, or β reverted states. The mass of each sample was stringently controlled to 15 mg $\pm$ 2.5 mg to mitigate effects of the sample mass, and the drop-height results of 46 to 68 samples per sample type were used to calculate the PDF estimators (μ and σ) for the six sample types. It was found that there was no statistically distinguishable difference between any of the small HMX crystal samples ($\beta_{0,sm}$, δ_{sm}, and $\beta_{r,sm}$), indicating that the δ conformer (boat molecular configuration) plays little or no role in the impact sensitivity of HMX, and corroborating evidence that microstructural changes upon δ-phase transition and β-reversion in the small crystals are insignificant, or that they play little or no role in the small crystals' impact sensitivity. However, a significant difference in impact sensitivity was apparent between each of the three large crystal HMX sample types ($\beta_{0,lg}$, δ_{lg}, and $\beta_{r,lg}$). Coupled with the evidence from XCT results that a significant increase in porosity due to cracks occurs upon the δ-phase transition in the large HMX crystals, the results of the hypothesis testing indicate that the change in microstructure

is the primary driver of the increase in impact sensitivity in this case, and more specifically, the change in microstructure mostly due to growing and propagating cracks, rather than pores.

The large crystal β-reverted HMX also incurs a significant increase in impact sensitivity relative to the large crystal δ-HMX, even though a significant increase in crystal size and porosity due to cracks or pores was not apparent in the 30 crystals analyzed. This may indicate that another complex factor, such as crystal or pore shape, has a significant effect on impact sensitivity, as it was noted that significant spatial shifts, changes in crystal shape, and crystal breakage occurred in a single sample of large HMX crystals when allowed to revert to β-HMX in an undisturbed environment over 120 hours. Further study of changes in crystal and pore shape upon thermal insult implementing methods such as those employed by Mares et al. [73] would be useful for determining the role that crystal and pore shape play in impact sensitivity.

Additionally, further work to determine the influence on impact sensitivity due to water contamination in HMX should be conducted, because water likely contributes to the desensitization of β-reverted HMX, based on the contrast between the results of this work and those of Peterson et al. [29].

4.7 Publication disclosure

The majority of the work shown in this chapter was submitted for publication with authors Cummock et al. [74], and is pending peer review at the time of writing this dissertation.

5. A REVIEW ON HOT SPOTS AND SHOCK SENSITIVITY

Experiments revealing information about the initiation mechanisms of explosives is of high value due to the critical need for predicting explosive behavior when subjected to varying types of insult. It is of interest to pursue experiments which reveal information about critical hot spot generation, i.e., which characteristics of hot spots are important in determining whether or not initiation in an explosive will occur. The following experiments have been recently undertaken and are ongoing at Zucrow Labs, Purdue University.

1. **Gas gun shots on HMX/sylgard systems (typically with very low solids loadings) using high-speed (1-2 Mfps) phase-contrast imaging**. These experiments had the goal of visualizing decomposition and damage of HMX crystals within a binder system, particularly involving interactions at the particle-binder interface and at crystal asperities. Similar shots have also been performed using visible light imaging, possible since the binder in use is clear.

2. **Mechanical excitation of HMX/sylgard systems near a system resonant frequency ($\approx$ 250 kHz)** using contact piezo-electric transducers. Eventually, the goal is to explore HMX/binder interactions with varying binder mechanical properties, such as stiffness. It is suspected that delamination of the binder from the HMX crystal plays a large role in particle heating due to resonant excitation.

3. **High speed visualization (5-10 Mfps) of small-scale ($<$ 5 g) ideal and non-ideal detonations**, which serve to both verify velocity measurements of microwave interferometer experiments, and to provide additional insight on the behavior of explosives under very light confinement at the small-scale, particularly during the process of detonation failure (when the charge is under the explosive's critical diameter).

A number of initiation related research questions and topics of interest are presented here, with some background relating to each topic.

5.1 The reactivity of dynamical hot spots versus thermal hot spots

Campbell et al. [75] explored the initiation of nitromethane (NM) containing inclusions in 1961 in an effort to determine whether shock heating of the gas, or heating of the explosive in a local region due to pressure interaction at the inclusion is more important in the initiation process. Recent atomistic simulations showed that the size and thermodynamic conditions of hot spots are not sufficient to determine their criticallity [76], i.e., dynamical hot spots (those induced by mechanical insult or shock rather than pure heating) are more reactive than thermal hot spots of identical size and thermodynamic conditions, which predictions conflict with current hot spot models and have not yet been confirmed or denied experimentally.

5.2 Inferring hot spots characteristics based on the downward concave region of the diameter effect curves in heterogeneous explosives

Experiments have shown that adding inclusions to NM produce a sensitizing effect, in the sense that the critical diameter of the NM is reduced [77]. Additionally, experiments have shown that physically homogeneous explosives have linear diameter-effect curves (i.e., velocity deficits from an 'infinite' diameter are linearly dependent, which dependence is often weak, on charge diameter between the 'infinite' and 'failure' diameters), while large, nonlinear velocity deficits occur before failure diameter is reached in physically heterogeneous explosives [78]. This phenomenon is shown for NM with physical and chemical sensitizing additives in Fig. 5.1. In summary, the scenarios are as follows:

1. Physically homogeneous explosives

   (a) $d >> d_c, \quad D(d) \approx D_\infty$

   (b) $d \approx d_c, \quad D(d) \approx D_\infty$

2. Physically heterogeneous explosives

   (a) $d >> d_c, \quad D(d) \approx D_\infty$

   (b) $d \approx d_c, \quad D(d) << D_\infty$

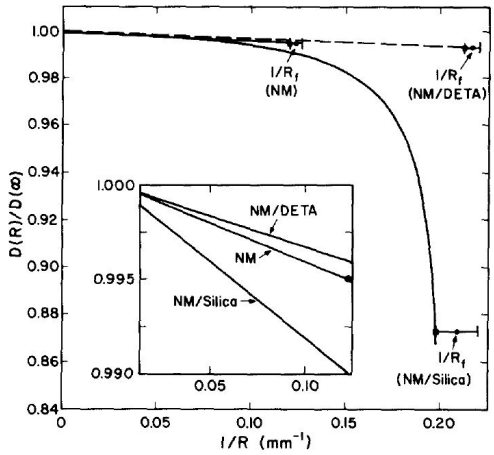

Figure 5.1. Diameter effect curve produced by pure NM, NM/Diethylenetriamine (DETA) (chemical heterogeneity), and NM/silica (physical heterogeneity). Reproduced from [78].

where d is the explosive charge diameter, d_c is the critical diameter of the explosive material, D is the detonation velocity of the explosive, and D_∞ is the detonation velocity of the explosive at infinite charge diameter. See the corresponding Fig. 5.2 and 5.3. It has been suggested that hot spots are responsible for this effect [77], [79].

It is hypothesized that in the case of homogeneous explosives, the decrease in detonation velocity as charge diameter approaches the failure diameter is due solely to lateral energy losses (i.e., expansion losses as the detonation interacts with the yielding confinement surrounding the explosive charge, resulting in curvature of the detonation front, lengthening of the reaction zone, and approach of the sonic plane to the leading shock so that less energy release is available to support the detonation [80]), while the decrease in velocity in heterogeneous explosives is due in part to lateral energy losses, but a larger portion of the decrease in velocity is more complicated.

If the interparticle separation is larger than the explosive's critical diameter, the detonation is able to propagate between the inclusions or voids (see Fig. 5.2), otherwise, the shock propagates through the inclusion and is attenuated to a degree which depends on the size of the inclusion (see Fig. 5.4). If the inclusion through which the shock propagates is sufficiently small (i.e., the shock is not attenuated to below some critical pressure), the detonation may continue beyond the inclusion (Fig. 5.4(a)). It is possible that the area

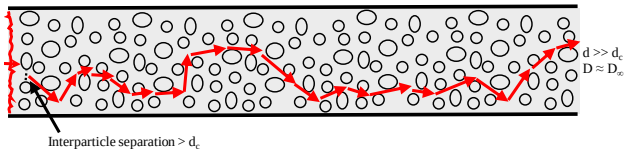

(a) Interparticle spacing larger than the critical diameter allows a detonation to propagate around inert inclusions. In this case, the pathlength through the explosive is increased. Larger inclusion sizes decrease the inclusion packing factor. As can be seen, the detonation wave has a number of paths through which it may travel without necessity of propagating through the inert inclusions. It is expected that all possible paths (between inert particles) will be used, therefore lengthening the overall reaction zone (not locally), which thickness will be proportional to the difference between the shortest pathlength and the longest pathlength between inclusions. Results from [78] showed that it is likely that the NM/Silica mixture has a one-dimensional reaction zone length roughly twice that of NM.

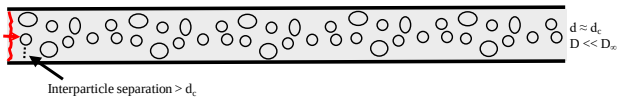

(b) As the charge diameter is decreased, the number of possible paths between inclusions will be proportionally decreased, leading to a decrease in measured detonation velocity due to increased pathlengths in addition to increased lateral energy losses (relative to the case shown in Fig. 5.2(a)).

Figure 5.2. Explosives with equal volume percent of inert heterogeneities show an exponential decrease in detonation velocity as charge diameter is decreased, while their detonation velocities at large diameters are nominally equal to that of their homogeneous counterpart.

(a) A physically homogeneous explosive of very large charge diameter through which a detonation wave propagates shows a detonation velocity similar to that which would be observed in an infinite diameter charge. Lateral losses are negligible in this case.

(b) A homogeneous explosive charge near its critical diameter exhibits a detonation velocity only slightly lower (relative to that of a heterogeneous detonation velocity near its critical diameter) than that of an infinitely large charge diameter homogeneous explosive. Lateral losses are expected to be the primary cause the relatively small detonation velocity deficit observed.

Figure 5.3. Detonation velocity deficit due to decreased charge diameter is small relative to that in heterogeneous explosives.

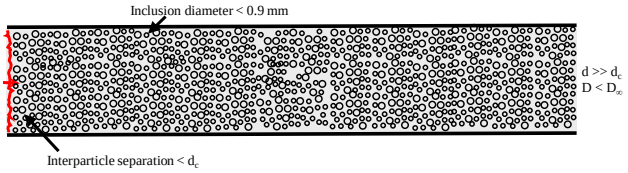

(a) The interparticle separation is less than the homogeneous explosive's critical diameter, however, detonation is able to propagate (with a decreased overall detonation velocity) because the bead diameter is small enough that attenuation through the beads transmits a shock on its far side which is strong enough to reinitiate the explosive.

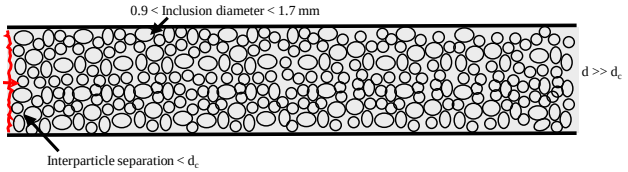

(b) The interparticle separation is less than the explosive diameter and the detonation fails to propagate through the charge because the inert inclusions are large enough to attenuate the shock to below pressures which are able to reinitiate the explosive on its far side.

Figure 5.4. In the shown cases, the interparticle separation is too small for the detonation to propagate between the inert inclusions (i.e., interparticle separation < critical diameter of the homogeneous explosive). The shock front's only forward path is directly through the beads, where shock attenuation occurs.

between the NM/DETA curve and the NM/Silica curve in Fig. 5.1 is proportional to the initial potential energy of each composition, and further, the number or volume of initial hot spot sites found in the explosive.

Additionally, results from Lee et al. [81] indicate that there may be two distinct mechanisms of detonation propagation through heterogeneous explosives (see Fig. 5.5):

- propagation around inclusions/voids when the interparticle or void separation is larger than the explosive's failure diameter, as in Fig. 5.2(a) and
- propagation through the inclusions/voids themselves, where the shock attenuation is not enough to quench the detonation, as in Fig. 5.4(a).

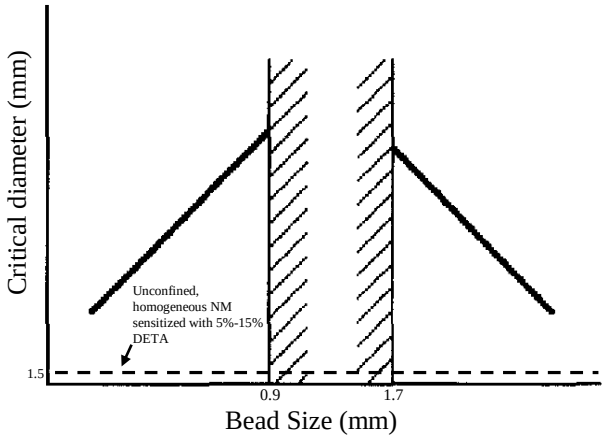

Figure 5.5. Schematic showing the dependence of critical diameter on bead size for NM sensitized with DETA in a densly packed bed of glass beads. Two propagation mechanism regimes are shown, in between which is a 'forbidden zone', where the bead diameter is too small for propagation between beads (due to the increase in packing factor) but large enough to cause sufficient wave attenuation to quench the detonation. Reproduced from [81].

5.2.1 Independently controlling the steady-state and initiation sensitivity of explosives by the addition of heterogeneities

Engelke discussed the possibility of using heterogeneities to independently control the steady-state sensitivity (as measured by critical diameter) and initiation sensitivity (as measured by run-to-distance or induction time in, for example, wedge tests) [82]. It was noted that 150 μm heterogeneities separated by 200 μm were reported to reduce the initiation distance in NM by 15% [75], while work from Engelke [82] showed that heterogeneities of similar size and separation leave the critical diameter of NM unchanged or increased it, i.e., the steady-state sensitivity (as measured by critical diameter) was unchanged or decreased. The addition of heterogeneities in a similar manner may allow the converse type of control, where an explosive from NM with a reduced critical diameter, but unchanged or increased initiation distance is produced. Fig. 5.6 shows a few of the simplified scenarios of changes in failure diameter and induction time (run-to-detonation time) as a function of heterogeneity characteristics.

Additionally, Engelke [82] proposed that the wave reflection process, e.g. the strength of the wave reflection as is determined by the acoustic impedance ratio of the shocked materials, on inhomogeneities plays a role in the critical-diameter reduction phenomenon.

Also, it is noted that a critical diameter reduction only occurs in NM when the average interparticle separation distances (L) is less than the NM one-dimensional reaction zone length. It is also of interest that for L spanning the range of 1/6 to 2/3 of NM reaction zone length, L is linearly correlated with the charge critical diameter (see Fig. 5.7), while the function relating critical diameter and number density of heterogeneities per unit volume is not linear [82].

Information required to develop a theoretical understanding of the relationship between critical diameter and L would require [82]:

1. a theory of the dependence of critical diameter on the chemical heat-release function in the detonation reaction zone [83]

2. knowledge of the thermodynamic-state dependence of the homogeneous material chemical heat-release function

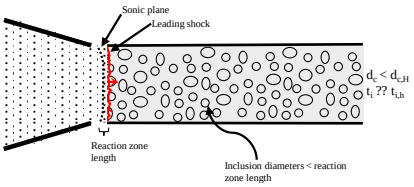

(a) A steady-state detonation wave propagating through an explosive with heterogeneities with diameters smaller than the reaction zone length of the detonation wave in the homogeneous explosive. Heterogeneities with diameters larger than the reaction zone length still may effect initiation.

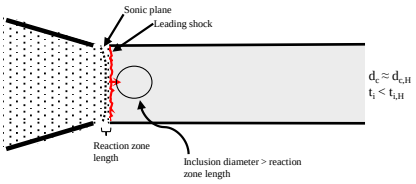

(b) A shockwave during build-up, or initiation, during which heterogeneities of a variety of sizes, including diameters larger than the reaction zone length of the homogeneous material, may reduce the induction time (t_i) of the material.

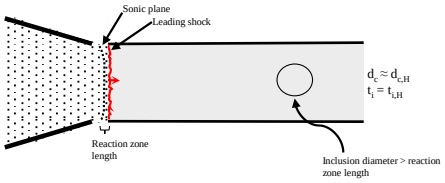

(c) A similar sized heterogeneity as that in Fig. 5.6(b) is shown further into an otherwise homogeneous explosive, in which case no effect on the induction time or the critical diameter will be observed, as the shock will have fully developed into a high-order detonation by the time the inclusion is met.

Figure 5.6. Schematics showing the scenarios in which heterogeneities may affect the steady-state shock sensitivity (measured by critical diameter) and induction time (often measured in the wedge test). d_c represents the critical diameter of the shown charge, $d_{c,H}$ is the critical diameter of the homogeneous explosive, t_i is the induction time of the shown charge, and $t_{\mathrm{i},H}$ is the induction time of the homogeneous explosive. Note that it may be possible for inhomogeneities to be included in an explosive a manner such that, as in Fig. 5.6(a), the critical diameter of the homogeneous explosive is decreased, while the induction time is increased (thus, increasing the steady-state shock sensitivity, while decreasing the initiation shock sensitivity).

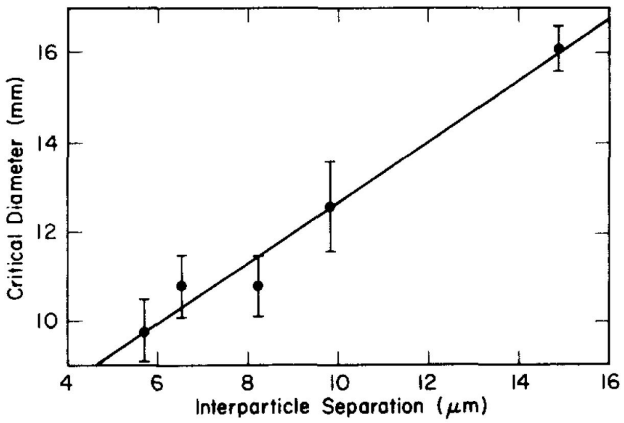

Figure 5.7. Linear relationship of interparticle separation distance (L) and critical diameter of NM, reproduced from [82].

3. a correct model of how the heterogeneities and their spacing modify the chemical heat-release function of the homogeneous material

where if factors (1) and (2) are given with a data set, one could likely determine something about factor (3) by solving the inverse problem for the heat-release function in the materials containing the heterogeneities.

5.3 Viscoplastic collapse versus hydrodynamic collapse

As is shown in Fig. 5.8, viscoplastic collapse [84]–[88] is expected at small pore radii ($a_0 < 100$ nm) and high viscosities ($\mu > 10^2$ Pa·s), while hydrodynamic collapse [89] is expected at large pores ($a_0 > 30$ μm) and low viscosities ($\mu < 5 \times 10^{-1}$ Pa·s). Visualization of the shock as it passes through a pore may elucidate the mechanism of collapse and hot spot formation.

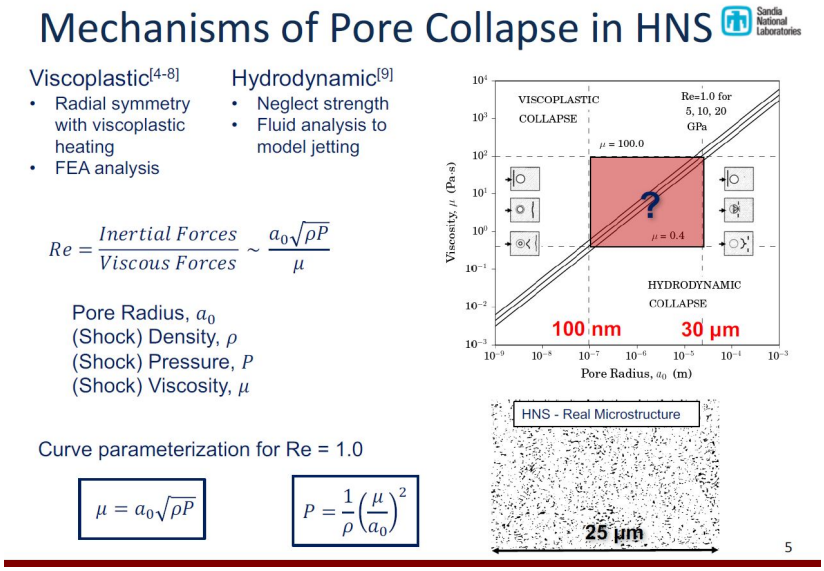

(a) Slide from a presentation given by Dr. Kittell (Sandia National Labs) at Purdue University, showing the regimes in which viscoplastic collapse and hydrodynamic collapse are expected. Note the parameters where the pore collapse mechanism is unknown.

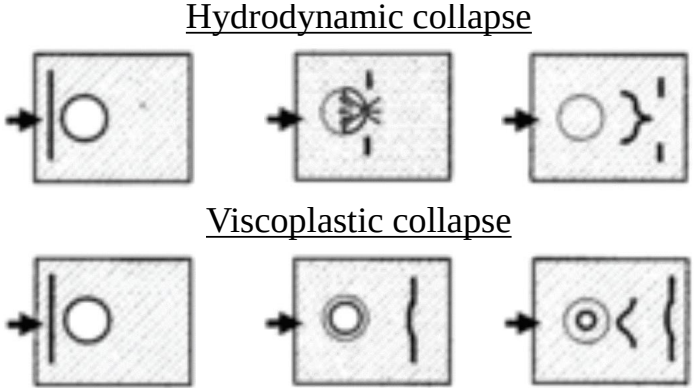

(b) Enlargened image of the two collapse mechanisms discussed (shown in Fig. 5.8(a)), viscoplastic, and hydrodynamic.

Figure 5.8. Pore collapse regimes, viscoplastic collapse vs. hydrodynamic collapse. Presented by Dr. David Kittell at Purdue University in 2017.

6. PRELIMINARY SMALL-SCALE GAP TEST RESULTS ON PRISTINE AND THERMALLY DAMAGED PBX 9501

The purpose of this chapter is to provide the reader with a brief background on shock sensitivity tests, and an attempt at using inordinately small samples to obtain shock sensitivity information. This attempt introduced multi-dimensional attenuation effects into the data, adding complexity to the analysis and interpretation of the results.

6.1 Background

The Pop-plot [90] is commonly used to gain an understanding of relative shock sensitivity of energetics, and shows the run-to-detonation distance (r_d) as a function of pressure input (P); however, there is little experimental data available showing the change that occurs in shock sensitivity of an energetic, and its corresponding Pop-plot, as it changes in density. Thermal damage in a polymer bonded explosive (PBX) results in a change in density in addition to other potential material property changes. The energetic, PBX 9501 (95% HMX, 2.5% estane, 2.5% plasticizer) is well known, along with its Pop-plot data at high densities (>98.2% of its Theoretical Maximum Density, or TMD), as can be seen in Fig. 6.1). Typical experiments yielding Pop-plots are known as wedge tests, which require machining of energetic materials to high tolerances. This sort of machining is likely infeasible for low density materials, and especially for damaged materials. Gas gun experiments can also be used to yield Pop-plot data, although the range of pressure inputs will not be as high as that of wedge tests.

Here, it is hoped that a convenient method for acquiring data to be used for shock sensitivity evaluation of low density and damaged energetic materials, which potentially has comparable results to those of one-dimensional experiments (thus potentially yielding valid Pop-plots), can be developed.

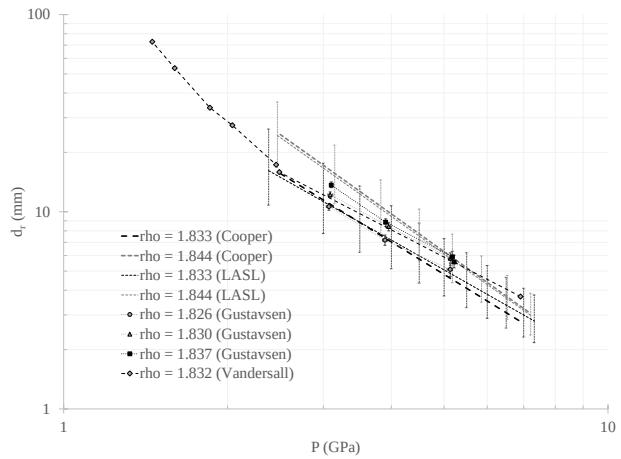

Figure 6.1. Pop-plot for PBX 9501 with data from a variety of sources at similar densities [91]–[94]. Vandersall et al. [94] found that very low shock pressures don't align with a straight log-log fit of the same materials shocked at high pressures.

6.1.1 Transforming a Pop-plots to density versus attenuator length

Although the Small-Scale Gap Test (SSGT) configuration using polymethyl methacrylate (PMMA) shown in this work (as described in section 6.3) does not simulate a one-dimensional test, it is desired that a comparison can be made to the results of experiments which yield Pop-plot data, since the SSGT is designed with the intention of making shock sensitivity comparisons. It is important to keep in mind when drawing any conclusions based on such a comparison that the SSGT very likely has 2-dimensional effects due to the experimental geometry and size. To make such comparisons, it is necessary to convert a portion of Pop-plot data to Density vs. Attenuator length plots. This requires the use of several calibration curves, and as such, no extrapolations should be made.

The first necessary calibration curve is that of the input pressure to the sample as a function of the attenuator length. This curve, of course, will be specific to the combination of the booster input into the attenuator and the attenuator type. An example of such a calibration curve is shown in Fig. 6.2. The calibration curve for here will be of the form:

$$P = k_1 L_A^{-k_2}, \tag{6.1}$$

where P is output pressure (typically in GPa), L_A is the attenuator length (typically in mm), and k_1 k_2 are both constants, tuned to the data. The data shown in Fig. 6.2 was obtained from the work of Cutting et al. [95].

Additionally, of course, the Pop-plot data which is desired to be transformed is necessary. Pop-plot data is typically on a log-log scale, as is shown in Fig. 6.1. Each dataset shown has its corresponding calibration curve of the form:

$$r_d = c_1 P^{-c_2} \tag{6.2}$$

where r_d is the run-distance to detonation (typically in mm), and both c_1 and c_2 are constants, tuned to the data.

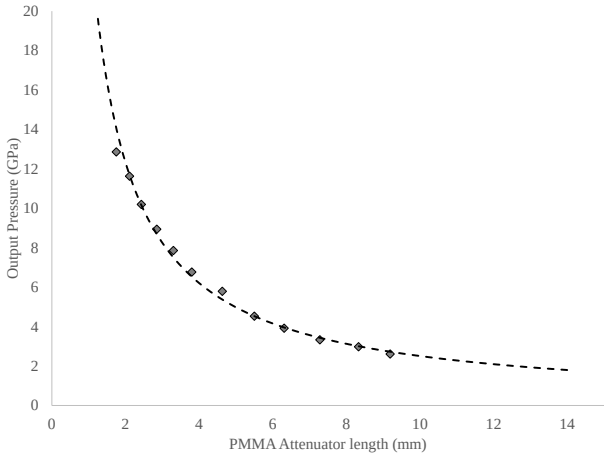

Figure 6.2. Output pressure as a function of attenuator length, where the booster here is Detasheet and the attenuator is PMMA. Least squares curve fit to the shown data points from [95].

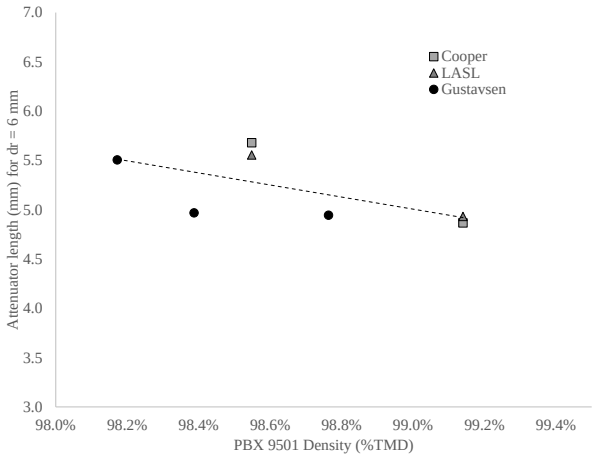

Figure 6.3. Pop-plot transformation to density vs. attenuator length space. Each data point is simply an interpolation of each dataset along the $r_d = 6$ mm line in Fig. 6.1. Note the very small density range given here, which should not be flippantly extrapolated to lower densities.

Combining Eq. 6.1 and 6.2 yields

$$r_d = c_1 \left(k_1 L_A^{k_2} \right)^{-c_2} , \tag{6.3}$$

at which point r_d can be fixed to the desired run-distance, perhaps the length of the sample being tested, and the value of L_A may be solved noting the density of the samples tested for each dataset in the Pop-plots. Two vectors are then formed, one of density, and one of attenuator length required to make the run-distance, r_d, equal to the chosen value. Here it is noted that the solution to Eq. 6.3 is:

$$L_A = \left[\frac{\left(\frac{r_d}{c_1} \right)^{-1/c_2}}{k_1} \right]^{-1/k_2} ,$$

which, if desired, can be related directly back to a Pop-plot, where r_d would equate to the length of the sample pellets tested, and P is found using Eq. 6.1. The result of transforming the Pop-plot given in 6.1 to density vs. attenuator length space is shown in Fig. 6.3.

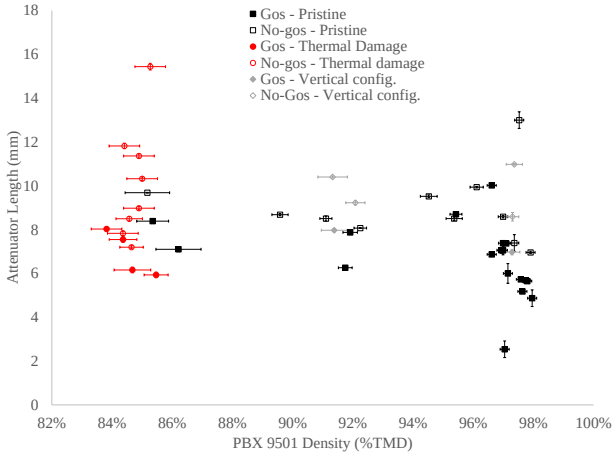

Figure 6.4. SSGT results for 6 mm diameter, 6 mm height cylindrical samples, where filled markers represent a completed detonation as reported by a dent in a witness plate, and non-filled markers represent a failure to reach detonation. Thermally damaged samples started at 97% TMD, and thermal damage resulted in a porosity increase of approximately 12%. Samples in 'vertical configuration' are pristine.

6.2 Recent results

A SSGT has been used to evaluate the shock sensitivity of PBX 9501 after it has been thermally damaged, in comparison with its undamaged counterpart at varying initial densities. Upon acquiring some of the initial results, there was some concern that the configuration of the SSGT may have been dominating in some way due to weak confinement on one side of the samples; thus, the 'vertical confg.' shots were made. Figure 6.4 shows the 'go–no-go' raw results. Here, thermally damaged PBX 9501 samples, which were pressed to an initial density of 97% TMD, are compared to pristine samples of varying densities, including a density similar to that of the post-damaged PBX 9501 samples.

6.2.1 Thermal input

It is well known that a solid-solid phase transition occurs in HMX at elevated temperatures near 180 °C, where the transition results in a solid phase of HMX which is thought to be, in general, more sensitive than more commonly encountered β-phase, of HMX. The energetic material, PBX 9501 is made up of 95% HMX by mass; heating pressed PBX 9501 pellets to

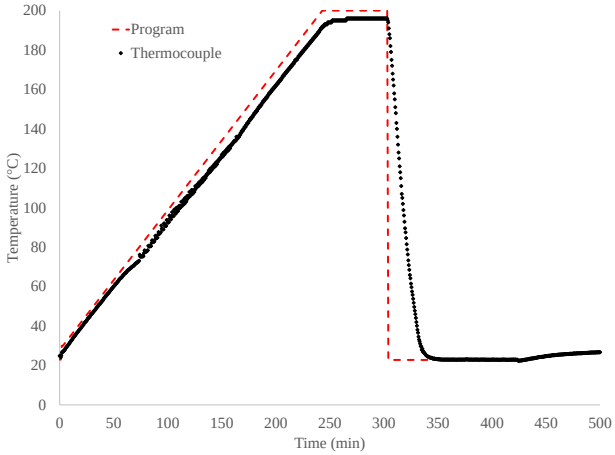

Figure 6.5. The thermal input to the PBX 9501 samples as programmed by a forced convection oven and measured by thermocouple in open air nearby the pellets within the oven.

a sufficient temperature will not only produce the supposedly more sensitive δ-phase HMX, but an increase in porosity, and potentially even a change in particle size may occur via a process known as Ostwald ripening [96], [97], where fine HMX particles are dissolved by the PBX 9501 plasticizer and subsequently recrystallize onto larger particles continually. It was desirable to damage the samples in a spatially uniform and repeatable manner order to assess the affect on the shock sensitivity of PBX 9501; Smilowitz and Henson saw that radial temperature gradients of less than 0.5 K could be maintained when heating 4x4x1 mm samples of PBX 9501 at 4.8 K/min or slower [98], additionally, phase reversals (from $\delta \rightarrow \beta$-phase) were observed when cooling slowly at 3 K/min; it is necessary to rapidly cool in order to 'kinetally lock' in the $\beta \rightarrow \delta$-phase transition. Thus a heating profile for PBX 9501 samples in this work was chosen such that heating rate was $\sim$0.7 K/min and the cooling rate was $\sim$6 K/min (as shown in Fig. 6.5).

6.2.2 Statistical analysis

The 'go–no-go' results shown in Fig. 6.4 were grouped into three separate density intervals in order to evaluate the Mean Likelihood Estimate parameters, μ_{MLE} and σ_{MLE}, for each group. With these parameters, the shape of the Probability Density Function (PDF) can be estimated, thus allowing meaningful comparisons against each group. The distributions have

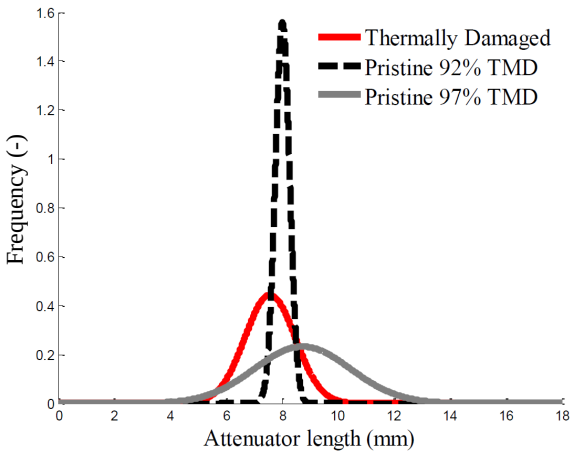

Figure 6.6. PDF of each group, where 'thermally damaged' represents all of the thermally damaged samples, 'Pristine 92% TMD' represents all samples with densities from 91.1–92.2% TMD, and 'Pristine 97% TMD' represents all samples with densities from 96.6–97.5% TMD.

been assumed to be normal. The estimated PDF for each group is shown in Fig. 6.6, and the cumulative distribution function (CDF) is also constructed based off of each PDF, and each is shown in Fig. 6.7, showing the percent chance of a complete detonation as a function of attenuator length. Some of the groups were not analyzed due to the lack of a meaningful number of datapoints, and some datapoints were left outside of a group altogether due to their anomalous density; this can be seen in Fig. 6.8. It should be noted that the 'Pristine 97% TMD' or 'HD1 press' may have been grouped with too large of a density interval, considering that the shock sensitivity may be highly sensitive to density in the high density region (above ∼96%), thus resulting in the wide PDF due to the large σ_{MLE} for that group.

Here, the distributions have been represented along with the L50, L95, and L05, which represent the attenuator lengths at which there is a 50%, 95%, and 5% chance of a complete detonation. In addition to these metrics, it is important to quantify the confidence in these estimates, i.e., the confidence in μ_{MLE} and σ_{MLE}.

6.2.3 Comparison to Pop-plot data

Using the method described in section 6.1.1, the data shown in Fig. 6.8 can be transformed to input pressure (P) vs. run-distance space, where the length of the pellet used in the SSGTs

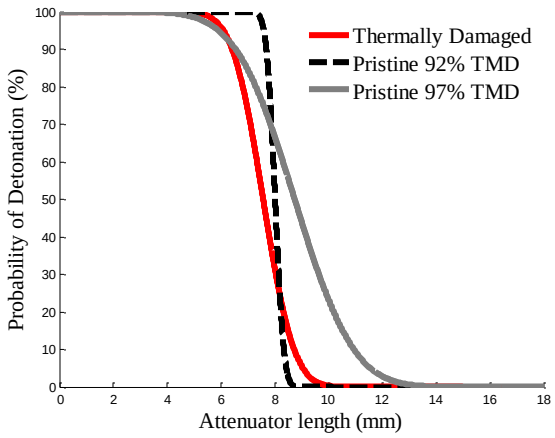

Figure 6.7. CDF of the PDFs shown in Fig. 6.6.

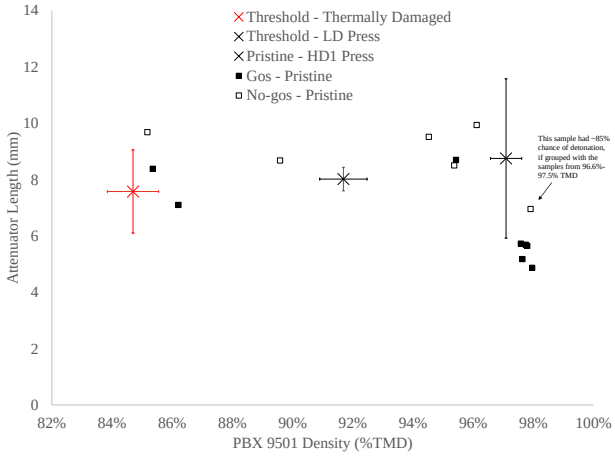

Figure 6.8. Groupings of 'go–no-go' results. Note that here, the vertical bars for the three groups do not represent error, rather they represent the L95 (bottom) and L05 (top). Similarly, each of the three points themselves represent the L50.

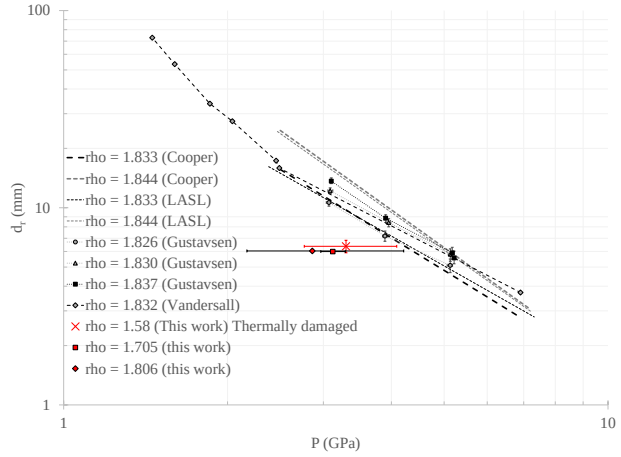

Figure 6.9. SSGT results compared with Pop-plot data for PBX 9501, where the horizontal uncertainty bars actually represent the L95 (right) and L05 (left).

represents the run-distance (r_d). Here, comparisons can be made to 1-dimensional data obtained from wedge tests and gas gun experiments (see Fig. 6.9). It is expected that higher density PBX 9501 SSGTs will yield results which will approach 1-dimensional Pop-plot data.

6.3 Literature on changing the slope of a Pop-plot

It should be noted that a simple change in shock sensitivity might not be expected when thermally damaging PBX 9501 to a level that produces a $\beta \rightarrow \delta$-phase transition. This is due to effects from multiple mechanisms involved in determining the shock sensitivity, particle size effects which may cause a change Pop-plot slope, (see Fig. 6.10) occurring both at different pressing intensities [99] and possibly during thermal damage [96], in addition to shifts in Pop-plot occurring with changes in porosity, not to mention the unknown effect of the δ-phase HMX.

There are ways to isolate some of these mechanisms, but quite a few experiments would be needed to make any conclusions.

The current configuration of the SSGT is concerning due to the weak confinement on one side of the pellet. It may be necessary to try a number of shots in a vertical, unconfined configuration in order to see if the weak confinement is dominating the sensitivity results. Fig. 6.11 shows the results of six (6) recent tests with vertical configuration, where it appears

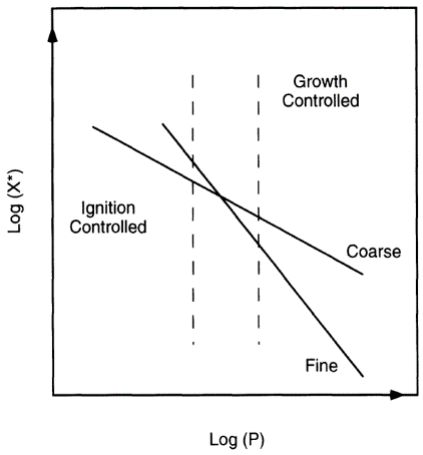

Figure 6.10. A hypothetical Pop-plot of a material at two different particle sizes, with all other parameters identical. Reproduced from [100].

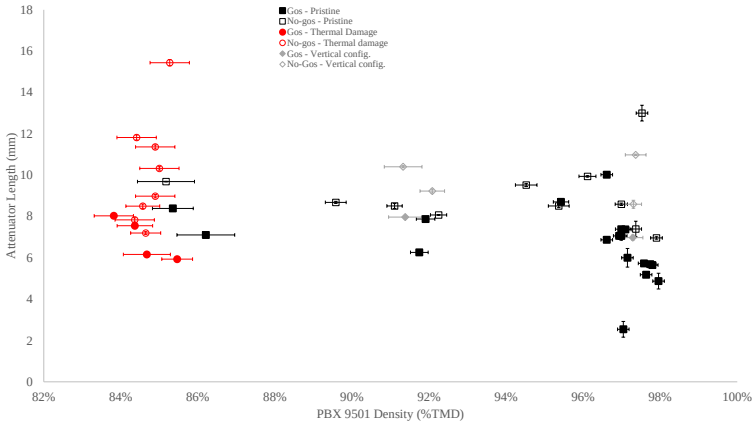

Figure 6.11. SSGT results, where filled markers represent a completed detonation as reported by a dent in a witness plate, and non-filled markers represent a failure to reach detonation. Thermally damaged samples started at 97% TMD, and thermal damage resulted in a porosity increase of approximately 12%. Samples in 'vertical configuration' are pristine.

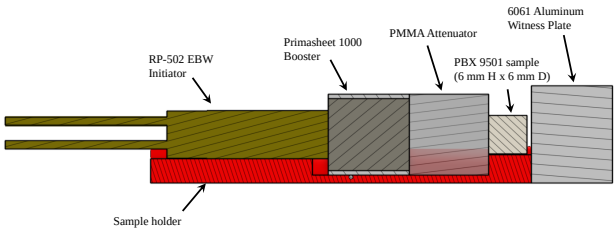

Figure 6.12. Cross section of configuration number one, which is the default configuration, for the SSGT in this dataset.

that at both mid-density (approximately 91% TMD) and high density samples, the confinement doesn't have a significant effect. Figures 6.12 and 6.13 show the two configurations, where Fig. 6.12 shows the configuration for most of the samples, and Fig. 6.13 shows the configuration for the unconfined, 'vertical config.' samples.

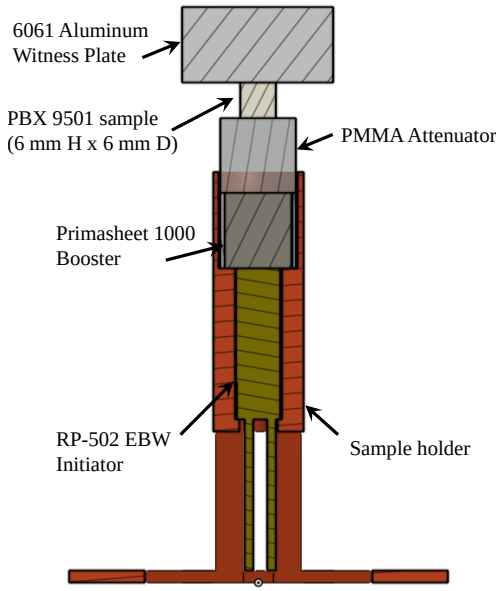

Figure 6.13. Cross section of configuration number two, the vertical configuration, for the SSGT in this dataset.

7. ANALYSIS OF A SHOCK WAVE IN A SMALL-SCALE GAP TEST

A Small-Scale Gap Test (SSGT) was designed in order to draw correlations of thermal damage input to PBX 9501 pellets to their shock sensitivity, relative to pristine PBX 9501 pellets. In the SSGT, the length of a PMMA attenuator, situated between a booster and the sample of interest, was varied in order to control the shock input to the PBX 9501 sample. Unexpected behavior was apparent from the results of the SSGT, and thus further analysis of the shock as it travelled through the attenuator was merited.

7.1 Overview of input pressure reduction due to rarefaction waves

It can be seen from the results of experiments plotted in the density vs. attenuator length plots (see Fig. 6.4; hereafter referred to as *ρ-input plots*) that attenuator lengths longer than roughly 8.5 mm result in low chance of detonation. It is unexpected that this length seems fairly constant for varying initial densities of PBX 9501. It is possible that the input shock is highly attenuated once this length in the PMMA is reached due to radial attenuation and 'thin-pulse' condition effects in the PMMA [101]. It will be important to take into account the effect from both the rarefaction wave following the shock input to the PMMA and the radially traveling rarefaction wave. Both of these phenomenon can cause greater run-distances than expected from a one-dimensional case, or failure to detonate. The effects of a small diameter impacter (or attenuator) can be seen in Fig. 7.1.

In addition to rarefaction waves in the attenuator potentially causing reduced pressure input, the length of the unreacted explosive due to the run-distance itself must be taken into account. The options for estimating the effect of the rarefaction waves on the pressure input to the samples in the SSGT are the use of the Hugoniot relationships in the attenuator and unreacted explosive, and gathering experimental evidence that the attenuation due to rarefaction is negligible or accountable.

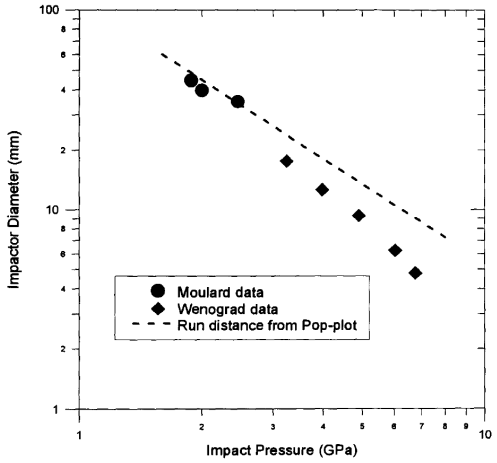

Figure 7.1. Small impacter diameters cause a deviation from the Pop-plot run-distance. Reproduced from [101].

Table 7.1. U-u Hugoniot plane values (taken from [102] and [103]).

Material	ρ_0 **(g/cm^3)**	C_0 **(km/sec)**	s **(-)**	q **(sec/km)**
Plexiglass	1.186	2.598	1.516	0
PBX 9501	1.844	2.683	1.906	0
347 Steel	7.910	4.62	1.42	0

7.2 Analysis of shock and rarefaction wave interactions

The shock velocity can be found from its particle velocity relationship [101]

$$U = C_0 + su \tag{7.1}$$

and a rarefaction wave velocity can be approximated by [101]

$$R = C_0 + 2su, \tag{7.2}$$

where U is the shock velocity, C_0 is the bulk sound speed[1], s is the velocity Hugoniot coefficient, u is the particle velocity, and R is the rarefaction wave speed. Parameters for PMMA (also known as Plexiglass) are given in Table 7.1 (see [102] and [103]) along with those of other relevant materials[2].

7.2.1 Using U-u Hugoniot relationships

Here, the particle velocity, u, in the attenuator is not measured, but it may be estimated based a conservation of momentum, assuming that the shock pressure (P) input to the attenuator is known:

$$P_1 - P_0 = \rho_0(u_1 - u_0)(U - u_0) \tag{7.3}$$

[1] C_0 has no real physical meaning [102] other than the fact that it is the y-axis intercept on a straight line drawn through the data points on the U-u plane. Do not confuse this parameter with C_L or C_S, the longitudinal and shear wave velocities.

[2] $U = C_0 + su + qu^2$; sometimes a shift in slope of the U-u Hugoniot occurs, which is accounted for by the q parameter. This shift in slope is likely due to a phase change or shift in crystal lattice that occurs at the given point in the plane.

where the subscripts 0 and 1 represent material just before the shock, and just after the shock, respectively. From Eq. 7.3 it is seen that

$$u_1 = \frac{P}{\rho_0 U}, \tag{7.4}$$

where $P = P_1 - P_0 \approx P_1$ for strong shocks such as those resulting from an explosive, and $u_0 = 0$. Since the right-hand side of Eq. 7.4 depends on u_1, the quadratic formula is used to yield:

$$u_1 = \frac{1}{2s}\left[-C_0 \pm \left(C_0^2 + \frac{4sP}{\rho}\right)^{1/2}\right]$$

The parameters s, C_0, P, and ρ in Eq. 7.5 are always positive values for a detonation, and as such, Eq. 7.5 will always yield a positive and a negative solution. A particle speed, u_1, which is not in the same direction as the shock in a detonation is non-physical, and as such, the positive value for u_1 is taken as the particle speed. Thus,

$$u_1 = \frac{1}{2s}\left[\left(C_0^2 + \frac{4sP}{\rho}\right)^{1/2} - C_0\right] \tag{7.5}$$

Note that giving C_0 in km/s, ρ in g/cm^3, and P in GPa will yield u_1 from Eq. 7.5 in units of km/s. Note that Eq. 7.5 is simply the momentum equation (Eq. 7.3) solved for u_1, (where $P_0 = u_0 = 0$).

7.2.2 Using P-u Hugoniot relationships

Section 7.2.1 assumes that the input pressure, P_1 is known; however, if the impedance of the input explosive detonation products ($Z_{det} = \rho_0 D$) and that of the receiving attenuator ($Z_{mat} = \rho_0 U$) are not equal, then the initial shock pressure after transition from the booster to the attenuator (P_1) is not equal to Chapman-Jouguet pressure (P_{CJ}) of the booster; i.e., $P_1 \neq P_{CJ}$. In such cases, the input pressure must be calculated by matching P-u Hugoniots for the two materials and solving for u_1, which will yield the pressure after the transition from the booster to the attenuator (P_1).

This can be accomplished only knowing P_{CJ} for the input explosive, its detonation velocity, and its initial density, in addition to the Hugoniot parameters for the receiving attenuator (see Table 7.1). It has been found that the P-u Hugoniot for many explosives fall into a narrow band when plotting reduced pressure (P/P_{CJ}) and reduced particle velocity (u/u_{CJ}) [104]. This data is correlated by

$$\frac{P}{P_{CJ}} = 2.412 - 1.7315\left(\frac{u}{u_{CJ}}\right) + 0.3195\left(\frac{u}{u_{CJ}}\right)^2 \tag{7.6}$$

where $u_{CJ} = P_{CJ}/\rho_0 D$. This correlation holds for $P/P_{CJ} > 0.08$, and may provide a reasonable estimate when using explosive materials which do not have experimental data available for the C_0 and s parameters for the detonation products. The P-u Hugoniot for the receiving attenuator may be represented by

$$P = \rho_0 u_1 \left(C_0 + s u_1\right). \tag{7.7}$$

Combining Eq. 7.6 and 7.7 yields

$$\begin{aligned} \left(\rho_0 s - 0.3195\frac{P_{CJ}}{u_{CJ}^2}\right) u^2 + \\ \left(1.7315\frac{P_{CJ}}{u_{CJ}} + \rho_0 C_0\right) u - 2.412 P_{CJ} = 0 \end{aligned} \tag{7.8}$$

from which u can be solved and entered into Eq. 7.6 or 7.7 to calculate P, where ρ_0, s, and C_0 are for inert attenuator (see Table 7.1). Note that for $Z_{det} > Z_{mat}$,

$$u > u_{CJ} \quad \text{and} \quad P < P_{CJ}$$

while for $Z_{det} < Z_{mat}$,

$$u < u_{CJ} \quad \text{and} \quad P > P_{CJ}.$$

7.3 Thin pulse condition: estimation of the length into the attenuator at which shock attenuation begins due to the rear rarefaction wave

The pulse duration of the shock (t_s) formed is given by

$$t_s = x_s \left(\frac{1}{U} + \frac{1}{R} \right) \tag{7.9}$$

where x_s is the thickness of the input shock. This may be the thickness of a flyer which inputs pressure to the sample upon impact, or, in this case, perhaps the reaction zone thickness.

The following relation can be used to calculate the distance over which the shock maintains constant peak pressure [101]:

$$x_{P,const} = \frac{URt_s}{R - U} \tag{7.10}$$

Beyond the distance $x_{P,const}$, the rarefaction continually attenuates the peak pressure. This attenuation from Primasheet 1000 to PMMA is shown in data taken by Cutting et al. [95] in an experiment simulating one-dimensional conditions. The measurements taken by Cutting et al. [95] used a booster of 10 cm (3.9 in) diameter, and pressure measurements were taken from the axis of the PMMA, such that the side rarefaction wave had no effect on pressure measurements.

7.4 Two-dimensional effects: estimation of the length into the attenuator at which side rarefaction waves become important

Whether or not the effect of impact shock diameter is significant can be estimated using U and R from Eq. 7.1 and 7.2 to calculate the base angle of a cone-shaped zone that defines the only location where the initial impact shock pressure endures (see Fig. 7.2). Noting that the rarefaction velocity is greater than the shock velocity [101], the base angle of this cone-shaped zone must be less than 45°. The formula to calculate this base angle is simply:

$$\alpha = \arctan \left(\frac{U}{R} \right) \tag{7.11}$$

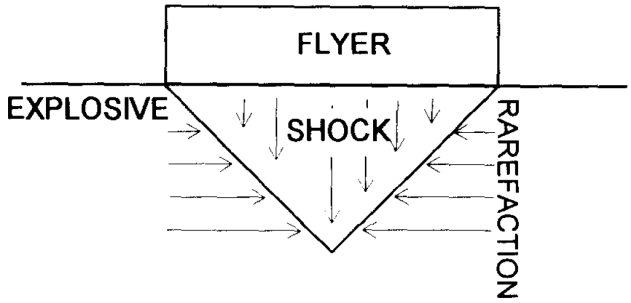

Figure 7.2. Diagram showing the attenuation effect of a radially propagating rarefaction wave. Reproduced from [101].

where α is the base angle; as such, the formula for calculating the distance into the attenuator of the cone apex (d_{cone}) is

$$d_{cone} = \frac{d_A U}{2R} \tag{7.12}$$

where d_A is the diameter of the attenuator and booster charge in use. Assuming that a shock reaches the sample explosive, if the apex distance within the explosive is very small (close to half) of the ideal run-distance of the explosive sample, it will fail to detonate.

Using $P_{CJ} = 18.52$ GPA, $D = 7.1$ km/s, and $\rho_0 = 1.44$ g/cc for Primasheet 1000 [105], [106] in addition to the parameters shown in Table 7.1 for polymethylmethacrylate (PMMA), the particle velocity (u_1) in PMMA after receiving the shock from the booster is calculated and shown, along with other relevant values, in Table 7.2. The uncertainty in $x_{P,const}$ is based on the reaction zone thickness (x_s from Eq. 7.9) of 0.1–0.9 mm [107]; the data from Cutting et al. [95] suggests that the reaction zone thickness for Primasheet 1000 is less than or equal to to 0.365 mm ($x_s \leq 0.365$ mm) since the data shows a rise in pressure output with decreasing PMMA length down to 1.75 mm, though data is not shown for lengths shorter than 1.75 mm (see Fig. 7.3).

The rate of pressure decay was estimated to decay at three times its original rate once it reached d_{cone} (Eq. 7.12) for the pellet center, and twice its rate after reaching the distance where the side rarefaction meets the pellet edge for the radius of the pellet. It is likely that the pressure decay due to the side rarefactions seen in Fig. 7.3 is heavily exaggerated as seen by a test recorded with a high speed video where a 9 mm length PMMA attenuator is boosted by Primasheet 1000. As shown in Fig. 7.4 sufficient void collapse occurs within the

Table 7.2. Shock calculations in PMMA after receiving the initial shock from the booster, PS 1000, both of which are 12.7 mm (0.5 in) in diameter.

Parameter	Calculated value
u_1 (km/s)	1.92
U (km/s)	5.5
R (km/s)	8.4
$x_{P,const}$ (mm)	2.4±1.9
d_{cone} (mm)	4.2

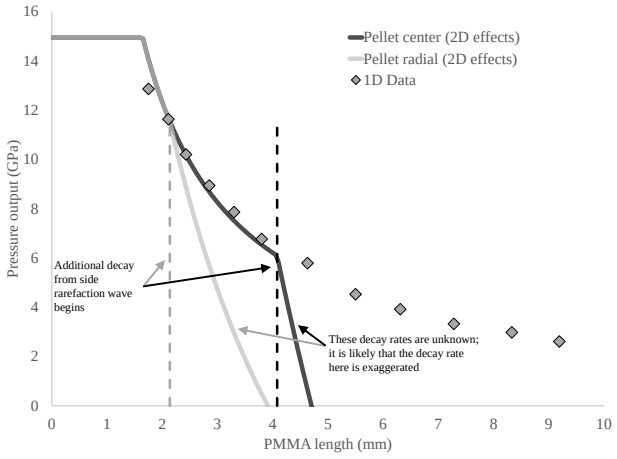

Figure 7.3. Estimation of effects of side rarefaction waves on the output shock into a PBX 9501 sample in the SSGT using 12.7 mm (0.5 in) diameter booster and attenuators. The side rarefaction waves reach the outer radius of the pellet first, as shown by 'Pellet radial (2D effects)'. One-dimensional data ('1D Data') taken from [95].

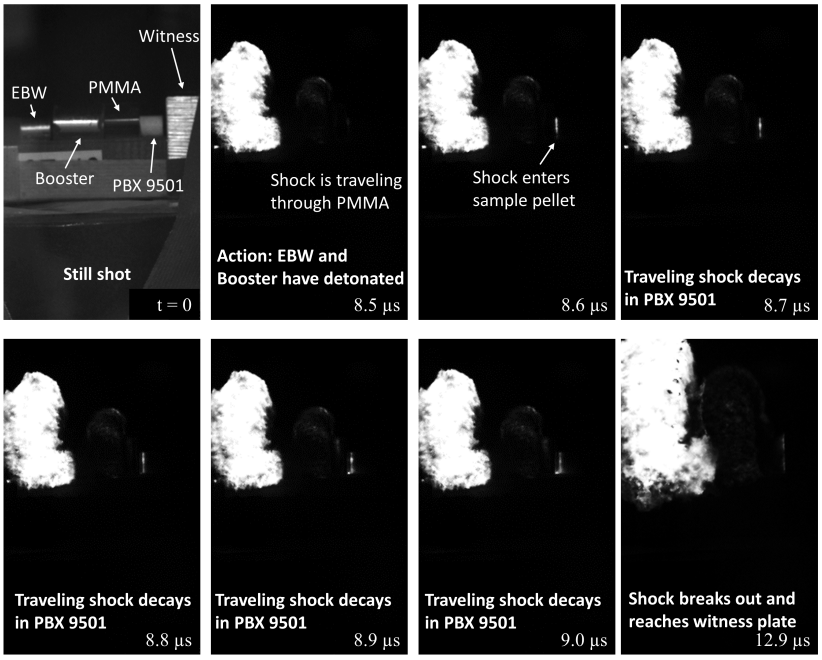

Figure 7.4. Select high speed images (10 MHz) of the SSGT using a 9 mm PMMA attenuator. Here it is shown that a significant pressure wave reaches the sample pellet, though the event did not grow to a detonation (no dent on the witness plate).

sample such that light was emitted and visible to the camera as the shock travelled through the sample pellet.

7.5 Assume that the sample pellet receives a one-dimensional shock: effect of side rarefaction waves in the sample

For an inert shock transition from a material A to material B, the solution to the particle speed at the interface of the materials, found by matching P-u Hugoniots is:

$$\begin{aligned} u = \frac{1}{2s_A\rho_A - 2s_B\rho_B}\Big\{ & C_{0,A}\rho_A + 4s_A u_{0,A}\rho_A + \\ & C_{0,B}\rho_B \pm \Big[C_{0,A}^2\rho_A^2 + \\ & 2C_{0,A}\left(C_{0,B} + 4s_B u_{0,A}\right)\rho_A\rho_B + \\ & \rho_B(8s_A u_{0,A}(C_{0,B} + 2s_B u_{0,A})\rho_A + C_{0,B}^2\rho_B)\Big]^{(1/2)}\Big\} \end{aligned} \tag{7.13}$$

where the left and right going Hugoniots for materials A and B, respectively are:

$$P_L = \rho_A C_{0,A}\left(2u_{0,A} - u\right) + \rho_A s_A\left(2u_{0,A} - u\right)^2 \tag{7.14}$$

and

$$P_R = \rho_B C_{0,B} u + \rho_B s_B u^2 \tag{7.15}$$

and $P_L = P_R$ at the interface. In Eq. 7.13 and 7.14, $u_{0,A}$ represents the particle velocity of material A just behind the shock wave, just before the A and B material interface. Using the interface pressure and particle velocity, the length at which two-dimensional effects within the pellet can be estimated, using the same treatment shown in previous sections. Relevant values for pressure inputs of 2–10 GPa are shown in Table 7.3, and Hugoniot parameters for unreacted PBX 9501 are given in Table 7.1. In Table 7.3, $x_{P,const}$ represents the length into the PBX 9501 that shock attenuation will begin due to the rear rarefaction wave; d_{cone} represents the length into the PBX 9501 where the center of the pellet (and thus, the entire pellet) will begin being affected by the side rarefaction wave as a two-dimensional effect; and d_r represents the estimated run-distance for a full density, pristine pellet [108], [109].

The parameter, $x_{P,const}$ is not a geometry effect, rather it is a function of the input pressure amplitude and thickness, as well as the material properties present at the shock interface; thus, the value is the same even for experiments simulating one-dimensional conditions, if

Table 7.3. Shock calculations in PBX 9501 after receiving a one-dimensional shock from a 12.7 mm diameter PMMA attenuator, where the PBX 9501 diameter is 6 mm.

P **(GPa)**	$x_{P,const}$ **(mm)**	d_{cone} **(mm)**	d_r **(mm)**
2	4.2	2.5	27.5
5	2.6	2.3	5.5± 0.5
10	2.0	2.1	1.5± 0.5

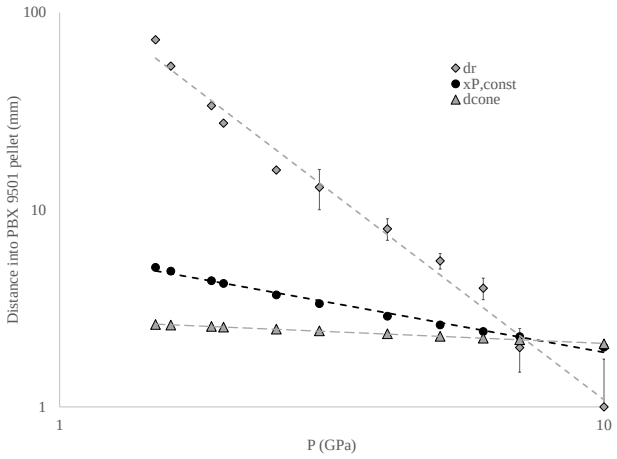

Figure 7.5. Illustration of the intersection of run-distance (d_r) with the constant pressure distance ($x_{P,const}$) and the side rarefaction cone apex distance (d_{cone}) into the explosive sample, PBX 9501. Run-distance data (d_r) taken from [108], [109].

Primasheet 1000 is used as a booster (where the shock thickness is determined by the reaction zone thickness of the booster). This value may be controlled by the flyer thickness in a gas gun or Exploding Foil Initiator (EFI) experiment, however. Because $x_{P,const}$ is relatively constant in comparison with d_r, it may be reasonable to neglect the change in $x_{P,const}$ for the purpose of comparing shock sensitivity of a damaged explosive sample to a pristine explosive sample. This is typical for explosive driven experiments which obtain Pop-plot results.

However, typical explosive driven experiments which return Pop-plot results do simulate one-dimensional conditions; i.e., the diameter of the booster, attenuator, and sample are all large enough such that the side rarefaction wave does not interfere with part of the sample where measurements are recorded. As such, tests which induce interface pressures below ~7 GPa in a 6 mm diameter pellet of PBX 9501 will be particularly susceptible to two-dimensional effects, as the side rarefaction wave will interfere with the entirety of the shock before reaching the run-distance of the explosive (if $P < 7$ GPa, then $d_r > d_{cone}$; see Fig. 7.5).

Care should be taken to note that the value for P in Table 7.3 is the pressure at the interface of the attenuator and explosive sample. Reporting the input pressure at the interface will account for differences in attenuator material properties. Note that when the explosive

sample impedance is greater than that of the attenuator, the pressure at the interface will be greater than the pressure in the attenuator just before the interface.

7.6 Recommendations for future experiments

Here it is suggested that three changes be made to the experimental configuration to overcome the problem of the side rarefaction wave: (1a) *increase the diameter of the booster explosive and attenuator*, (1b) *change the attenuator material to one in which the side rarefaction wave moves at a velocity (R) closer to that of the axial shock (U)*, i.e., use an attenuator material where $U/R \approx 1$, where the base angle of the cone shown in Fig. 7.2 would be 45°, maximizing the length of the shock which has an unaffected center to side rarefaction, and (2), *increase the diameter of the sample explosive such that d_{cone} is greater than the run-distance in the desired pressure input test range*. Changes (1a) and (1b) are attempts to input a near one-dimensional shock wave to the sample explosive, and change (2) is an attempt mitigate effects from the side rarefaction wave within the sample.

7.6.1 Input of a near 1D shock into the sample

Table 7.4 shows a list of candidate and example attenuator materials, sorted by their respective U/R when shocked by this system's booster to show what materials would most favorable for this test. Parameters C_0, s, and ρ_0 used to populate Table 7.4 were taken from both Cooper [102] and Marsh [103].

For instance, if 347 Steel is chosen as the new attenuator material (see Table 7.1 for Hugoniot parameters) and the booster (PS 1000) diameter is increased to 31.8 mm (1.25 in), d_{cone} for such a configuration is increased to 14.2 mm (see Table 7.5). Of course, with a change in attenuator material, there would be a need to find data on pressure outputs for varying lengths of the material, so this change would be limited to publicly available data. Otherwise, a PDV system could be used to calibrate this. Also to be noted in Table 7.5 is the large $x_{P,const}$ value and uncertainty. If this value is very close to the d_{cone} value, then the material will not be useful as an attenuator, as this would limit the achievable pressure range.

Table 7.4. Shock – rarefaction wave velocity ratios of a number of materials when shocked with PS 1000.

Material	U/R
Tungsten ($\rho = 19.2$ g/cc)	.897
Cobalt	.867
347 Steel	.845
304L Stainless Steel	.839
304 Stainless steel	.838
Gold	.834
348 Steel	.817
Brass (High Pb)	.813
2024 Aluminum	.810
Silver	.798
Neoprene	.664
Plexiglass	.642
Adiprene	.622
Teflon	.616
Water	.579
Quartz	.554
Sugar Pine	.525

Table 7.5. Shock calculations in PMMA after receiving the initial shock from the booster, PS 1000.

Parameter	**Calculated value**
$dia_{booster}$ (mm)	31.8
$\ell_{booster}$ (mm)	19.1
$m_{booster}$ (g)	21.7
u_1 (km/s)	0.45
U (km/s)	5.25
R (km/s)	5.89
$x_{P,const}$ (mm)	8.8±7.0
d_{cone} (mm)	14.2

8. THE INFLUENCE OF MICROSTRUCTURE AND β and δ POLYMORPHS ON THE SHOCK SENSITIVITY OF 1,3,4,7-TETRANITRO-1,3,5,7-TETRAZOCTANE (HMX)

The influence on 1,3,5,7-tetranitro-1,3,5,7-tetrazoctane (HMX) shock sensitivity resulting from damage due to phase transition versus that of the polymorphic conformer and crystal lattice change in heated HMX are explored in this work. Samples of class III HMX at 1.24 g/cm^3 are shocked in a modified gap test which yields quantitative, rather than 'go/no-go', results. Microstructural characterization of similarly prepared samples is used to draw conclusions about the primary driver of the difference in sensitivity between pristine β-HMX, thermally induced δ-HMX, and HMX that has spontaneously reverted from $\delta \rightarrow \beta$-HMX. It is found, surprisingly, that large crystals of HMX incur a slight decrease in shock sensitivity after undergoing δ-phase transition and/or spontaneous reversion from $\delta \rightarrow \beta$-HMX. Shock sensitivity results of a significantly smaller HMX particle size distribution are inconclusive using this test setup. Further testing of the small particle size distribution using a different experimental design which allows much lower input pressures may be useful for comparison. The results of this study indicate that while the increased crack cross-sectional area in HMX crystals drives an increase in impact sensitivity, it drives a decrease in sensitivity in the shock regime.

8.1 Background

The change in impact sensitivity due to HMX phase transition has been explored considerably [2], [7], [8], [29], [74], but little attention has been given to the strong shock regime with this regard. Isolation of the physical damage from the change in polymorphic conformer from $\beta \rightarrow \delta$ has not been considered with sensitivity tests of varying stimulus levels. Understanding the potential impacts on the shock sensitivity of HMX is important because it is ubiquitous in defense applications, where thermal and mechanical stimuli could result in changes to microstructural characteristics and even its polymorphic phase.

Shock sensitivity experiments on heated LX-04 charges (85% wt. HMX, 15% wt. Viton) were carried out by Urtiew et al. [110]. The temperatures used in testing were ambient, 150,

170, and 190 °C, where the shots were fired 20 minutes after reaching the target temperature, except in the case of the charges with a target of 190 °C, where the target temperature was held for over an hour. The concept was that the charges below 190 °C would not have sufficient time to undergo $\beta \rightarrow \delta$-phase transition, while the charge at 190 °C would undergo the phase change; as such the change in microstructure would ideally be isolated from the phase change. Unfortunately, significant microstructural effects likely occurred due to binder and HMX decomposition during the long heat soak at 190 °C, and as such the increased shock sensitivity reported [110] may have been due to the additional pore structure added as both phase change and decomposition occurred.

Recent work by Cummock et al. [111] has performed simulations of PBX 9501 initiated via a booster into varying attenuator lengths in a modified gap test. In these simulations, the particle velocity and pressure were monitored at the end of the sample, similar to a measurement using photon doppler velocimetry (PDV). These simulations predicted that a continuously varying particle velocity with attenuator length can be measured at the end of the sample, where there is a clear transition from a developing detonation wave to a fully developed detonation wave at the end of the sample as the attenuator length is decreased. The use of PDV to measure particle velocity at the end of a sample may prove to be a useful diagnostic in determining the shock sensitivity of energetic samples. This sensitivity information could be used to distinguish shock sensitivities of HMX which has been insulted in some way.

The objective of this study is to better understand the influence on shock sensitivity of the δ-HMX polymorphic conformer compared with the effects of microstructural changes that typically occur upon thermally inducing transition from $\beta \rightarrow \delta$-phase HMX. This is carried out by applying similar sample preparation methods and a test matrix as those demonstrated in a recent impact sensitivity study [74], as is discussed in chapter 4.

8.2 Sample Preparation

Pure HMX powder at a poured density was chosen for testing in this study. Pressing of the material would incur significant mechanical damage and thus influence the internal microstructure of the HMX crystals, which is the focus of this work. Grade B class III HMX

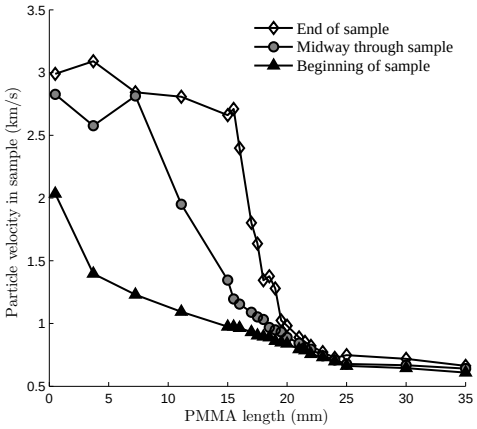

Figure 8.1. Particle velocities predicted in a CTH simulation. The transient region (∼15-25 mm) is where the reaction was still growing to a complete detonation when it arrived at the end of the sample. Reproduced from [111]

(BAE 74BC314-8) was sieved through a #42 mesh sieve such that the samples excluded particles smaller than 355 μm; i.e., the particle size distribution (PSD) for sieved class III HMX shown in recent work [74] is the same as that used for this study.

Additionally, a similar hypothesis test matrix to that used in the recent study on impact sensitivity of δ-phase and β-reverted HMX [74] was used, where HMX is thermally cycled prior to testing. The primary three test groups for which shock sensitivity data was able to be gathered are:

1. large pristine β-HMX ($\beta_{0,lg}$)
2. large thermally induced δ-HMX (δ_{lg})
3. large thermally induced β-HMX reverted from a short-lived δ-phase transition ($\beta_{r,lg}$)

For sieved class III HMX, it was found that a poured density powder bed, after lightly tapping with a spatula on the HMX confiner, was 1.24 g/cm^3; this is consistent with previous work by J.J. Dick [112], [113]. Results from those shock experiments at 1.24 g/cm^3 HMX (pour density after 5-10 minutes of vibration in its confiner) yielded the following Pop-plot [90] points: at P = 0.81 GPa, run distance = 5.2 $\pm$ 0.2 mm, and at P = 2.08 GPa, run distance = 3.06 $\pm$ 0.15 mm (see Pop-plot given in [112]). These Pop-plot values were used in this study to estimate the necessary attenuation values in order to input pressures in HMX samples which would produce a run-to-detonation distance greater than the length of the sample, allowing particle velocity measurement outputs during the shock to detonation transition (SDT) [114]–[116].

A heating profile similar to that suggested by Smilowitz et al. [14] for HMX based pellets was used to induce the δ-phase transition and, where applicable, samples which were desired to incur a β-reversion were allowed to remain in ambient conditions for 72 hours, then heated at 50 °C for 24 hours to remove any water from the samples which may have been acquired during the phase-reversion. Specifically, the heating cycle used to induce phase transition consisted of

1. a thermal ramp from room temperature to 180 °C at 0.6 K/min,
2. a ten hour isotherm at 180 °C,

3. cooling to room temperature at 6 K/min.

This thermal profile input was produced by a Tenney TJR Temperature Chamber. The β-reverted samples were allowed to cool after drying at 50 °C for at least 24 hours before testing. Samples to be tested in the δ-phase were prepared and shot within 9 hours of receiving heat treatment, and were stored in a vacuumed desiccator for much of the time between the end of each sample's heat treatment and testing in order to ensure the samples remained in the δ-phase during the experiment. The times for which samples are expected to remain in the δ-phase are based on the XRD results with time given in [74].

Sample density was controlled by precise mass control of the HMX samples. Sieved class III HMX samples were measured to 304.6 ± 1.0 mg, then placed in a low-sound speed confiner made of thermoplastic polyurethane (TPU), which was carefully tapped once it contained the sample for leveling purposes before placing a 44 g weight on the sample to lightly pack the powder bed and ensure its height was a consistent 3 mm. The resulting samples were 3 mm in height, with a powder bed density of 1.240 ± 0.004 g/cm^3.

8.3 Methods

8.3.1 Simulations

A shock physics hydrocode owned by Sandia National Labs known as CTH [117] was used both to estimate the minimum charge diameter necessary in order to mitigate two-dimensional pressure attenuation in a polymethyl methacrylate (PMMA) attenuator, and to gather insight on the expected trend of particle velocity outputs from low-density HMX during PDV experiments. A resolution of 263 elements/cm in the horizontal direction, and 374 elements/cm in the vertical direction was used. A custom Jones-Wilkins-Lee (JWL) equation of state (EOS) model for Primasheet 1000 booster was used and is discussed in [118]. The Mie-Grüneisen EOS is used for PMMA attenuators (1.186 g/cm^3), polyeurethane sample confinement (1.265 g/cm^3), and copper (8.945 g/cm^3). The built-in SESAME option was used for sapphire, and the version of CTH used was v12.1. The history variable reactive burn (HVRB) model was chosen for the HMX sample because it was designed to describe initiation

and propagation of detonations in heterogeneous explosives. It was used in conjunction with an unreacted EOS input of HMX with density 1.24 g/cm^3 using the Mie-Grüneisen EOS.

It is important to note that the HVRB model uses wedge test data to estimate SDT behavior in energetics, and so it is not expected that the PSD and microstructural characteristics of the samples used in this study will be accounted for in this simulation. Additionally, modelling PMMA pressure attenuation is notoriously difficult, likely due to the variability in PMMA manufacturing processes [119], and so it is not necessarily expected that the Mie-Grüneisen model used here would accurately predict the attenuator length at which the run distance in low density HMX would become greater than the HMX sample length (3 mm). However, the downward trend in HMX output pressure as the attenuator length increases is expected to hold qualitatively, as well as the somewhat steady output pressure reached once the input pressure is high enough to induce a run-distance $\leq$ 3 mm.

8.3.2 Experiments

Previous work [74] contains quantitative analysis on the relative differences in microstructure between $\beta_{0,lg}$, δ_{lg}, and $\beta_{r,lg}$ samples, as well as between similar sample types in a small PSD. The primary differences found between the large particles was that in the δ_{lg} and $\beta_{r,lg}$ samples, a significant increase in cross-sectional surface crack percentage was seen relative to $\beta_{0,lg}$ samples; this significant increase in internal cracks appeared to be the primary driver in the increase in impact sensitivity in δ-phase and β-reverted samples. Of interest here is whether the increase in sensitivity seen for impact holds for the shock regime.

Shock sensitivity experiments in the configuration shown by Fig. 8.2 were performed, where the HMX was a 1.24 g/cm^3 pour-density powder. An RP-80 exploding bridge wire (EBW) with no aluminum cup was used to initiate a Primasheet 1000 booster of 25.875 $\pm$ 0.125 g. The booster provided shock input into a PMMA attenuator of variable length. To reduce the variability in PMMA attenuator properties, all PMMA disks used in this work were sectioned from the same 3 ft. rod (clear scratch and UV resistant cast acrylic rod, McMaster part#: 8528K53).

The PMMA attenuators were cut with a band saw, then smoothed with a 360 grit abrasive, then polished with silk cloth impregnated with 1 μm diamonds. After polishing

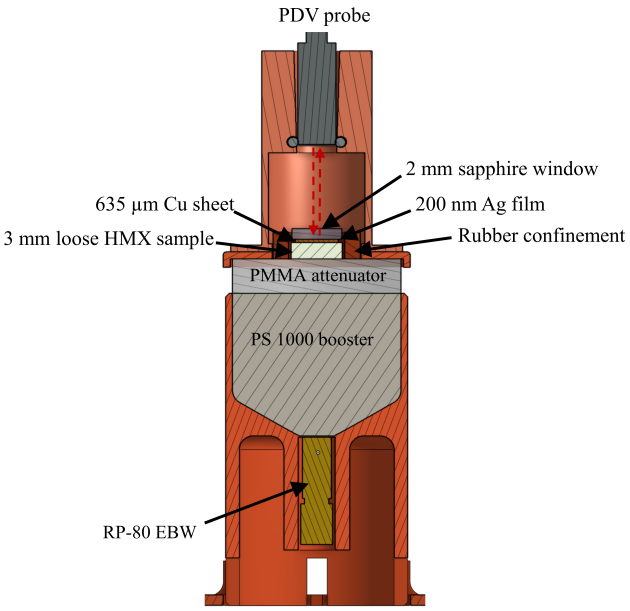

Figure 8.2. Experimental configuration, where the Primasheet 1000 booster is 31.8 mm in diameter, and the poured-density HMX powder is 10.2 mm in diameter. Red arrows represent the 1550 nm laser emitted from the PDV probe. Light red colored parts are 3D printed tough polylactic acid (PLA) holders used primarily for centering and alignment purposes.

and cleaning, they were measured using a micrometer 10-20 times at random positions across their face in order to calculate a standard deviation on the thickness of each PMMA attenuator. Disks were discarded if $2\sigma > 0.15$ mm. Primarily, this controlled the minimum flatness of each attenuator.

The attenuated shock was input from the PMMA attenuator to the HMX sample, which begins a SDT with kinetics based on the magnitude of the pressure input. The output of the HMX sample after 3 mm is routed through a thin copper sheet (110 copper shim stock, McMaster part#: 9300K7) to allow smoothing of the shock. The copper sheet is adhered with a thin layer of cyanoacrylate to a silver coated face of a c-cut sapphire disk (Knight Optical part#: WSC1002; Batch#: 26760). The silver coating is 200 nm thick, placed via electron beam deposition. A 1550 nm laser from a PDV probe (LPF-04-1550-9/125-S-1.8-15-6.2AS-60-3A-1-2 pigtail style focuser with a 15 mm working distance) is transmitted through the 2 mm thick x 10 mm diameter sapphire window and reflected off of the E-beam deposited Ag coating. The predicted spot size is $\sim$20 μm at the $1/e^2$ level at the 15 mm working distance. Focusing and alignment of the probe was performed by adjusting the probe height and angle while attached to a back reflection meter (OZ Optics, BM-100-3A-1550) in order to maximize the reflected power back to the probe. Once an acceptable reading on the back reflection meter was achieved (typically > -10 dB), short working time epoxy was applied to the probe, and it was held in place until the epoxy was sufficiently cured.

The PDV diagnostic was used to measure the particle velocity in c-cut sapphire due to a shockwave propelled by chemical energy from a developing HMX detonation, where input pressures to the HMX are low enough such that the run distance in this low density HMX is > 3 mm. The PDV system used in this work uses heterodyne laser interferometry, and was designed and built by Christian Blum-Sorensen. A schematic of the PDV system is shown in Fig. 8.3.

The particle velocity in the sapphire window is related to the frequency through

$$u_p = (f_2 - f_1)\frac{\lambda_0}{2}C_w \tag{8.1}$$

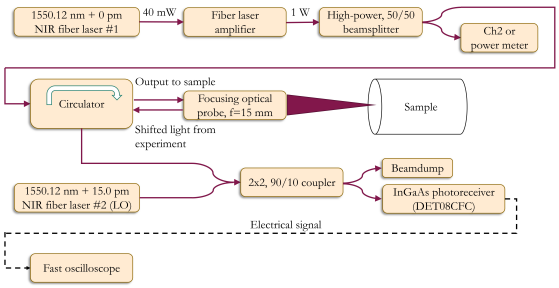

Figure 8.3. Schematic of the heterodyne PDV system used for this work.

where u_p is the particle velocity in the sapphire, f_1 is the baseline frequency (i.e., the frequency output of the system when the laser is reflected from a non-moving surface), f_2 is the frequency history during the moving reflector event, λ_0 is the reference wavelength of the system (1550 nm in this case), and C_w is the window correction factor which is necessary due to the reduced speed of light while passing through the window as opposed to a vacuum, where the window here is sapphire, and the correction factor is proportional to λ_0, and is found by Jensen et al. to be $\sim$0.5786 for a 1550 nm system [120].

To calculate the constant f_1 and the continuous f_2, the raw waveform obtained via PDV was passed through a second-order Butterworth high-pass filter with a cutoff frequency of 1 GHz, followed by a second-order Butterworth low-pass filter with a cutoff frequency of 7 GHz. Note that the cutoff frequency for the low-pass filter was outside the photodetector (DET08CFC InGaAs Biased Detector) bandwidth range of DC to 5 GHz. A short time fourier transform (STFT) was used to analyze the filtered PDV data. The STFT of a signal $f(t)$ is defined according to the integral

$$\mathrm{STFT}(\omega, \tau) = \int_{-\infty}^{\infty} f(t)\omega(t-\tau)\mathrm{e}^{\mathrm{i}\omega t}\mathrm{d}t \tag{8.2}$$

where ω is the frequency, τ is the integration variable, and $\omega(t-\tau)$ represents the window function with horizontal translation τ. The STFT is implemented using the SciPy [121] library in Python [122]. According to the Gabor uncertainty principle for time frequency analysis, the combination of time and frequency resolution must satisfy the inequality

$$(\delta f)\delta t \geq \frac{1}{4\pi} \tag{8.3}$$

where δf and δt represent respectively the frequency resolution in Hertz and the time resolution in seconds. The frequency resolution δf is proportional to the velocity resolution according to Eq. 8.1. The STFT was implemented using a Hamming window. After obtain-

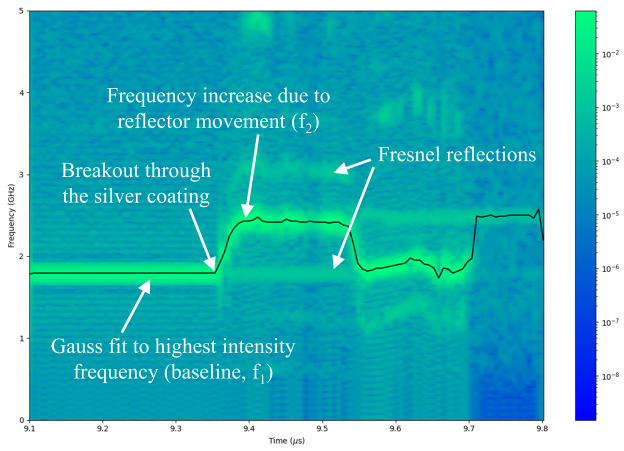

Figure 8.4. An example spectrogram of a baseline shot (no energetic sample), where $t = 0$ represents the time at which the RP-80 EBW is initiated. The event of interest is considered to be within 100 ns of the time of shock breakout through the silver coating.

ing the STFT spectrogram, a least-squares fit between the intensity and frequency at each point in time on the STFT spectrogram was computed using a Gaussian curve fit of the form

$$I(f) = A \cdot \exp\left[-\frac{\left(f - \bar{f}\right)^2}{2\sigma^2}\right] + B \tag{8.4}$$

where $\bar{f}$ is the center frequency, σ is the standard deviation, and A and B are constants. The primary frequency was determined by computing the maximum intensity obtained from Eq. 8.4. An example spectrogram resulting from the above described process using a Hamming window of size ∼12.3 ns on a signal which was yielded from a baseline experiment (no sample, Cu sheet and adhered sapphire window interfacing directly with a 10.5 mm PMMA attenuator) is shown in Fig. 8.4, where the solid black line represents the primary frequency determined by a Gaussian fit (Eq. 8.4). The resulting frequency trace is only considered for 100 ns after breakout of the shockwave through the silver coating, guaranteeing that any shock travelling with an average velocity < 20 km/s does not reach the free surface (which must be at rest for Eq. 8.1 to be valid [120]) of the sapphire window and produce a reverse travelling rarefaction wave during the event of interest.

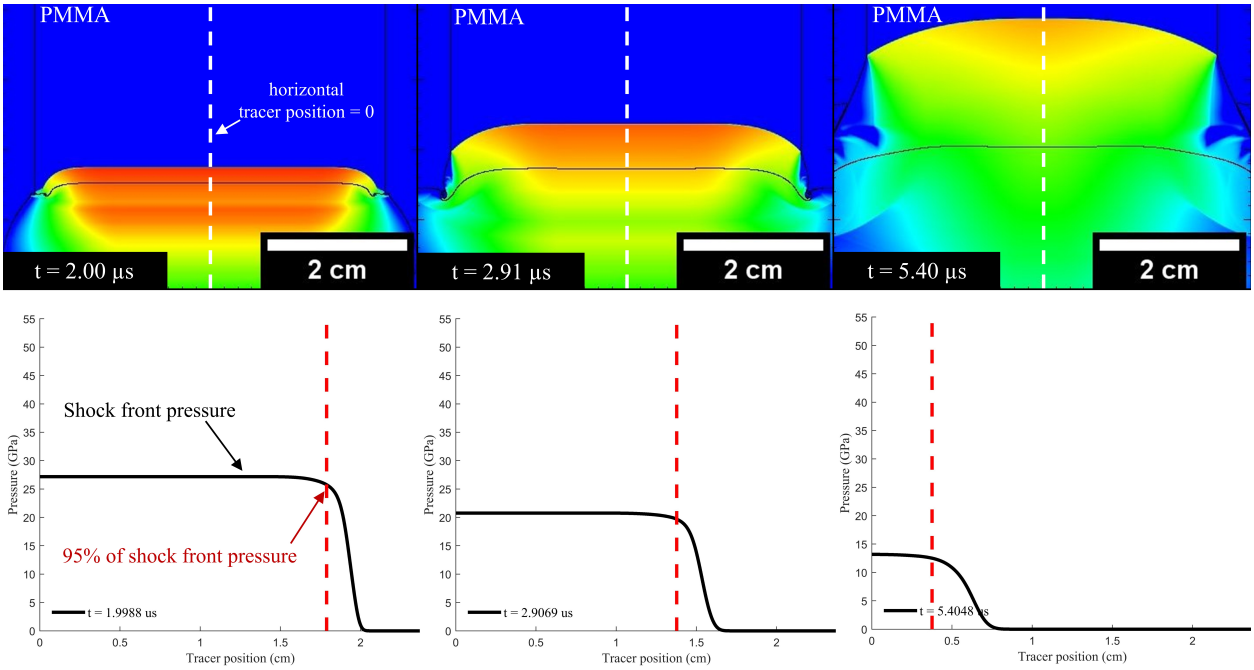

Figure 8.5. Tracking of the radial rarefaction wave in a PMMA attenuator after receiving a shock input from a Primasheet 1000 booster. The top and bottom row are at corresponding times in the simulation, and 'tracer position = 0' on the horizontal axis in the bottom row represents the horizontal center of the pressure maps in the top row.

8.4 Results and discussion

8.4.1 Radial rarefaction simulations

In order to estimate the minimum charge diameter necessary to mitigate two-dimensional effects from the radial rarefaction wave, CTH was used to model shockwave attenuation in PMMA after receiving a shock input from a Primasheet 1000 booster. Select pressure maps from an input shock travelling through a 30 mm PMMA attenuator are shown in the top row of Fig. 8.5. The shock front pressure was monitored radially as it travelled deeper into the PMMA attenuator, and the position of the radial edge at which the shock pressure reached 95% of the center (tracer position = 0) shock pressure was tabulated and the values are given in Fig. 8.6; this process is shown in the bottom row of Fig. 8.5, where 'tracer position = 0' on the horizontal axis represents the center of each corresponding image in the top row (i.e., the pressure map is symmetric about zero on the horizontal axis).

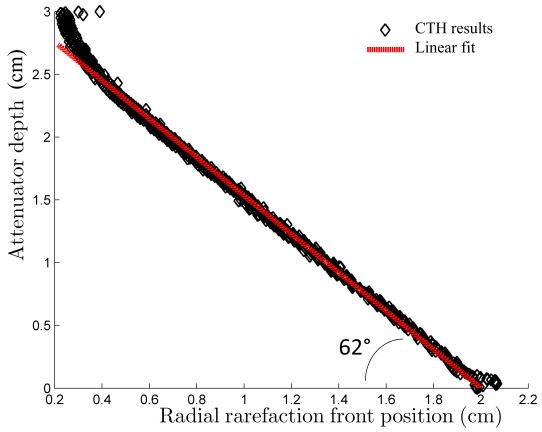

Figure 8.6. Position of the radial rarefaction wave as it travels toward the center of a PMMA attenuator while the shock moves deeper into the length of the PMMA. From the linear fit to the data, an angle at which the rarefaction wave affects the shock can be estimated.

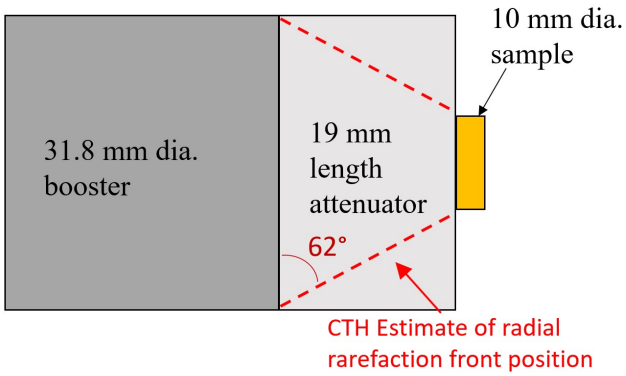

Figure 8.7. Example schematic showing a system in which a right travelling shock would attenuate through 19 mm of PMMA and the radial rarefaction wave would not have an effect on the shock that the sample receives.

The estimated angle of trajectory of the radially travelling rarefaction wave allows one to estimate the necessary diameter of the charge based on the length(s) of the attenuator needed to achieve a given range of pressures. Here, it was estimated to be 62°, indicating, e.g., that a ∼19 mm PMMA attenuator could be used to input a shock from this system to a centered 10 mm diameter sample where the radial rarefaction would not have an effect on the pressure input to the sample; i.e., the sample would receive a radially uniform in magnitude pressure input. An example schematic showing this is given in Fig. 8.7. Using a PMMA attenuator significantly longer than 19 mm would result in two-dimensional pressure attenuation due to the radial rarefaction, and is not ideal. Further details on the radial rarefaction wave and other methods for estimating its trajectory angle are given by Cooper [101].

8.4.2 Particle velocity output simulations

Results of simulations using CTH were shown previous work [111] as a proof of the concept for measuring the particle velocity output of a short PBX 9501 pellet as a modified version of the gap test in order to obtain quantitative information about the progress in the SDT. Similar CTH simulations were run with a configuration akin to that shown in Fig. 8.2 for this work. Figure 8.8 shows a cropped portion of the simulation geometry (the booster is actually 2.7 cm in length in this simulation, but the full booster length is not

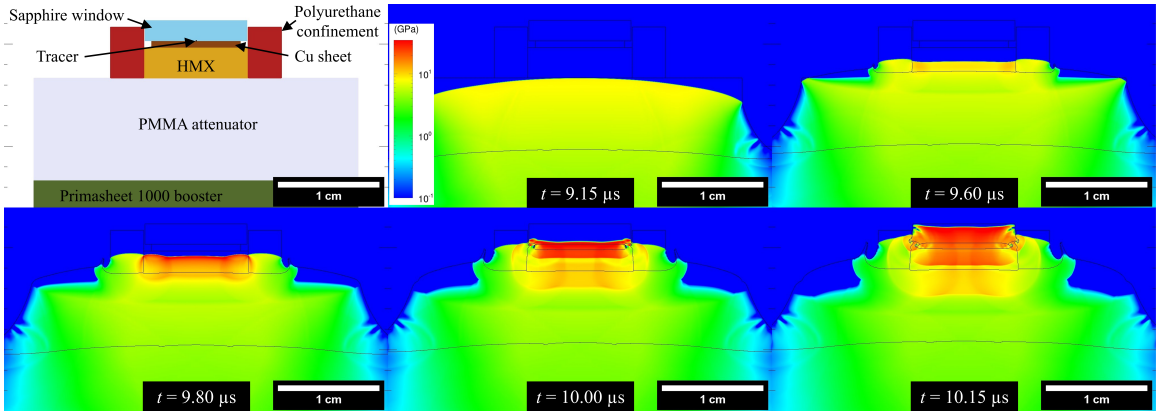

Figure 8.8. Portion of simulation geometry (top-left) and pressure maps at select times during a CTH simulation, where a non-fixed tracer is placed at the copper-sapphire interface. Here it is seen that (1) the shockwave enters the HMX sample at $t = 9.15$ μs, (2) the pressure is still relatively low in the HMX sample at $t = 9.60$ μs, (3) significant chemical energy release has occurred, increasing the pressure by $t = 9.80$ μs, (4) the output shock from the HMX sample has exited the sample and travelled through the Cu sheet by $t = 10.00$ μs, and (5) the shock has nearly travelled through the entire length of the sapphire window by $t = 10.15$ μs.

shown in Fig. 8.8 for the purpose of detailing the event of interest) and pressure maps at select times after breakout of a shockwave from a 10 mm PMMA attenuator. A non-fixed tracer is situated at the interface between the Cu sheet and the sapphire window in order to measure particle velocity after the shock passes into the sapphire window. This simulation was run for 14 different PMMA attenuator lengths, and the tracer particle velocity outputs are shown in Fig. 8.9. In both Fig. 8.8 and 8.9, $t = 0$ represents the time 3.45 μs prior to the reaction beginning in the Primasheet 1000 booster to account for the time delay introduced on average in experiments by the capacitive discharge unit and RP-80 initiator.

It is notable that a subtle shoulder appears in particle velocity traces for attenuators $\geq$ 25 mm, where the particle velocity appears to reach a peak and shortly after sees a secondary sharp rise. In these cases, a secondary shock due to reflection from the HMX/rubber confinement boundary passes over the HMX and appears to increase the rate of detonation development. This is a two-dimensional effect that occurs in the sample rather than the PMMA attenuator, but does not appear to have an effect on results where the simulated attenuator is $\leq$ 25 mm in length.

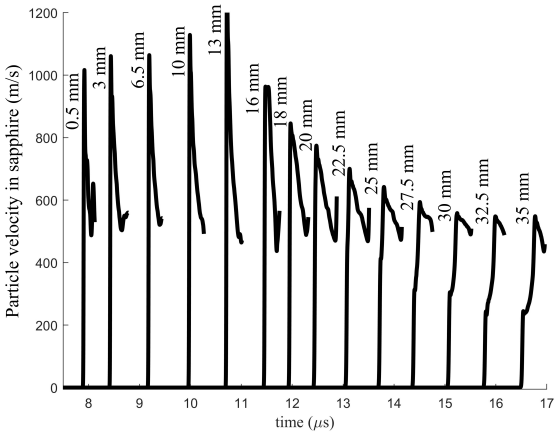

Figure 8.9. Particle velocity traces from a CTH simulation with the geometry shown in Fig. 8.8. Note that only a small time period of each trace is shown for clarity. The length of the attenuator is noted to the left of each trace.

In all cases shown in Fig. 8.9, a sharp acceleration in the particle velocity is seen, resulting in a peak and then a gradual deceleration. After a few hundred nanoseconds, another period of acceleration occurs (only a small portion of this second acceleration is shown on each curve) due to the shock having reached the sapphire free surface (sapphire-air interface) and a rarefaction wave is reflected off of this boundary back into the sapphire window. The second acceleration is seen when this reflected rarefaction wave passes over the tracer particle; however, this occurs well after the event of interest, which is shown at the first velocity peak and occurs less than 100 ns after the breakout of the shock into the sapphire window. Of note is that the peak for the 10 mm case, which has its pressure mapping shown in Fig. 8.8 and its particle velocity trace shown in Fig. 8.9, occurs at $t = 9.99$ μs.

8.4.3 Particle velocity measurements

For the purpose of determining the relative shock sensitivity of $\beta_{0,lg}$, δ_{lg}, and $\beta_{r,lg}$ sample types, a modified gap test was performed where the particle velocity was measured via PDV at the output of each HMX sample. In this way, quantitative information is observed for each 'no-go', rather than binary data typically obtained from a traditional gap test. With a well-characterized pressure input, this test design is an efficient way to estimate run-to-detonation distances, as the output yields data relating to the kinetics of the SDT when combined with results of the same sample type with different pressure inputs. The particle velocity traces, calculated from frequency traces using Eq. 8.1, for the three large PSD sample types are shown in Fig. 8.10.

Additionally, baseline shots were performed with four different length attenuators in order to estimate the pressure input to the HMX. The baseline tests were of the exact same configuration as that shown in Fig 8.2, except the sample was removed, and so the copper sheet (which was adhered to the sapphire window) was directly interfaced with the PMMA attenuator. The results of two of the baseline shots (6.9 mm attenuator and 10.5 mm attenuator) are shown in Fig. 8.11 and 8.12, respectively, along with sample shots with similar lengths of attenuators. In Fig. 8.11 and 8.12, the time scales have been shifted such that the $t = 0$ represents the time just after breakout of the shock through the silver coating, in order to show typical velocity traces over the time of interest (100 ns after breakout).

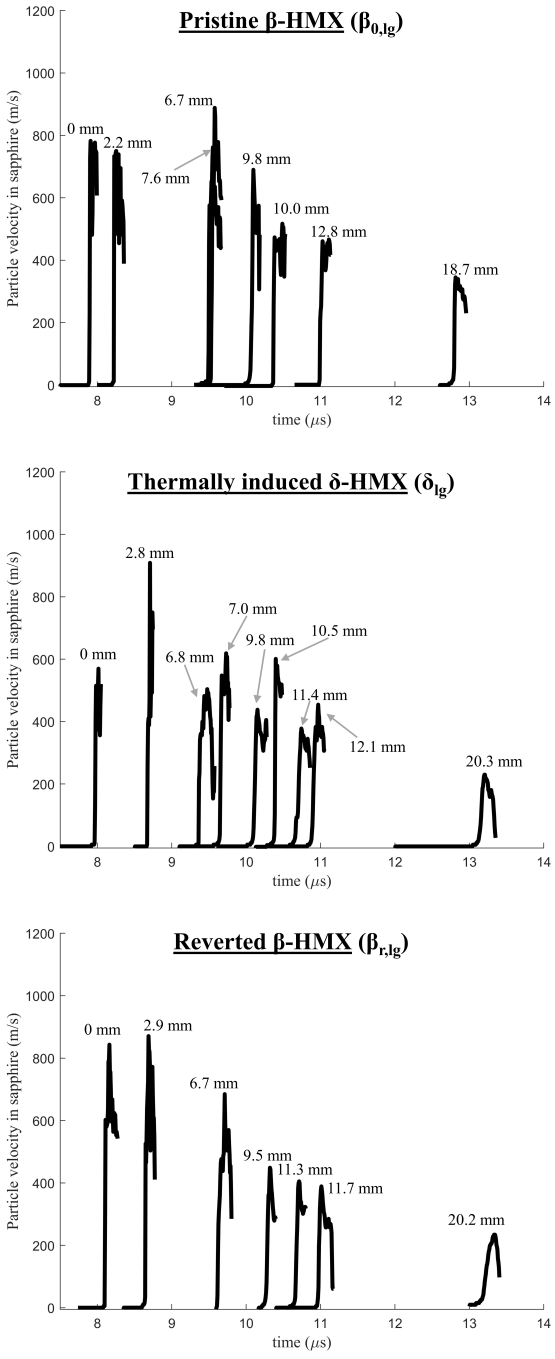

Figure 8.10. The PDV measured particle velocity traces for three sample types of a sieved class III PSD: $\beta_{0,lg}$ (top), δ_{lg} (middle), and $\beta_{r,lg}$ (bottom). The time $t = 0$ refers to the time at which the RP-80 EBW was initiated, where shock breakout through the silver coating occurs ∼8–13 μs afterwards.

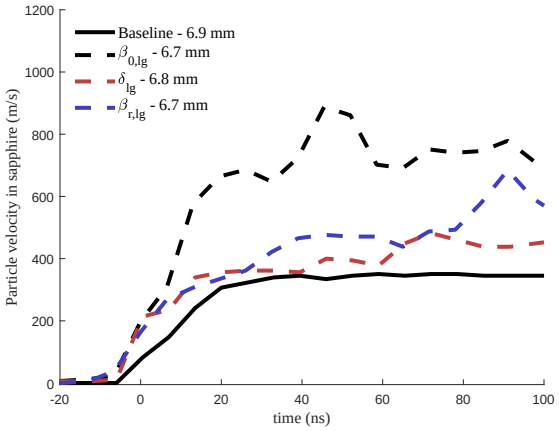

Figure 8.11. Particle velocity traces of a baseline shot with a 6.9 mm PMMA attenuator and select sample shots with attenuators of a similar length. Time $t = 0$ represents the time just after breakout of the shock through the silver coating.

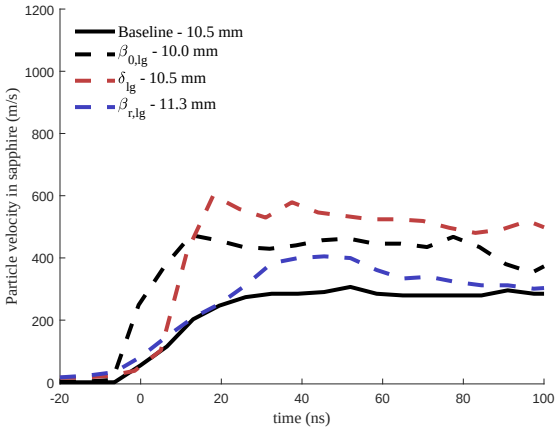

Figure 8.12. Particle velocity traces of a baseline shot with a 10.5 mm PMMA attenuator and select sample shots with attenuators of a similar length. Time $t = 0$ represents the time just after breakout of the shock through the silver coating.

Table 8.1. Shock matching values for calculating the pressure input to low density (1.24 g/cm^3) HMX. Hugoniot fits used for low density HMX were $C_0 =$ 3.05 km/s and $s = 3.66$, and those for 1.186 g/cm^3 PMMA were $C_0 = 2.88$ km/s and $s = 1.36$.

Attenuator length (mm)	**Measured sapphire particle velocity (m/s)**	**Calculated PMMA pressure prior to interface (GPa)**	**Calculated PMMA/HMX Interface pressure (GPa)**
0	491	8.1	10.3
6.9	345	5.6	7.0
10.5	307	4.9	6.1
16.8	213	3.4	4.1

Using shock Hugoniot parameters given for PMMA and sapphire by [123], shock matching based on the baseline output particle velocities can be performed to calculate the pressure just before the PMMA/HMX interface at those lengths. Using Hugoniot parameters for a Grüneisen calculation of HMX given in [112] of $C_0 = 3.05$ km/s and $s = 3.66$, the pressure at the PMMA/HMX sample interface can be calculated, thus yielding the input pressure that the unreacted HMX incurs just as the shock exits the PMMA attenuator. Table 8.1 shows key values associated with this calculation.

It appears from Fig. 8.10 that the $\beta_{0,lg}$ sample has a run-to-detonation distance of 3 mm when the PMMA attenuator length is between 6.7 and 9.8 mm, or a pressure input of $5.7 > P_{in} > 4.9$ GPa. Here, P_{in} is defined as the pressure in the PMMA attenuator immediately prior to reaching the PMMA/HMX interface; though one could certainly, knowing the unreacted sample Hugoniot values, define P_{in} as the pressure at the PMMA/HMX interface, which would be slightly higher than the P_{in} values given here due to the slightly higher impedance of 1.24 g/cm^3 HMX relative to PMMA. The choice of this definition is arbitrary, though the distinction is important to understand. The differences in the baseline tests between these two defined pressure values are shown in columns three and four of Table 8.1.

The $\beta_{r,lg}$ sample appears to be much less shock sensitive relative to $\beta_{0,lg}$, as a run-to-detonation distance of 3 mm is reached when the PMMA attenuator length is between 2.9 and 6.7 mm; i.e., a significantly higher pressure input ($7.0 > P_{in} > 5.8$ GPa) is needed

to reduce the run-to-detonation distance of $\beta_{r,lg}$ to 3 mm as compared with $\beta_{0,lg}$. This is in contrast to the impact sensitivity of $\beta_{r,lg}$ relative to $\beta_{0,lg}$ [74], where $\beta_{r,lg}$ is significantly more impact sensitive than both $\beta_{0,lg}$ and δ_{lg}. Here, the δ_{lg} sample type appears to behave more sporadically than the other two sample types, and determining a meaningful attenuator length range at which the run-to-detonation distance is near 3 mm is difficult. The δ_{lg} HMX run-to-detonation distance appears to be 3 mm when the attenuator length is between 2.8 and 7.0 mm ($7.0 > P_{in} > 5.7$ GPa), which is similar to $\beta_{r,lg}$. The δ_{lg} sample appears to be less shock sensitive than $\beta_{0,lg}$, which is also in contrast to behavior seen in the corresponding study of its impact sensitivity [74].

This behavior could be attributed to the types of voids which are produced in HMX upon transition and reversion to and from δ-phase. It is observed in recent work [74] that the voids produced are primarily in the form of internal cracks, while the amount of porosity which is roughly spherical in shape appears to remain constant in all three sample types. Additionally, it is not known whether or not added cracks in $\beta_{r,lg}$ and δ_{lg} tend to form along slip planes in the HMX crystals, which could have an effect on the ability of the crystal to relieve strain as it is insulted. Additionally of note is the contrast between these results and those shown in work by Urtiew et al. [110]. It is important, however, to recall that Urtiew et al. tested binderized materials, where the thermal input likely caused binder decomposition, delamination of crystals from binders, and crystal-crystal interactions. None of these factors were present in this work, where loose powders were thermally insulted and tested. As such, the contrast between these studies indicates that the factors previously mentioned which are enabled in binderized systems have a significant on the shock sensitivity of a system, and likely overwhelm the effects of intra-crystal defects and polymorphs.

A compilation of the peak particle velocities of the sieved class III HMX samples, as well as the CTH simulations is shown in Fig. 8.13, where only 100 ns after breakout of the shock through the silver coating is considered when determining the peak particle velocity for a given sample. Here again, the estimated pressures shown in Fig. 8.13 represent the shock front pressure in the PMMA attenuator immediately before reaching the interface with the low density HMX sample. One could use Hugoniot parameters for low density HMX [112], [113] and shock matching to estimate the pressure at the PMMA/HMX interface. The

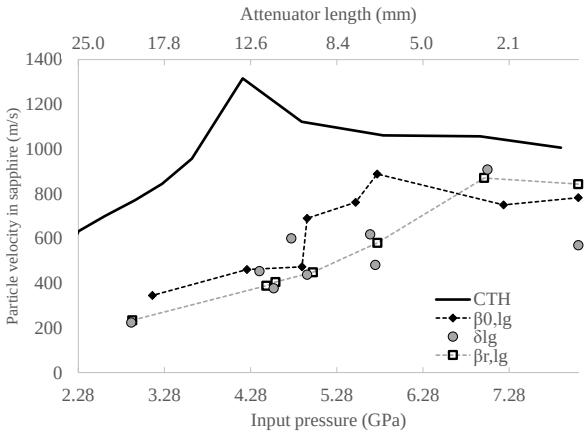

Figure 8.13. Particle velocity peaks (within the first 100 ns after shock breakout) for the three sieved class III HMX sample types, with a comparison to CTH calculations. For clarity, a line does not connect the δ_{lg} sample type, since significant scattering occurred for this particular sample type.

estimated relationship between PMMA attenuator length and shock front pressure in the attenuator (prior to reaching any interface) after receiving an input from the booster in this work is

$$P_a = 8.082\exp\left(-0.051\ell_a\right),$$

where P_a is the shock front pressure in PMMA, and ℓ_a is the length of the PMMA. Use of this relationship in other work, however, is likely inappropriate, again, likely due to the varying manufacturing processes a PMMA causing significant variability in PMMA stress-strain relationship properties [119].

The peak simulated peak in maximum particle velocity vs. attenuator length (Fig. 8.9 and 8.13) occurs at a simulated PMMA attenuator length near 13 mm. Looking more closely at the 13 mm attenuator simulation pressure map, the detonation wave appears to reach full development (where a rapid increase in pressure is seen at the shock front) just before (and very near) the HMX/Cu interface. Shorter attenuator lengths cause the full development to occur at further and further distances from the HMX/Cu interface (i.e., the run-distance-to-detonation is shortened), but it appears that given some time for development, the detonation front thins slightly, and then steadily moves forward. I.e., it appears that this peak in maximum particle velocity occurs because of an overshoot in detonation pressure that occurs

when the detonation reaches full development, which then steadies. This phenomenon seems to appear in experimental values as well. Such an overshoot is common in homogeneous explosives, where a thermal explosion occurs behind the incident shock front which after some time overtakes the initial shock, where an overdriven detonation is observed [124], which then settles down to a steady detonation velocity. Heterogeneous explosives typically show continuous/gradual reactive growth, but many heterogeneous explosives have been shown to exhibit shock initiation behavior that is reminiscent of both mechanisms [124].

Additional shock sensitivity tests were performed using a small PSD (that of $\beta_{0,sm}$ in recent work [74]), but the results were inconclusive because it was necessary to pack the particles to an extremely low density ($\sim$0.81 g/cm^3) in order to avoid mechanically affecting their microstructure, which resulted in very low performing samples in terms of their output pressure and particle velocity, in addition to highly increased sensitivity to shock relative to $\beta_{0,lg}$. The sample length was reduced to 0.625 mm with an attenuator length of 13 mm, and a similar output particle velocity was observed as a case with a sample length of 2.5 mm and no attenuator. A different experimental design appears to be necessary in order to test the small HMX PSD at a very low bulk density while still mitigating two-dimensional effects.

It should be noted, however, that the primary purpose of tests involving a small PSD of HMX is to obtain shock sensitivity results that only have a change in polymorphic conformer, and are minimally affected microstructurally by the thermal cycle which causes a phase transition. In this way, the influence of the δ-phase conformer alone is tested. However, the δ_{lg} and $\beta_{r,lg}$ sample types appear similar in shock sensitivity, and do not appear to incur an increase in shock sensitivity relative to $\beta_{0,lg}$; this indicates that any increase in shock sensitivity caused by the δ-phase conformer is overwhelmed by the influence of the microstructural changes that occur upon phase transition. The result that the δ-phase conformer has little or no influence on the sensitivity relative to the microstructural changes which occur upon phase transition is consistent with results from recent impact sensitivity work [74].

8.5 Limitations

The PDV system used in this study is a recently built system at Purdue University; however, the technique is not novel, and the results are reasonable. In this study, four baseline shots were performed to ensure that the particle velocity results were reasonable and that the analysis was sound; however, further testing could be performed with this system on well-known materials for the purpose of validation of particle velocity results.

8.6 Conclusions

Sample characterization results from recent work [74] indicated the necessary heating profile to transition pristine β-HMX to δ-HMX, and in some cases, subsequently allow reversion to β-HMX, where the microstructure is significantly effected by the phase-transition and reversion, as was also observed via XCT and focused ion beam sectioning and polishing and subsequent SEM imaging. Samples from the same batch and lot of sieved class III HMX, with PSD shown in recent work [74] were tested for changes in shock sensitivity, and compared with simulation results using CTH.

In order to determine the minimum charge diameter necessary while mitigating two-dimensional pressure attenuation, simulations were used to estimate the trajectory angle of a radial rarefaction wave in a PMMA attenuator with input from a Primasheet 1000 booster. It was found that this trajectory angle was 62°. Future work placing multiple PDV probes at varying radii of the PMMA attenuator could be useful for determining the accuracy of the 62° trajectory, but this work used this trajectory angle conservatively to estimate a necessary booster charge diameter of 3.18 cm with a 10 mm diameter sample and a maximum attenuator length of 19 mm.

Simulations in CTH similar in configuration to that of the PDV experiments in this work were performed to gain insight into the behavior of samples upon receiving varying shock inputs as well as to predict and compare trends to experimental results. Using the HVRB model for HMX at 1.24 g/cm^3, tracer results showing particle velocity traces of the sapphire interface significantly overpredicted the lengths of PMMA attenuators necessary to increase the HMX sample run-to-detonation distance to beyond the sample length, which

was 3 mm. This indicates that either the PMMA model predicting the pressure attenuation as a function of PMMA length failed to accurately predict sample input pressures, or the HMX itself is significantly less sensitive than that predicted based on wedge test result fits. A combination of these problems is expected, as PMMA manufacturing process variability tends to introduce significant scatter in its response to insult, and the HVRB model is based on fits to wedge test data, which would not account for the microstructural differences in the samples used in this study.

Experimental particle velocity results indicate that there is not a significant increase in shock sensitivity at this sample length of HMX when it is thermally transitioned to δ-phase or even when allowed to revert to β-phase. In fact, it appears likely that there is a slight decrease in shock sensitivity, again, at this sample length, in δ_{lg} and $\beta_{r,lg}$ relative to $\beta_{0,lg}$. Further detail on the shock sensitivity of the different sample types could be experimentally tested by combining these results with results at a longer sample length; this would allow determination of the slope of the Pop-plot for $\beta_{0,lg}$, δ_{lg}, and $\beta_{r,lg}$, but may require larger diameter samples to avoid two-dimensional effects.

This decrease in shock sensitivity is in contrast to impact sensitivity results, which have indicated that a primary driver for the increase in impact sensitivity is the increase in internal cracks which occur upon transition to δ-HMX. Due to the extreme difference in strain rates between impact and shock insults, many of the mechanisms involved in initiation of the sample material may not be expected to overlap between the two regimes. It may be that at very high strain rates, such as the strong shock regime, cracks are in fact not particularly useful as hot spot sites, rather spherically shaped pores are important for development of hot spots. Further studies detailing typical cracks which occur upon δ-phase transition, such as if the cracks tend to form along slip planes in the crystal, could be useful for interpreting this contrast between impact and shock sensitivity results.

Furthermore, the shape of the experimentally obtained curve showing particle velocity output versus the attenuator length and/or input pressure appears to be qualitatively consistent with that shown by CTH simulations. The rate at which this curve reaches its maximum (where the run-to-detonation distance is equal to the sample length) is controlled by the sample kinetics.

Although there is evidence of the importance of inter- and intra-crystalline porosity in energetic samples for shock sensitivity, whether or not the polymorphic conformer (β- versus δ-HMX) and crystal packing structure are of importance in the shock regime is currently unknown; however, results of this study indicate that the δ conformer of HMX does not significantly increase the shock sensitivity, at a run distance of 3 mm, of HMX.

Further shock senstivity results utilizing a very small PSD of HMX, such as that of FEM HMX used in a recent impact study [74] could be useful for separating the influence of the changing microstructure of HMX from the changing polymorphic conformer. However, in order to avoid influencing the microstructure of FEM HMX upon preparing the sample for shock experiments, one must pack the material to a very low density, which inherently increases the shock sensitivity of the material by introducing numerous potential hot spot sites. Additionally, any increase in shock sensitivity caused by the δ-phase conformer appears to be overwhelmed by the influence of the microstructural changes that occur upon phase transition, since the δ_{lg} and $\beta_{r,lg}$ sample types appear similar in shock sensitivity; this result is consistent with recent impact sensitivity experiments [74].

The modified gap test method shown in this work can be used to estimate pressure thresholds for a given run distance with a relatively small number of experiments. Sample lengths can be changed and subsequently a Pop-plot could be constructed after estimating the pressure at which the run-to-detonation distance is that of the sample length. The method is viable to be more adept and efficient at determining and comparing shock sensitivity relative to traditional gap tests that yield only binary ('go/no-go') results.

9. SUMMARY

Work exploring the effects of assuming a distribution type in drop-weight impact sensitivity tests was presented. It was shown that the effects of the distribution form (between the forms considered) is insignificant, and thus it is suggested that the most convenient and/or computationally effecient distribution form be used when analyzing impact sensitivity results. Further work exploring special cases of the log-logistic distribution is recommended.

Further work was presented on determining the effects of microstructure on the change to a drop-weight impact sensitivity distribution. Studies on the the $\beta \rightarrow \delta$-phase transition in HMX and its effect on the microstructure of varying crystal sizes were presented, in an effort to assist in understanding the influence of conformer and crystalline structure on impact sensitivity, rather than a conflation of the polymorph and induced damage and density changes influence on impact sensitivity. It was shown that large crystals incur an increase in cracks, while small crystal microstructure appears relatively pristine after phase transition. Additionally, the microstructural change is the primary driver in impact sensitivity, while the δ-conformer plays little or no role in the increased impact sensitivity. Previous studies showing an increase in sensitivity while attempting to control microstructure include bindarized samples, where factors such as binder decomposition/delamination and crystal-crystal interactions during heating occur, which appear to play a significant role in impact sensitivity but were controlled for in this work by the use of nonbinderized samples.

Similarly, of interest is the change in shock sensitivity due to polymorph and microstructural changes independently, and work which used a similar hypothesis test matrix to that of the impact study was presented. A modified gap test to evaluate shock sensitivity was shown, which is more efficient than traditional 'go/no-go' gap tests. It was found that neither the microstructural or polymorphic conformer changes which occur during HMX thermal transition to δ-phase cause a significant increase in sensitivity at the charge length considered (3 mm). Multiple sample lengths could be tested in future work to construct a Pop-plot for each material ($\beta_{0,lg}$, δ_{lg}, and $\beta_{r,lg}$); however, larger booster charges and sample diameters would likely be necessary to avoid two-dimensional rarefaction effects at significantly longer sample lengths. Additionally, a contrast to previous shock sensitivity work on δ-HMX should

be noted, where binderized samples were used. Similarly to the impact tests, the contrast indicates that the effects of binder decomposition/delamination and crystal-crystal interaction during heating may play a significant role in the sensitization of samples, and in the shock regime, these effects appear to overwhelm those of intra-crystal defects and polymorphic conformer.

REFERENCES

[1] H. Czerski, M. Greenaway, W. Proud, and J. Field, "β-δ phase transition during drop-weight impact on cyclotetramethylene-tetranitroamine," *Journal of applied physics*, vol. 96, no. 8, pp. 4131–4134, 2004.

[2] H. H. Cady, *Studies on the Polymorphs of HMX*. Los Alamos Scientific Laboratory of the University of California, 1962, vol. 2652.

[3] W. Moodie, "Safety considerations in grinding HMX," Mound Facility, Miamisburg, OH (USA), Tech. Rep., 1978.

[4] J. Rogers, "Physical and chemical properties of rdx and hmx," *Holston Army Ammunition Plant*, 1962, I was not able to obtain a copy of this report.

[5] P. Main, R. Cobbledick, and R. Small, "Structure of the fourth form of 1, 3, 5, 7-tetranitro-1, 3, 5, 7-tetraazacyclooctane (γ-hmx), 2c4h8n8o8. 0.5 h2o," *Acta Crystallographica Section C: Crystal Structure Communications*, vol. 41, no. 9, pp. 1351–1354, 1985.

[6] M. Herrmann, W. Engel, and N. Eisenreich, "Thermal analysis of the phases of hmx using x-ray diffraction," *Zeitschrift für Kristallographie-Crystalline Materials*, vol. 204, no. 1-2, pp. 121–128, 1993.

[7] M. Herrmann, W. Engel, and N. Eisenreich, "Thermal expansion, transitions, sensitivities and burning rates of HMX," *Propellants, Explosives, Pyrotechnics*, vol. 17, no. 4, pp. 190–195, 1992.

[8] B. W. Asay, B. F. Henson, L. B. Smilowitz, and P. Dickson, "On the difference in impact sensitivity of beta and delta HMX," *Energetic Materials*, vol. 21, no. 4, pp. 223–235, 2003.

[9] C.-S. Yoo and H. Cynn, "Equation of state, phase transition, decomposition of β-HMX (octahydro-1, 3, 5, 7-tetranitro-1, 3, 5, 7-tetrazocine) at high pressures," *The Journal of Chemical Physics*, vol. 111, no. 22, pp. 10 229–10 235, 1999.

[10] R. J. Karpowicz and T. Brill, "The beta to delta transformation of HMX–its thermal analysis and relationship to propellants," *Aiaa Journal*, vol. 20, no. 11, pp. 1586–1591, 1982.

[11] C. Saw, "The 12th international detonation symposium, August 11–16, 2002, San Diego, CA, United States," UCRL-JC-145228, Tech. Rep., 2002.

[12] A. Landers and T. Brill, "Pressure-temperature dependence of the β-δ polymorph interconversion in octahydro-1, 3, 5, 7-tetranitro-1, 3, 5, 7-tetrazocine," *The Journal of Physical Chemistry*, vol. 84, no. 26, pp. 3573–3577, 1980.

[13] B. L. Weeks, C. M. Ruddle, J. M. Zaug, and D. J. Cook, "Monitoring high-temperature solid–solid phase transitions of HMX with atomic force microscopy," *Ultramicroscopy*, vol. 93, no. 1, pp. 19–23, 2002.

[14] L. Smilowitz, B. Henson, B. Asay, and P. Dickson, "The β–δ phase transition in the energetic nitramine-octahydro-1, 3, 5, 7-tetranitro-1, 3, 5, 7-tetrazocine: Kinetics," *The Journal of chemical physics*, vol. 117, no. 8, pp. 3789–3798, 2002.

[15] J. Field, S. Palmer, P. Pope, R. Sundararajan, and G. Swallowe, "Mechanical properties of PBXs and their behaviour during drop-weight impact," in *Proc. 8th Symp.(Int.) on Detonation*, Naval Surface Weapons Center White Oak, MD, 1985, pp. 635–44.

[16] G. T. Afanas'ev and V. K. Bobolev, *Initiation of solid explosives by impact*. Israel Program for Scientific Translations, 1971.

[17] E. K. Rideal and A. Robertson, "The sensitiveness of solid high explosives to impact," *Proceedings of the Royal Society of London. Series A. Mathematical and Physical Sciences*, vol. 195, no. 1041, pp. 135–150, 1948.

[18] F. P. Bowden and O. Gurton, "Initiation of solid explosives by impact and friction: The influence of grit," *Proceedings of the Royal Society of London. Series A. Mathematical and Physical Sciences*, vol. 198, no. 1054, pp. 337–349, 1949.

[19] F. P. Bowden and O. Gurton, "Birth and growth of explosion in liquids and solids initiated by impact and friction," *Proceedings of the Royal Society of London. Series A. Mathematical and Physical Sciences*, vol. 198, no. 1054, pp. 350–372, 1949.

[20] B. Henson, B. Asay, R. Sander, S. Son, J. Robinson, and P. Dickson, "Dynamic measurement of the HMX β-δ phase transition by second harmonic generation," *Physical review letters*, vol. 82, no. 6, p. 1213, 1999.

[21] B. Henson, L. Smilowitz, B. Asay, and P. Dickson, "The β–δ phase transition in the energetic nitramine octahydro-1, 3, 5, 7-tetranitro-1, 3, 5, 7-tetrazocine: Thermodynamics," *The Journal of chemical physics*, vol. 117, no. 8, pp. 3780–3788, 2002.

[22] A. Metzner and C. Coffey, "Hot spot initiation of plastic bonded explosives during the rapid flow phase of the drop weight impact test," in *10th International Detonation Symposium*, 1993.

[23] R. Meyer, *Explosivstoffe. 5. aufl. verlag chemie*, I wasn't able to find a copy of this report, 1979.

[24] W. Jeffers, "The impact sensitivity of HMX polymorphs," ERDE 1/R/58, Tech. Rep., Feb. 1958, For Official Use Only; could not find a copy of this report.

[25] A. Blomquist, "The polymorphism of HMX," *OSRD-1227*, vol. 27, 1943.

[26] W. Bachmann, A. Blomquist, L. Davy, D. MacDougall, and F. Whitmore, "The impact sensitivity of HMX and of RDX-HMX mixtures," OSRD-4099, Tech. Rep., Sep. 1944, Could not find a copy of this report.

[27] X. Song, Y. Wang, C. An, X. Guo, and F. Li, "Dependence of particle morphology and size on the mechanical sensitivity and thermal stability of octahydro-1, 3, 5, 7-tetranitro-1, 3, 5, 7-tetrazocine," *Journal of Hazardous Materials*, vol. 159, no. 2-3, pp. 222–229, 2008.

[28] L. Smilowitz, B. Henson, B. Asay, and P. Dickson, "A model of the β- δ phase transition in PBX9501," in *Twelfth International Detonation Symposium, volume ONR*, Citeseer, 2002, pp. 333–05.

[29] P. Peterson, K.-Y. Lee, D. Moore, R. Scharff, and G. Avilucea, "The evolution of sensitivity in HMX-based explosives during the reversion from delta to beta phase," in *AIP Conference Proceedings*, AIP, vol. 955, 2007, pp. 987–990.

[30] G. Yan, Z. Fan, S. Huang, J. Liu, Y. Wang, Q. Tian, L. Bai, J. Gong, G. Sun, and X. Wang, "Phase retransformation and void evolution of previously heated HMX-based plastic-bonded explosive in wet air," *The Journal of Physical Chemistry C*, vol. 121, no. 37, pp. 20 426–20 432, 2017.

[31] Brill, "Unknown," in *Uknown*, I was not able to find a copy of this article with the above information, JCP, vol. 82, 1978, pp. 1912–1917.

[32] L. B. Smilowitz, B. F. Henson, B. W. Asay, and V. Levitas, "Unifying observations of solid-solid phase transitions in HMX," Los Alamos National Lab.(LANL), Los Alamos, NM (United States), Tech. Rep., 2011.

[33] L. Smilowitz, B. Henson, and J. Romero, "Intercomparison of calorimetry, raman spectroscopy, and second harmonic generation applied to solid- solid phase transitions," *The Journal of Physical Chemistry A*, vol. 113, no. 35, pp. 9650–9657, 2009.

[34] T. Brill and R. Karpowicz, "Solid phase transition kinetics. the role of intermolecular forces in the condensed-phase decomposition of octahydro-1, 3, 5, 7-tetranitro-1, 3, 5, 7-tetrazocine," *The Journal of Physical Chemistry*, vol. 86, no. 21, pp. 4260–4265, 1982.

[35] D. Price, "Shock sensitivity, a property of many aspects," NAVAL ORDNANCE LAB WHITE OAK MD, Tech. Rep., 1970.

[36] L. C. Smith, *Los Alamos National Laboratory explosives orientation course: Sensitivity and sensitivity tests*. Los Alamos National Laboratory, 1987.

[37] A. Barua, S. Kim, Y. Horie, and M. Zhou, "Prediction of probabilistic ignition behavior of polymer-bonded explosives from microstructural stochasticity," *Journal of Applied Physics*, vol. 113, no. 18, p. 184 907, 2013.

[38] C. M. Tarver and S. K. Chidester, "On the violence of high explosive reactions," in *ASME/JSME 2004 Pressure Vessels and Piping Conference*, American Society of Mechanical Engineers Digital Collection, 2008, pp. 3–12.

[39] A. Mellor, T. Boggs, J. Covino, C. Dickinson, D. Dreitzler, L. Thorn, R. Frey, P. Gibson, W. Roe, M. Kirshenbaum, *et al.*, "Hazard initiation in solid rocket and gun propellants and explosives," *Progress in energy and combustion science*, vol. 14, no. 3, pp. 213–244, 1988.

[40] J. Cornfield and N. Mantel, "Some new aspects of the application of maximum likelihood to the calculation of the dosage response curve," *Journal of the American Statistical Association*, vol. 45, no. 250, pp. 181–210, 1950.

[41] J. Berkson, "A statistically precise and relatively simple method of estimating the bioassay with quantal response, based on the logistic function," *Journal of the American Statistical Association*, vol. 48, no. 263, pp. 565–599, 1953.

[42] C. Guymon, *Statistical relative comparison (SRC) method*, www.sms-ink.com, Safety Management Services, 1847 West 9000 South, Suite 205, West Jordan, Utah 84088, 2014.

[43] R. Kassen and T. Bataillon, "Distribution of fitness effects among beneficial mutations before selection in experimental populations of bacteria," *Nature genetics*, vol. 38, no. 4, p. 484, 2006.

[44] J. Heintzenberg, "Properties of the log-normal particle size distribution," *Aerosol Science and Technology*, vol. 21, no. 1, pp. 46–48, 1994.

[45] J. C. Thomas, "The determination of log normal particle size distributions by dynamic light scattering," *Journal of colloid and interface science*, vol. 117, no. 1, pp. 187–192, 1987.

[46] O. G. Raabe, "Particle size analysis utilizing grouped data and the log-normal distribution," *Journal of Aerosol Science*, vol. 2, no. 3, pp. 289–303, 1971.

[47] J. Ayres, "Standardization of the small scale gap test used to measure the sensitivity of explosives," NAVAL ORDNANCE LAB WHITE OAK MD, Tech. Rep., 1961.

[48] J. N. Ayres, L. J. Montesi, and R. J. Bauer, "Small scale gap test (SSGT) data compilation: 1959-1972. volume 1. unclassified explosives," NAVAL ORDNANCE LAB WHITE OAK MD, Tech. Rep., 1973.

[49] M. H. Keshavarz, H. Motamedoshariati, H. R. Pouretedal, M. K. Tehrani, and A. Semnani, "Prediction of shock sensitivity of explosives based on small-scale gap test," *Journal of hazardous materials*, vol. 145, no. 1-2, pp. 109–112, 2007.

[50] D. Price, A. Clairmont Jr, and J. Erkman, "The nol large scale gap test. iii. compilation of unclassified data and supplementary information for interpretation of results," NAVAL ORDNANCE LAB WHITE OAK MD, Tech. Rep., 1974.

[51] D. Price and T. Liddiard Jr, "The small scale gap test: Calibration and comparison with the large scale gap test," NAVAL ORDNANCE LAB WHITE OAK MD, Tech. Rep., 1966.

[52] R. Stresau Jr and L. Starr Jr, "Some studies of the propagation of detonation between small confined explosive charges," NAVAL ORDNANCE LAB WHITE OAK MD, Tech. Rep., 1950.

[53] B. Tan, X. Long, R. Peng, H. Li, B. Jin, and S. Chu, "On the shock sensitivity of explosive compounds with small-scale gap test," *The Journal of Physical Chemistry A*, vol. 115, no. 38, pp. 10 610–10 616, 2011.

[54] J. Ayres, L. Hampton, I. Kabik, and A. Solem, "Varicomp. a method for determining detonation-transfer probabilities," NAVAL ORDNANCE LAB WHITE OAK MD, Tech. Rep., 1961.

[55] S. Walley, J. Field, and M. Greenaway, "Crystal sensitivities of energetic materials," *Materials Science and Technology*, vol. 22, no. 4, pp. 402–413, 2006.

[56] M. Kendall and A. Stuart, "The advanced theory of statistics, vol. 2, hafner," *New York*, 1967.

[57] B. T. Never, "A D-optimality based sensitivity test," *Technometrics*, vol. 36, no. 1, pp. 61–70, 1994.

[58] A. Golub and F. E. Grubbs, "Analysis of sensitivity experiments when the levels of stimulus cannot be controlled," *Journal of the American Statistical Association*, vol. 51, no. 274, pp. 257–265, 1956.

[59] N. Gunduz and E. Fokoue, "On the predictive analytics of the probit and logit link functions," Gazi University, Tech. Rep., 2013, Accessed from http://scholarworks.rit.edu/article/1235.

[60] W. J. Dixon and A. M. Mood, "A method for obtaining and analyzing sensitivity data," *Journal of the American Statistical Association*, vol. 43, no. 241, pp. 109–126, 1948.

[61] N. R. Cummock, A. D. Casey, and S. F. Son, "The effect of the chosen distribution form on reaction probability estimates from drop-weight impact results," *Journal of Energetic Materials*, pp. 1–22, 2020.

[62] J. D. Yeager, E. B. Watkins, A. L. Higginbotham Duque, and J. Majewski, "The thermal and microstructural effect of plasticizing HMX-nitrocellulose composites," *Journal of Energetic Materials*, vol. 36, no. 1, pp. 13–28, 2018.

[63] C. K. Saw, "Kinetics of hmx and phase transitions: Effects of grain size at elevated temperature," in *12th International Detonation Symposium*, 2002, pp. 11–16.

[64] T. M. Willey, L. Lauderbach, F. Gagliardi, T. van Buuren, E. A. Glascoe, J. W. Tringe, J. R. Lee, H. K. Springer, and J. Ilavsky, "Mesoscale evolution of voids and microstructural changes in HMX-based explosives during heating through the β-δ phase transition," *Journal of Applied Physics*, vol. 118, no. 5, p. 055 901, 2015.

[65] X. Zhang, G. Xu, J. Xu, and W. Wang, "A study about impact sensitivity of ultrafine hmx and rdx," *Chin J Explos Propell*, vol. 22, no. 1, 33e6, 1999.

[66] C. Lu and J. Zhang, "Influence of particle size on the impact sensitivity of hmx," *Explosion and Shock Waves*, vol. 23, no. 5, pp. 472–474, 2003.

[67] M. R. Salazar, S. L. Thompson, K. E. Laintz, T. O. Meyer, and R. T. Pack, "Degradation of a poly (ester urethane) elastomer. iv. sorption and diffusion of water in pbx 9501 and its components," *Journal of applied polymer science*, vol. 105, no. 3, pp. 1063–1076, 2007.

[68] M. M. Kuklja, R. V. Tsyshevsky, and O. Sharia, "Effect of polar surfaces on decomposition of molecular materials," *Journal of the American Chemical Society*, vol. 136, no. 38, pp. 13 289–13 302, 2014.

[69] HMXDetailSpecification, "Military standard MIL-DTL-45444C," *US Dept. of Defence*, 1996.

[70] D. Sullenger, J. Cantrell, and T. Beiter, private communication, The private communication was not with the author of this manuscript, rather, the reference was found in a Powder diffraction database.

[71] D. Sullenger, J. Cantrell, and T. Beiter, "X-ray powder diffraction patterns of energetic materials," *Powder Diffraction*, vol. 9, no. 1, pp. 2–14, 1994.

[72] A. D. Casey and D. Arthur, *SenPy*, https://github.com/ACasey13/senpy, [Online; accessed Sept. 16th, 2020], 2020.

[73] J. J. Mares, B. D. Hardin, C. G. Butler, J. Vitarelli, and C. Molek, "Effect of shape resolution on the simulated energetic response of shock induced pore collapse within HMX," *APS Topical Group on Shock Compression of Condensed Matter*, vol. 64, no. 8, 2019.

[74] N. R. Cummock, J. R. Lawrence, M. Örnek, and S. F. Son, "The influence of microstructure and conformational polymorph on the drop-weight impact sensitivity of δ-phase HMX," *Submitted for peer review in the Journal of Energetic Materials in October 2020*, 2020.

[75] A. Campbell, W. Davis, and J. Travis, "Shock initiation of detonation in liquid explosives," *The Physics of Fluids*, vol. 4, no. 4, pp. 498–510, 1961.

[76] M. A. Wood, M. J. Cherukara, E. M. Kober, and A. Strachan, "Ultrafast chemistry under nonequilibrium conditions and the shock to deflagration transition at the nanoscale," *The Journal of Physical Chemistry C*, vol. 119, no. 38, pp. 22 008–22 015, 2015.

[77] R. Engelke, "Effect of a physical inhomogeneity on steady-state detonation velocity," *The Physics of Fluids*, vol. 22, no. 9, pp. 1623–1630, 1979.

[78] R. Engelke, "Effect of a chemical inhomogeneity on steady-state detonation velocity," *The Physics of Fluids*, vol. 23, no. 5, pp. 875–880, 1980.

[79] A. Campbell and R. Engelke, "Diameter effect in high-density heterogeneous explosives," Los Alamos Scientific Lab., N. Mex.(USA), Tech. Rep., 1976.

[80] O. Petel, D. Mack, A. Higgins, R. Turcotte, and S. Chan, "Minimum propagation diameter and thickness of high explosives," *Journal of Loss Prevention in the Process Industries*, vol. 20, no. 4, pp. 578–583, 2007.

[81] J. J. Lee, M. Brouillette, D. L. Frost, and J. H. Lee, "Effect of diethylenetriamine sensitization on detonation of nitromethane in porous media," *Combustion and Flame*, vol. 100, no. 1-2, pp. 292–300, 1995.

[82] R. Engelke, "Effect of the number density of heterogeneities on the critical diameter of condensed explosives," *The Physics of fluids*, vol. 26, no. 9, pp. 2420–2424, 1983.

[83] J. Bdzil, "Steady-state two-dimensional detonation," *Journal of Fluid Mechanics*, vol. 108, pp. 195–226, 1981.

[84] M. Carroll and A. Holt, "Static and dynamic pore-collapse relations for ductile porous materials," *Journal of Applied Physics*, vol. 43, no. 4, pp. 1626–1636, 1972.

[85] B. Khasainov, A. Attetkov, and A. Borisov, "Shock-wave initiation of porous energetic materials and visco-plastic model of hot spots," *CHEMICAL PHYSICS REPORTS C/C OF KHIMICHESKAIA FIZIKA*, vol. 15, pp. 987–1062, 1996.

[86] J. Kang, P. Butler, and M. Baer, "A thermomechanical analysis of hot spot formation in condensed-phase, energetic materials," *Combustion and flame*, vol. 89, no. 2, pp. 117–139, 1992.

[87] R. B. Frey, "The initiation of explosive charges by rapid shear," DTIC Document, Tech. Rep., 1980.

[88] S. A. Hambir, H. Kim, D. D. Dlott, and R. B. Frey, "Real time ultrafast spectroscopy of shock front pore collapse," *Journal of Applied Physics*, vol. 90, no. 10, pp. 5139–5146, 2001.

[89] C. L. Mader, "Initiation of detonation by the interaction of shocks with density discontinuities," *The Physics of Fluids*, vol. 8, no. 10, pp. 1811–1816, 1965.

[90] J. Ramsay and A. Popolato, "Analysis of shock wave and initiation data for solid explosives," in *Proceedings of the Fourth Symposium (International) on Detonation*, 1965, pp. 233–238.

[91] P. W. Cooper, *Explosives Engineering*. John Wiley & Sons, Nov. 1996, See section 22.2.2: Run Distance Versus Pressure.

[92] J. F. Baytos, *LASL explosive property data*. Univ of California Press, 1980, vol. 4.

[93] R. Gustavsen and S. Sheffield, "Shock initiation of new and aged pbx 9501 measured with embedded electromagnetic particle velocity gauges," Los Alamos National Lab., NM (US), Tech. Rep., 2000.

[94] K. S. Vandersall, C. M. Tarver, F. Garcia, and S. K. Chidester, "On the low pressure shock initiation of octahydro-1, 3, 5, 7–tetranitro-1, 3, 5, 7-tetrazocine based plastic bonded explosives," *Journal of Applied Physics*, vol. 107, no. 9, p. 094 906, 2010.

[95] J. Cutting, C. Chow, H. Chau, R. Hodgin, and R. Lee, "A small-scale safety test for initiation components," Lawrence Livermore National Lab., CA (US), Tech. Rep., 2002.

[96] H. Berghout, S. Son, C. Skidmore, D. Idar, and B. Asay, "Combustion of damaged pbx 9501 explosive," *Thermochimica Acta*, vol. 384, no. 1-2, pp. 261–277, 2002.

[97] A. Weissberger, *Technique of Organic Chemistry*. Interscience Publishers, 1956, vol. 3, Part I, Chapter III: Crystallization and Recrystallization.

[98] L. Smilowitz, B. Henson, B. Asay, and P. Dickson, "The β–δ phase transition in the energetic nitramine-octahydro-1, 3, 5, 7-tetranitro-1, 3, 5, 7-tetrazocine: Kinetics," *The Journal of chemical physics*, vol. 117, no. 8, pp. 3789–3798, 2002.

[99] P. Peterson, M. Fletcher, and E. Roemer, "Influence of pressing intensity on the microstructure of pbx 9501," *Energetic Materials*, vol. 21, no. 4, pp. 247–260, 2003.

[100] L. Davison, Y. Horie, and M. Shahinpoor, Eds., *High-Pressure Shock Compression of Solids IV: Response of Highly Porous Solids to Shock Loading*. Springer Science & Business Media, 1997, ch. 2, pp. 46–47, See section 2.5.2: Distance-to-Detonation Versus Particle Size.

[101] P. W. Cooper, *Explosives Engineering*. John Wiley & Sons, Nov. 1996, See section 22.2.3: Thick- Versus Thin-Pulse Criteria & 22.2.4: Effects of Impact Shock Diameter.

[102] P. W. Cooper, *Explosives Engineering*. John Wiley & Sons, Nov. 1996, See section 17.2: The U-u Plane.

[103] S. P. Marsh, *LASL shock Hugoniot data*. Univ of California Press, 1980, vol. 5.

[104] P. W. Cooper, *Explosives Engineering*. John Wiley & Sons, Nov. 1996, See section 20.2.3: Estimating the P-u Hugoniot of detonation products.

[105] D. E. Kittell, N. R. Cummock, and S. F. Son, "Reactive flow modeling of small scale detonation failure experiments for a baseline non-ideal explosive," *Journal of Applied Physics*, vol. 120, no. 6, p. 064 901, 2016.

[106] EBAD. (). "PRIMASHEET 1000 flexible sheet explosive (DETASHEET flexible explosive)," Ensign-Bickford Aerospace & Defense Company, [Online]. Available: https://www.eba-d.com/assets/product-sheets/Primasheet-1000-Flexible-Sheet-Explosive-Product-Sheet.pdf.

[107] S. I. Jackson, C. B. Kiyanda, and M. Short, "Experimental observations of detonation in ammonium-nitrate-fuel-oil (anfo) surrounded by a high-sound-speed, shockless, aluminum confiner," *Proceedings of the Combustion Institute*, vol. 33, no. 2, pp. 2219–2226, 2011.

[108] J. F. Baytos, *LASL explosive property data*. Univ of California Press, 1980, vol. 4.

[109] K. S. Vandersall, C. M. Tarver, F. Garcia, and S. K. Chidester, "On the low pressure shock initiation of octahydro-1, 3, 5, 7–tetranitro-1, 3, 5, 7-tetrazocine based plastic bonded explosives," *Journal of Applied Physics*, vol. 107, no. 9, p. 094 906, 2010.

[110] P. A. Urtiew, J. W. Forbes, C. M. Tarver, K. S. Vandersall, F. Garcia, D. W. Greenwood, P. C. Hsu, and J. L. Maienschein, "Shock sensitivity of lx-04 containing delta phase hmx at elevated temperatures," in *AIP Conference Proceedings*, AIP, vol. 706, 2004, pp. 1053–1056.

[111] N. Cummock, A. Casey, G. Montoya, and S. Son, "Shock sensitivity of energetic materials–-gathering additional information from the gap test," in *SHOCK19*, Shock Compression of Condensed Matter, 921 SW 6th Avenue, Portland, OR 97204 USA, Jun. 2019.

[112] J. Dick, "Measurement of the shock initiation sensitivity of low density HMX," *Combustion and Flame*, vol. 54, no. 1-3, pp. 121–129, 1983.

[113] J. Dick, "Stress-time profiles in low density HMX," *Combustion and flame*, vol. 69, no. 3, pp. 257–262, 1987.

[114] J. Dick and R. Engelke, "Reproducibility of planewave transit times in three explosives during initiation: Comparison to wedge experiments," *Propellants, Explosives, Pyrotechnics*, vol. 5, no. 5, pp. 139–144, 1980.

[115] S. Jacobs, T. Liddiard Jr, and B. Drimmer, "The shock-to-detonation transition in solid explosives," in *Symposium (International) on Combustion*, Elsevier, vol. 9, 1963, pp. 517–529.

[116] J. Dick, "Buildup to detonation in solid high explosives during plane shock initiation: Some comparisons," in *Symposium (International) on Combustion*, Elsevier, vol. 18, 1981, pp. 1623–1629.

[117] J. M. McGlaun, S. Thompson, and M. Elrick, "CTH: A three-dimensional shock wave physics code," *International Journal of Impact Engineering*, vol. 10, no. 1-4, pp. 351–360, 1990.

[118] D. E. Kittell, N. R. Cummock, and S. F. Son, "Reactive flow modeling of small scale detonation failure experiments for a baseline non-ideal explosive," *Journal of Applied Physics*, vol. 120, no. 6, p. 064 901, 2016.

[119] C. R. Siviour and J. L. Jordan, "High strain rate mechanics of polymers: A review," *Journal of Dynamic Behavior of Materials*, vol. 2, no. 1, pp. 15–32, 2016.

[120] B. Jensen, D. Holtkamp, P. Rigg, and D. Dolan, "Accuracy limits and window corrections for photon Doppler velocimetry," *Journal of applied physics*, vol. 101, no. 1, p. 013 523, 2007.

[121] P. Virtanen, R. Gommers, T. E. Oliphant, M. Haberland, T. Reddy, D. Cournapeau, E. Burovski, P. Peterson, W. Weckesser, J. Bright, S. J. van der Walt, M. Brett, J. Wilson, K. J. Millman, N. Mayorov, A. R. J. Nelson, E. Jones, R. Kern, E. Larson, C. J. Carey, İ. Polat, Y. Feng, E. W. Moore, J. VanderPlas, D. Laxalde, J. Perktold, R. Cimrman, I. Henriksen, E. A. Quintero, C. R. Harris, A. M. Archibald, A. H. Ribeiro, F. Pedregosa, P. van Mulbregt, and SciPy 1.0 Contributors, "SciPy 1.0: Fundamental Algorithms for Scientific Computing in Python," *Nature Methods*, vol. 17, pp. 261–272, 2020. DOI: 10.1038/s41592-019-0686-2.

[122] G. Van Rossum and F. L. Drake Jr, *Python tutorial*. Centrum voor Wiskunde en Informatica Amsterdam, The Netherlands, 1995.

[123] S. P. Marsh, *LASL shock Hugoniot data*. Univ of California Press, 1980, vol. 5.

[124] D. M. Dattelbaum, S. A. Sheffield, D. B. Stahl, A. M. Dattelbaum, W. Trott, and R. Engelke, "Influence of hot spot features on the initiation characteristics of heterogeneous nitromethane," in *Fourteenth Symposium (International) on Detonation*, 2010, pp. 611–621.

[125] H. Berghout, S. Son, C. Skidmore, D. Idar, and B. Asay, "Combustion of damaged PBX-9501 explosive," *Thermochimica Acta*, vol. 384, no. 1-2, pp. 261–277, 2002.

[126] J. F. Baytos, *LASL explosive property data*. Univ of California Press, 1980, vol. 4.

[127] B. Henson, L. Smilowitz, B. Asay, and P. Dickson, "The β–δ phase transition in the energetic nitramine octahydro-1, 3, 5, 7-tetranitro-1, 3, 5, 7-tetrazocine: Thermodynamics," *The Journal of chemical physics*, vol. 117, no. 8, pp. 3780–3788, 2002.

[128] L. Smilowitz, B. Henson, B. Asay, and P. Dickson, "The β–δ phase transition in the energetic nitramine-octahydro-1, 3, 5, 7-tetranitro-1, 3, 5, 7-tetrazocine: Kinetics," *The Journal of chemical physics*, vol. 117, no. 8, pp. 3789–3798, 2002, See section II.B.

[129] Z. Roberts, J. Mares, J. Miller, I. Gunduz, S. Son, and J. Rhoads, "Phase changes in embedded hmx in response to periodic mechanical excitation," in *Challenges in Mechanics of Time Dependent Materials, Volume 2*, Springer, 2017, pp. 79–86.

[130] D. Idar, D. Thompson, G. Gray Iii, W. Blumenthal, C. Cady, P. Peterson, E. Roemer, W. Wright, and B. Jacquez, "Influence of polymer molecular weight, temperature, and strain rate on the mechanical properties of pbx 9501," in *Aip conference proceedings*, AIP, vol. 620, 2002, pp. 821–824.

[131] E. Van de Casteele, D. Van Dyck, J. Sijbers, and E. Raman, "A model-based correction method for beam hardening artefacts in x-ray microtomography," *Journal of X-ray Science and Technology*, vol. 12, no. 1, pp. 43–57, 2004.

[132] R. J. Jennings, "A method for comparing beam-hardening filter materials for diagnostic radiology," *Medical physics*, vol. 15, no. 4, pp. 588–599, 1988.

[133] P. Jin, C. A. Bouman, and K. D. Sauer, "A method for simultaneous image reconstruction and beam hardening correction," in *Nuclear Science Symposium and Medical Imaging Conference (NSS/MIC), 2013 IEEE*, IEEE, 2013, pp. 1–5.

[134] N. Cummock, C. Rumchik, and S. Son, "Characterization of thermally and mechanically insulted pbx 9501 using micro-computed tomography," in *Proc. of the 16th Intl. Detonation Symp.*, 2018.

[135] J. Cutting, C. Chow, H. Chau, R. Hodgin, and R. Lee, "A small-scale safety test for initiation components," Lawrence Livermore National Lab., CA (US), Tech. Rep., 2002.

[136] J. F. Baytos, *LASL explosive property data*. Univ of California Press, 1980, vol. 4.

A. METHODOLOGY FOR HEATING PBX 9501 PELLETS TO INDUCE A β to δ-PHASE CHANGE

In the interest of minimizing effects due to temperature gradients and other potential sources, the methodology for inducing a phase change in the HMX crystals within a PBX 9501 pellet is explored.

A.1 Background

Many reports studying the polymorphic phases of HMX either do not detail the exact method of heating or heating rates used to induce the β–δ transition [29], or used heating rates of 2 K/min [34] or ∼5 K/min [8], [14], [28], [30].

Smilowitz et al. [14] perform heating experiments on 4 x 4 x 1 mm PBX 9501 pellets where the Second Harmonic Generation (SHG) is used to monitor the volume fraction of δ-phase HMX in the pellet (See Fig. A.1). Additionally, it is noted in two reports [14], [28] that radial gradients across a 4 x 4 x 1 mm (as shown in Fig. A.1) of less than 0.5 K can be maintained using heating rates of 4.8 K/min, while stressing that the kinetics have extreme sensitivity to temperature, thus temperature uniformity is essential.

Effects of heating rates between 0.2 and 10 K/min on the time to transition and temperature of transition are studied by Smilowitz et al. [33] and it is found that at 0.2 K/min, onset of phase transition from β to δ begins at ∼160.5 °C, and it is noted that faster ramp rates yield sharper Differential Scanning Calorimetry (DSC) peaks, but the total endothermicity integrated under the curve is independent of the ramp rate.

A.2 Methodology

In an effort to thermally induce a β–δ-phase transition in the HMX contained in PBX 9501 pellets, and damage inducing thermal stresses, samples are placed in a thin aluminum pan which are placed in a rack in a convection oven (see Fig. A.3 and A.4). Examples of a larger sample geometry pre- and post-heating is shown in Fig. A.5 and A.6.

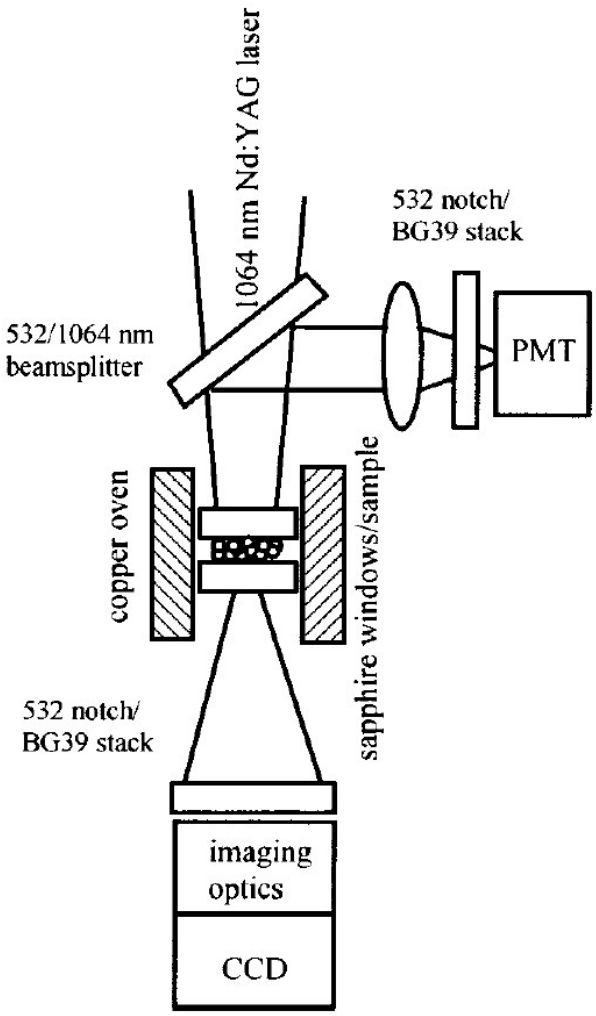

Figure A.1. Apparatus diagram of the SHG experiments. PMT and CCD stand for PhotoMultiplier Tube and Charge Coupled Device light detectors, respectively. 532 notch/BG39 denotes a notch filter centered at 532±2 nm and 5 mm of Schott glass BG39 short pass filters, respectively. The imaging size on the sample was approximately 5 mm in diameter. Laser intensity and typical integration and imaging times are discussed in [14]. Diagram reproduced from [14].

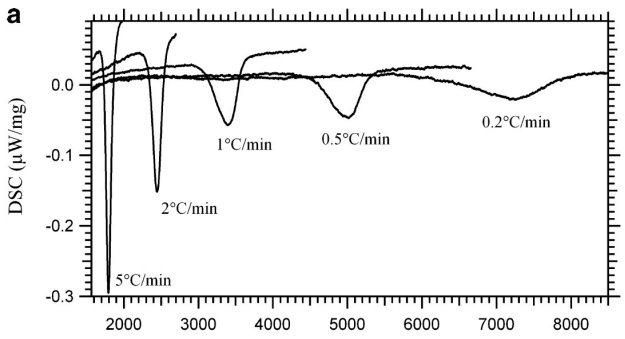

Figure A.2. Time dependence of β–δ HMX transition on the DSC ramp rate. Reproduced from [33].

Figure A.3. Aluminum pan with 3 x 1 mm PBX 9501 pellet placed in the center of a weight (used to keep the light-weight pan & pellet from moving due to convection currents within the oven).

Figure A.4. Programmable convection oven with samples placed inside.

Figure A.5. An example of a 6 x 6 mm PBX 9501 pellet with no heat treatment.

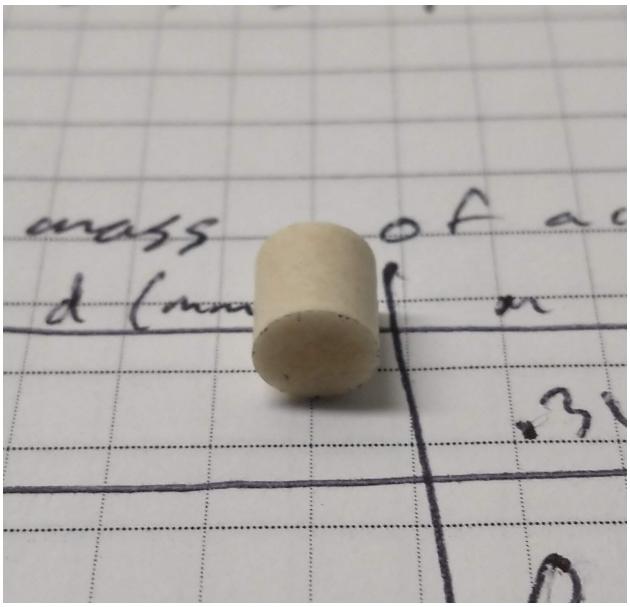

Figure A.6. An example of a 6 x 6 mm PBX 9501 pellet after heat treatment at 180 °C for one hour with a 0.7 K/min heat ramp.

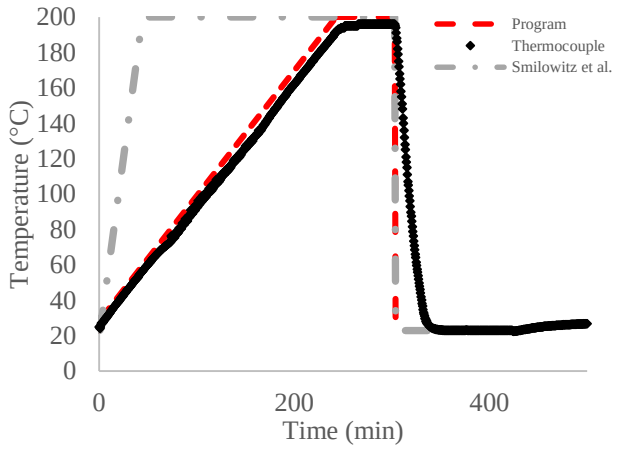

Figure A.7. An example of a sample set heating of PBX 9501 pellets, where a programmable convection oven was used to induce thermal insult. The programmed temperature is shown, along with a thermal couple placed in the oven near one of the samples under treatment. Additionally, the grey dotted line shows the maximum heating rate used by Smilowitz et al. [14], [28], where monitored temperature gradients within 4 x 4 x 1 pellets were observed to be less than 0.5 K.

In comparing heating rates to those used to induce a phase transition from β to δ in previous works, a conservative rate of 0.7 K/min was chosen for my samples, a heating rate nearly seven times slower than that suggested by Smilowitz et al. for samples of a similar size [14], [28] (see Fig. A.7). Of note is a model created by Smilowitz and Henson for half transition versus heating rate, shown in Fig. A.8.

A.3 Ramping effects

Something to be concerned with when inducing very slow heating rates is the increased energy input to the sample via the long period of time that the sample is exposed to high temperatures. Sample decomposition rates increase with temperature, and as such, significant amounts of material would be lost with extremely low heating rates. This could be mitigated by introducing a number of step functions with different heating rates starting at room temperature. Further examination of the effects of this sort of exposure on the physical structure of the HMX crystals is needed.

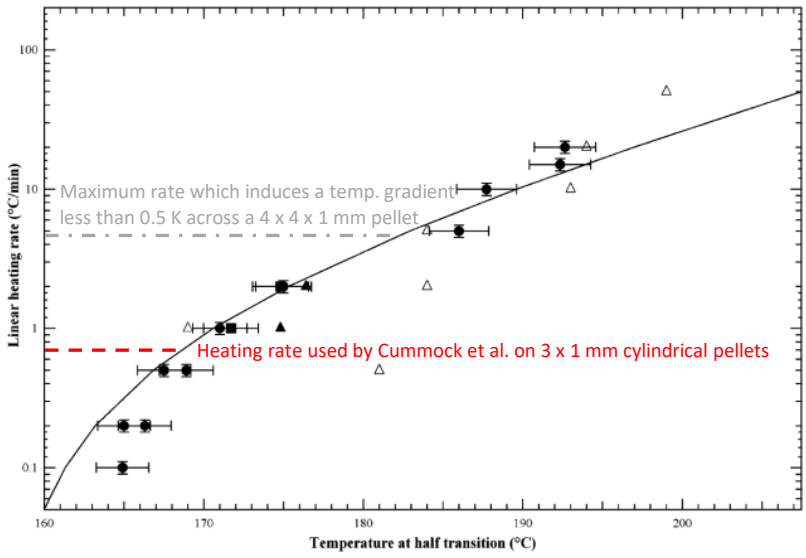

Figure A.8. Model curve of half transition temperature versus heating rate, reproduced from [33].

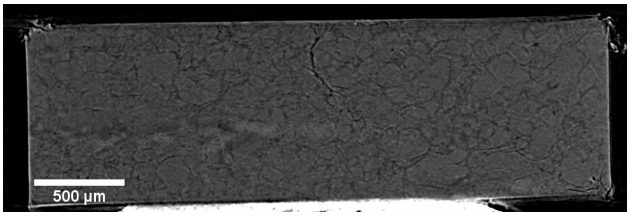

Figure A.9. Reconstruction of the cross-section of a pristine pellet

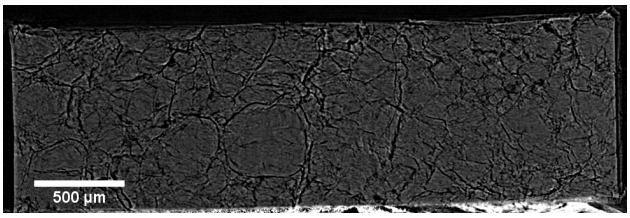

Figure A.10. Reconstruction of the cross-section of a thermally insulted pellet

A.4 Micro-CT Analysis

Two pellets were analyzed via micro-Computed Tomography (μCT), where one was pristine, and the other had been thermally insulted via the program/thermocouple heating profile shown in Fig. A.7. A reconstructed image of each is shown in Fig. A.9 and A.10.

Porosity analysis was performed using both CTAn, provided with the Skyscan software package, and with a microstructural analysis tool developed at AFRL by Jesus Mares, here labelled as 'Mares'. A key difference between the two techniques is that Mares allows for dynamic thresholding; i.e., each cross-sectional image is analyzed with a threshold specific to it, where an algorithm is used to determine the optimal threshold. CTAn, on the otherhand, uses a static user chosen threshold, where one must make a judgement on the optimal threshold value for the entire dataset, and then apply it to all cross-sectional images under analysis.

The results of the analysis are shown in Fig. A.11, where the porosity in each cross-sectional image is analyzed from the bottom face of the pellet to its top (dynamic face), yielding porosity vs. pellet depth. Additionally, the chosen thresholds are shown in Fig. A.12, where the thresholds chosen with CTAn are simply horizontal lines at the value 22.

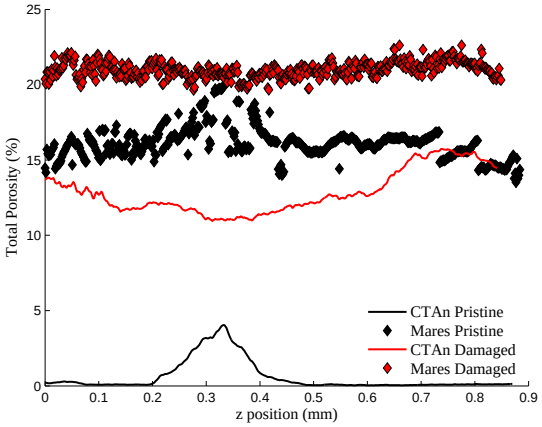

Figure A.11. Porosity with pellet depth as analyzed by CTAn and Mares.

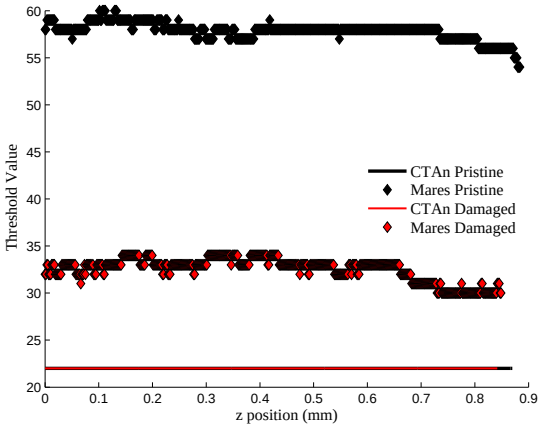

Figure A.12. Threshold values chosen for each analysis.

Note that the dataset for the pristine pellet had a significant artifact between z-positions 0.2 and 0.5 mm, where a spike appears in the porosity results. Outside of this artifact, the porosity appears to be quite constant throughout the pellet, with the exception of some effects near the faces of the pellets.

B. CHARACTERIZATION OF THERMALLY AND MECHANICALLY INSULTED PBX 9501 USING MICRO-COMPUTED TOMOGRAPHY

Initiation thresholds for HMX have been shown to depend on particle size, suggesting that understanding the microstructure of explosives may be important for predicting their initiation behavior. In this work, six samples of PBX 9501 are produced, four of which undergo thermal insult in an attempt to incur β–δ-phase transition in the HMX constituent, and one is mechanically insulted via quasi-static compression. X-ray Computed Tomography (XCT) is used to observe features within each sample. The change in porosity is quantified axially through the sample, and regions of highest porosity in thermally insulted samples appear where temperature gradients were likely large relative to other areas of the sample. The XCT results show the mechanically insulted sample having the highest porosity nearest the interface of the sample and the moving surface of the hydraulic press during quasi-static compression.

B.1 Background

Thermal or mechanical energy input which does not induce initiation in an explosive charge can result in deformation or damage, which may have an effect on its initiation behavior. This change is of interest regarding the intentional initiation as well as safe transportation of munitions.

Thermal insult and insult from quasi-static compression have been shown to change the combustion behavior of PBX 9501 by Berghout et al. [125], likely due to the microstructural changes that were produced. The microstructural changes observed [125] may be due to a β–δ-phase transition which produces a volume change in the HMX crystals [126]–[128]. In the case of thermal insult, it is possible that small HMX crystals are dissolved in the plasticizer during heating [125], exacerbating the structural change in the sample. Further characterization of the microstructure of damaged explosive charges, in comparison with that of pristine explosive charges, is necessary to develop a relationship between shock sensitivity and damage in explosives. It is therefore proposed that the microstructure of explosive

charges which have been subjected to thermal or mechanical insult be characterized using a non-destructive method, such as X-ray Computed Tomography (XCT); in this manner, well-characterized samples can subsequently undergo shock sensitivity or initiation threshold testing. This work is dedicated to beginning the microstructural characterization process of PBX 9501.

B.2 Experimental Methods

Five samples of PBX 9501 were produced and subsequently thermally or mechanically insulted, then scanned using XCT. Additionally, one pristine sample of PBX 9501 was produced and scanned using the same techniques to observe and quantify differences between pristine, thermally insulted, and mechanically insulted samples.

B.2.1 Sample Production

Cylindrical pellets were produced by axially pressing PBX 9501 into a die at 345 MPa and holding pressure for one minute each, resulting in pellets at 97% of Theoretical Maximum Density (TMD) [126], each with a 6.04 mm diameter and an aspect ratio of approximately 1.1. One of the six samples produced was chosen as a control, another sample was chosen to undergo quasi-static compression as mechanical insult, and the remaining samples were set aside to undergo varying levels of thermal insult via a natural convection oven.

B.2.2 Thermal Insult

Phase transition of HMX from β to δ has been observed and documented in numerous works [125], [127]–[129]. In an attempt to induce the β–δ-phase transition, four samples were heated in an oven which was pre-heated to 160–200 °C for 30–70 minutes at atmospheric pressure, then removed from the oven and allowed to cool at room temperature. The heating procedure was as follows: (1) pre-heated the oven to a select temperature and allowed approximately two hours to reach uniform equilibrium, then (2) placed the sample on an aluminum holding plate, both at room temperature, in the oven, then (3) allowed heating via natural convection for the selected test duration (see Table B.1), and (4) removed the

Table B.1. Heated PBX 9501 samples.

Samp. name	Mass (g)	Heating dur. (min.)	Heating temp. (°C)
S-H1	0.358	30	165
S-H2	0.354	30	175
S-H3	0.351	70	180
S-H4	0.355	35	200

Figure B.1. S-H3 after heating heating and cooling. No surface cracking was apparent immediately after removal from the oven, however, some surface cracking appeared approximately 24 hours after cooling to room temperature.

sample from the oven and allowed it to cool at room temperature for at least 24 hours before scanning.

Optical images of these samples were taken after heating; S-H1 and S-H2 (see Table B.1) showed no optically observable changes on the outer surface, while S-H3 (Fig. B.1) and S-H4 (Fig. B.2) underwent discoloration and surface cracking. A z-axis was defined for the heated samples such the surface that was not interfacing with the aluminum holding plate during heating, was $z = 0$. It is noted that the surface cracking observed in S-H4 occured near the interface between the aluminum holding plate and the sample (nearest $z = 6.35$ mm in Fig. B.2), indicating that the relatively high thermal conductivity of the aluminum plate may have caused a significant axial temperature gradient near the sample's surface.

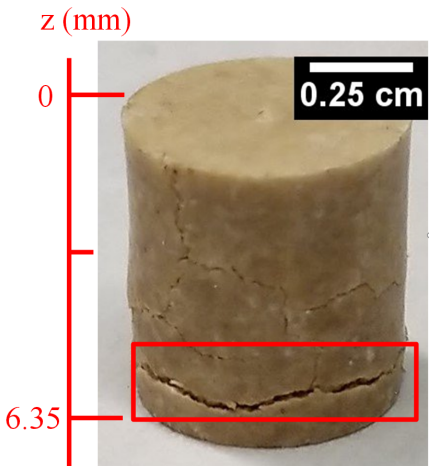

Figure B.2. S-H4 after heating and cooling. Discoloration and surface cracking developed during the heating process, where the most noticeable crack appeared nearest the interface between the aluminum holding plate and the sample.

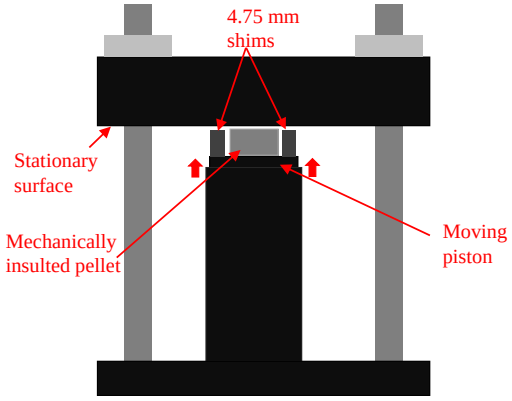

Figure B.3. Schematic showing mechanical insult of a PBX-9501 sample, S-C1.

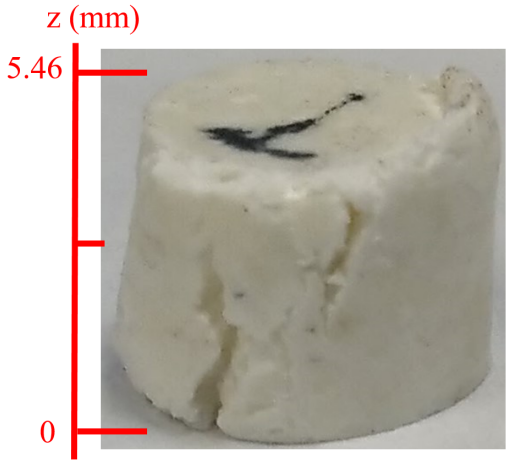

Figure B.4. S-C1 after unconfined axial compression to 25% engineering strain.

B.2.3 Mechanical Insult

The same hydraulic press used to produce the six PBX 9501 pellets was then used to quasi-statically compress one sample, here named S-C1, to a 4.75 mm shim, as shown in Fig. B.3, resulting in 25% axial engineering strain. During compression, the sample was unconfined on the sides, and 25% strain was held for one minute before releasing, where it was observed that significant plastic deformation had occurred (see Fig. B.4); spring-back to 5.46 mm was observed after release. The mark on the top face of the sample in Fig. B.4 represents the face of the pellet which was pressed against the stationary press surface during the mechanical insult process; its opposite surface was defined as $z = 0$.

B.2.4 Sample imaging

Sample imaging was performed with a Bruker SkyScan 1272 with a 16 Mp X-ray detector. The samples were scanned with 2.2–2.5 μm/pixel resolution with an accelerating voltage of 70–80 kV and no filter, as is detailed in Table B.2.

B.3 Analysis

Radiograph data from scans were reconstructed into sample cross-sectional images using NRecon and InstaRecon, software provided with the SkyScan 1272. These programs allow manual and automatic adjustments to be made during digital reconstruction to mitigate acquisition errors from ring artifacts, beam-hardening, and misalignment. The reconstructed 'slices', were then analyzed using CTAn, provided by Bruker. In the case of the pristine pellet (S-Prist), it was apparent that the scanning resolution (2.5 μm/pixel) was not sufficient to detect features such as distinct particles or pores within the sample (see Fig. B.5). Samples which underwent thermal cycling or unconfined mechanical compression, however, yielded images with increased void sizes which were easily resolved; images of thermally and mechanically insulted samples were binarized by choosing a lower threshold bit depth value, where any pixels below the chosen threshold value become 'void space' (black), and pixels larger than or equal to the threshold value become 'objects' (white). An example monochromatic image of a thermally insulted sample is shown in Fig. B.6, where it is apparent that voids are distinguishable and distinct; however, particles appear coalesced in the binarized image, rendering particle analysis unreliable.

Here, it is assumed that 'void-space' includes only air in each pressed sample, where HMX particles and the binder constituents [125], [130] of PBX 9501 are considered objects. This assumption was made based on there being no distinguishable 'void-space' in the pristine PBX sample; however, it is possible that the resolution simply was not sufficient to show the spaces between HMX particles which were undisturbed by the input.

Table B.2. X-ray CT scanning parameters used with the samples in this study.

Sample name	**Insult type**	**Scanning resolution (μm/pix)**	**Source voltage (kV)**	**Source power (W)**
S-Prist	None	2.50	75	8.3
S-H1	Thermal	2.20	80	10
S-H2	Thermal	2.20	70	8.8
S-H3	Thermal	2.50	75	8.3
S-H4	Thermal	2.50	75	8.8
S-C1	Mechanical	2.25	85	8.5

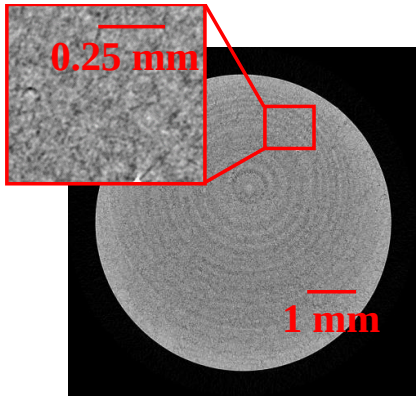

Figure B.5. Reconstructed XCT image showing a cross-section of pristine PBX 9501. The inset of this figure shows the low signal to noise ratio obtained after post-processing.

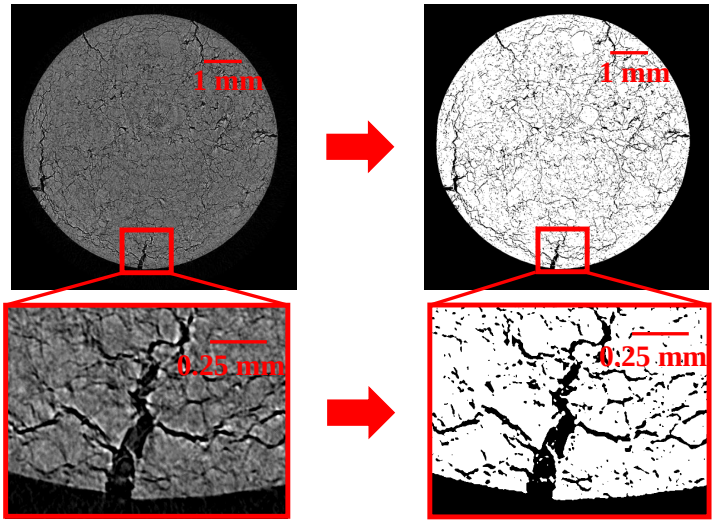

Figure B.6. Sample S-H4 reconstruction before binarization (left) and after binarization (right). Highly disturbed areas result in resolvable voids, however, many particle-particle interfaces are not resolved.

B.4 Results

After binarization of the XCT datasets obtained for the six samples in this work, it appeared that particle analysis would not be feasible at the resolution used; additional scans are necessary to determine what level of resolution is necessary to distinguish particles which have undisturbed interfaces with like particles. Large pores and cracks were observed in all thermally and mechanically insulted samples, where scans of the pristine sample showed very little ($<<$ 1%) total porosity, including open and closed pores. Approximately three percent porosity is expected in the pristine sample; enhanced resolution scans would likely yield a more accurate representation of the pristine sample porosity. The XCT images of S-Prist indicate an upper limit on the resolution of approximately 2.5 μm/pixel; i.e., resolution enhancement is necessary to distinguish distinct particles and pores in a pristine PBX 9501 sample pressed to 97% TMD. Increased resolution can generally be achieved with the trade-off of increased scan duration; the CT scanner used in this work has a maximum achievable resolution of 350 nm/pixel, though this limitation is not inherent to the method.

Figure B.7 shows selected cross-sections of each heated sample shown in Table B.1. The interfaces between particles are much more distinct in S-H3 and S-H4 [Fig. B.7 (C) & (D)] than those of S-H1 and S-H2 [Fig. B.7 (A) & (B)]. Additionally, beam hardening appears to have been especially significant in S-H1 and S-H2, exhibited by the spatially non-uniform profile where pixels appear brighter nearest the edge of the sample. This effect could likely be mitigated by using a lower accelerating voltage during scanning, in combination with a thin copper or aluminum plate as a filter [131], [132]; post-processing techniques can also be used to reduce beam-hardening that was not sufficiently mitigated during a scan [131], [133].

Due to the aforementioned problems in images from samples S-H1 and S-H2, binarization of the reconstructed images of these samples yielded inaccurate representations of porosity within the sample; therefore, quantitative analysis of these sample results were omitted. When comparing Fig. B.7 (A) & (B) with Fig. B.5, it is qualitatively clear that the level of heating imposed on S-H1 and S-H2 had some effect on the samples, though this was not apparent with the naked eye.

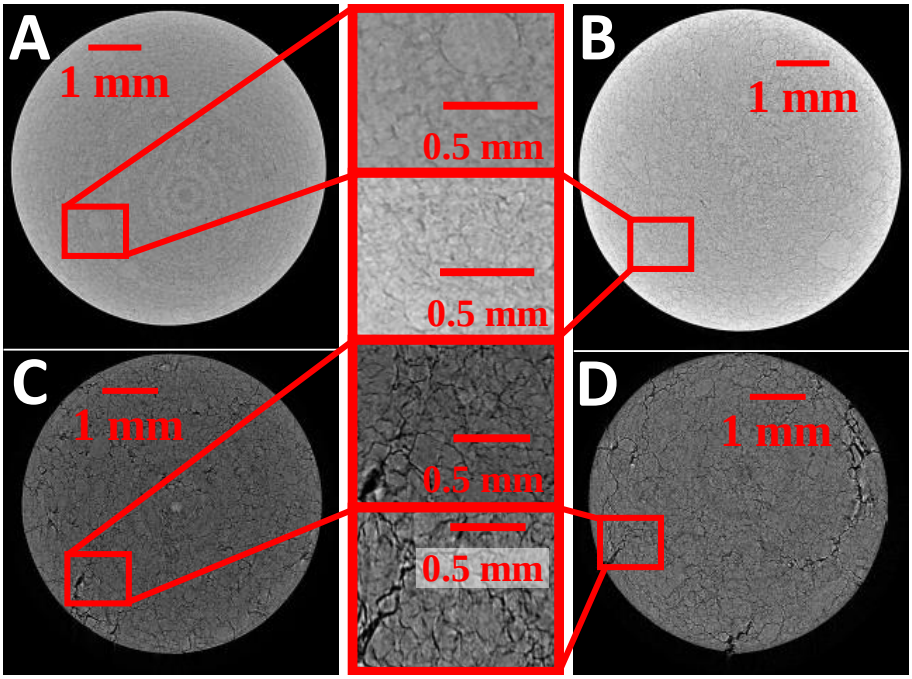

Figure B.7. Select cross-sectional images of S-H1 (A), S-H2 (B), S-H3 (C), and S-H4 (D). See Table B.1 for thermal input details.

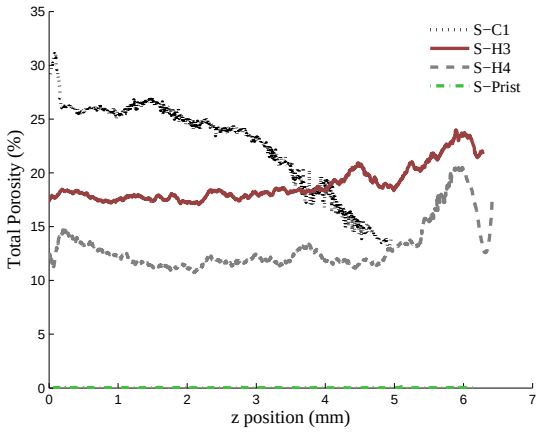

Figure B.8. Porosity of select samples, calculated from the XCT images using CTAn.

There was sufficient contrast in samples S-H3 and S-H4 such that binarization resulted in an accurate representation of the void space in these samples, allowing porosity analysis (see Fig. B.8). Porosity in these results should be interpreted as 'added porosity'; i.e., since void space in S-Prist could not be resolved (hence the porosity of S-Prist in Fig. B.8 being approximately constant near zero), it may be assumed that the void space that is resolved in the thermally and mechanically insulted samples resulted from the input. It is notable that a significant rise in porosity occurs closest to the surface of the sample which interfaced with the aluminum holding plate (compare Fig. B.2 and B.8), indicating that thermal insult was most significant nearest the holding plate, likely due to the high thermal conductivity of the aluminum allowing a larger temperature gradient on the plate side of the sample.

Additional experiments are needed to determine the mechanisms involved in producing additional pore space in the samples; it is likely, however, that the driving mechanisms between S-H1 and S-H2 are different than those of S-H3 and S-H4. A phase change from β to δ is expected in HMX at temperatures as low as 160 °C, given enough time [128]. If an HMX crystal is converted in its entirety from β-phase to δ-phase, a 6.7% volume increase is expected [127]. Additionally, significant decomposition of the HMX is likely in the samples with greater thermal energy input (S-H3 and S-H4). Decomposition of the components in the PBX 9501 binder (estane and plasticizer BDNPA-F) are also potential damage mechanisms. It has also been shown that fine HMX crystals may be dissolved by the

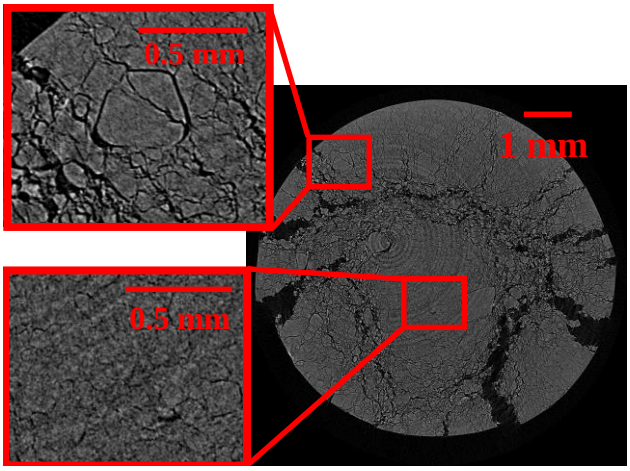

Figure B.9. Select cross-sectional XCT image of sample S-C1 (see Table B.2) after mechanical insult, showing highly disturbed areas near shear bands, and relatively undisturbed areas.

PBX 9501 plasticizer and subsequently recrystallized onto larger HMX crystals at elevated temperatures in a process known as Ostwald ripening [125]. Enhanced resolution XCT scans would be necessary to observe this phenomenon, since the results in this work do not allow visualization of undisturbed particle-particle interfaces, rather a view of 'added porosity' only, is seen.

While samples which underwent thermal insult showed 'added porosity' which was somewhat randomly distributed throughout the sample, the reconstructed XCT images of the mechanically insulted sample (S-C1) showed distinct shear bands with largely open porosity (i.e., cracks/pores which reached the outer edge of the sample), as shown in Fig. B.9; these approximately 45° shear bands (see Fig. B.10) are typical of compression tests. Sites in S-C1 which were not near the shear bands appeared relatively undisturbed, to the point where pores at these sites were not resolvable using scanning parameters shown in Table B.2, and these areas looked much like the results of S-Prist. The porosity along the z-axis of S-C1 is largest at $z = 0$, which represents the surface closest to the moving piston during mechanical insult (see Fig. B.3); porosity stays relatively constant at 25% after a very rapid decrease from 32%, and decreases linearly from 2.75 mm to the top surface of the sample.

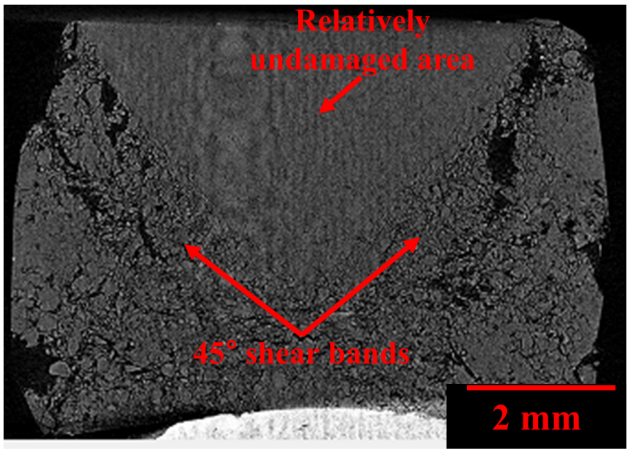

Figure B.10. Select axial cross-sectional XCT image of sample S-C1, where shear bands, typical of compression tests, are noted.

B.5 Conclusions

Images of six PBX 9501 samples are obtained using X-ray micro Computed Tomography (XCT), where one sample is undisturbed, i.e., pristine, four samples were subjected to thermal insult under various conditions, and one sample was mechanically insulted via quasi-static compression. It was apparent from the reconstructed XCT images that the scanning parameters such as pixel size, source voltage, and lack of a filter, did not allow for individual features in the pristine sample to be observed.

All heated samples had qualitative differences from the pristine sample, however, only the two samples with the largest thermal energy input had porosity which was able to be accurately represented by a binarized image. In the binarized images, particles tended to coalesce, so particle analysis was not feasible, rather porosity throughout the sample was quantified. A significant increase in porosity occurred near the sample surface which was resting on an aluminum holding plate during thermal insult, likely indicating that the largest temperature gradient occurred there due to the thermal conductivity of the plate.

The mechanically insulted sample XCT images showed distinct shear bands within the pellet, as opposed to the thermally insulted samples which exhibited added porosity which was randomly distributed spatially throughout the samples. The change in porosity along the axial direction of the mechanically insulted sample was plotted, and porosity was seen to decrease as the sample surface which interfaced with the stationary press surface during quasi-static compression was approached, i.e., the highest porosity was nearest the moving hydraulic press interface with the sample.

Porosity may be an important metric in estimation of the shock sensitivity of PBX 9501, and XCT is a tool which may be used to determine details about the porosity throughout an entire sample non-destructively. However, some features, such as pores in a binderized composite pressed to 97% of its TMD may not be detectable using the scanning parameters of this study. Mechanically and thermally insulted samples exhibit resolvable porosity under these parameters. Future work using enhanced resolution is to be performed, in addition to experiments correlating quantified microstructural results with the material's shock sensitivity.

B.6 Publication disclosure

The majority of the work presented in this chapter was published in the proceedings of the 16th International Detonation Symposium [134].

C. ESTIMATING THE INPUT PRESSURE AT AN HMX INTERFACE USING HUGONIOT MATCHING

Cutting et al. [135] shows particle velocity data in LiF at a PMMA/LiF interface, where the booster is Detasheet, and there is a 16 μm thick foil interface between the PMMA and LiF in order to have a reflective surface for velocimetry using a frequency doubled laser beam from a YAG laser.

Knowing these particle velocities in LiF shown in [135], we can estimate the particle velocities in the PMMA at the PMMA/LiF interface prior to crossing the interface using the Hugoniot data for PMMA and LiF found in [123], where the average ρ_0 for LiF is 2.638 g/cm^3. This can be done graphically by constructing the $P-u_p$ Hugoniots using the following steps:

1. draw the right-going $P-u_p$ Hugoniot for LiF, where $u_0 = 0$
2. draw the right-going $P-u_p$ Hugoniot for PMMA, where $u_0 = 0$
3. draw the left-going $P-u_p$ Hugoniot for PMMA, and slide it horizontally by varying u_0, recalling that $u_0 = 2u_1$, until its line intersects with u_2, the particle velocity measured in [135].
4. With the left-going Hugoniot of PMMA intersecting u_2, note the intersection with the right going Hugoniot of PMMA. This intersection represents u_1 and P_1, the particle velocity and pressure of the shock in the PMMA immediately prior to reaching the PMMA/LiF interface

The right-going Hugoniots are found by conservation of momentum:

$$P = \rho_0 u_p U_s \tag{C.1}$$

and the common empirical relationship for many materials between shock velocity and particle velocity

$$U_s = C_0 + s u_p \tag{C.2}$$

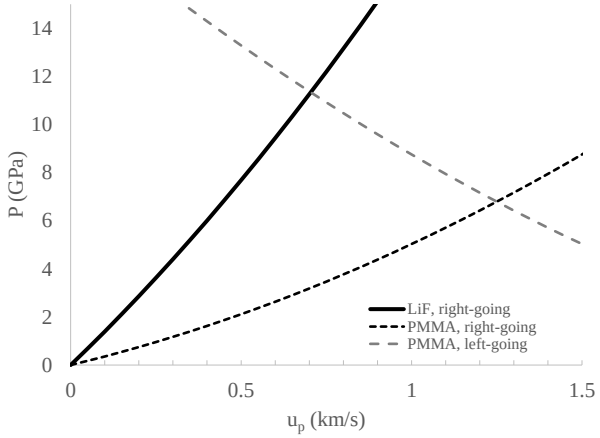

Figure C.1. An example of graphical shock matching using the $P - u_p$ Hugoniots of LiF and PMMA, where in the shown case, u_0 in the PMMA is 1.25 km/s, which is the result of a shock traveling at $U_s \approx 4.6$ km/s through the PMMA.

The left-going Hugoniot is found by

$$P = \rho_0 C_0 (2u_0 - u_p) + \rho_0 s (2u_0 - u_p)^2 \tag{C.3}$$

Of course, P is the vertical axis, and u_p is the horizontal axis in a $P - u_p$ Hugoniot, and u_0 represents the particle velocity of the first material through which the shock is traveling prior to meeting the interface. An example of the graphical shock matching method is shown in Fig. C.1, where the left-going Hugoniot for PMMA has been adjusted to intersect the right-going Hugoniot in LiF at $u_p = 0.7$ km/s, the highest particle velocity measured by Cutting et al. [135].

Additionally, one could solve for u_0 by equating the right-going Hugoniot for LiF and the left-going Hugoniot for PMMA:

$$u_0 = \frac{2 s_A u_2 \rho_{0,A} - C_{0,A}\rho_{0,A}}{4 s_A \rho_{0,A}} \pm \frac{\sqrt{\rho_{0,A}\left(4 C_{0,B} s_A u_2 \rho_{0,B} + 4 s_B s_A u_2^2 \rho_{0,B} + C_{0,A}^2 \rho_{0,A}\right)}}{4 s_A \rho_{0,A}} \tag{C.4}$$

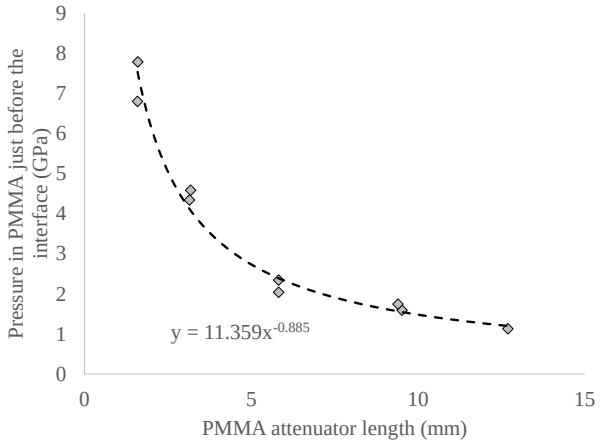

Figure C.2. Pressure in PMMA with length before a material interface. This is based on data shown in results by Cutting et al. [135].

where material A is the first material through which the shock is travelling (the PMMA in this case), and material B interfaces with material A and receives the shock, resulting in a P_2 and u_2 at the interface. Performing this calculation at all the particle velocities measured by Cutting et al. [135] yields Fig. C.2.

Now that we know the pressure in the PMMA with its length, we can find the pressures that would result at a PMMA/HMX interface, where the HMX is low density. This requires using P-ν Hugoniot results from the work of J.J. Dick [112]. Once we have an estimate of the pressures resulting at this interface, we can choose two attenuator lengths that yield significantly different pressures at this interface, but that are low enough to result in a run-to-detonation distance greater than 3 mm, the length of the HMX sample. Failure to reach a complete detonation is desired because the particle velocity is capped once detonation is achieved.

When estimating the pressure at the interface of the PMMA one may solve for u_2 in Eq. C.4:

$$\begin{aligned} u_2 = & \frac{1}{2s_A\rho_{0,A} - 2s_B\rho_{0,B}} \Big\{ C_{0,A}\rho_{0,A} + 4s_A u_0 \rho_{0,A} + C_{0,B}\rho_{0,B} - \\ & \Big[C_{0,A}^2\rho_{0,A}^2 + 2C_{0,A}(C_{0,B} + 4s_B u_0)\rho_{0,A}\rho_{0,B} + \\ & \rho_{0,B}(8C_{0,B}s_A u_0 \rho_{0,A} + 16 s_A s_B u_0^2 \rho_{0,A} + C_{0,B}^2 \rho_{0,B}) \Big]^{1/2} \Big\} \end{aligned} \tag{C.5}$$

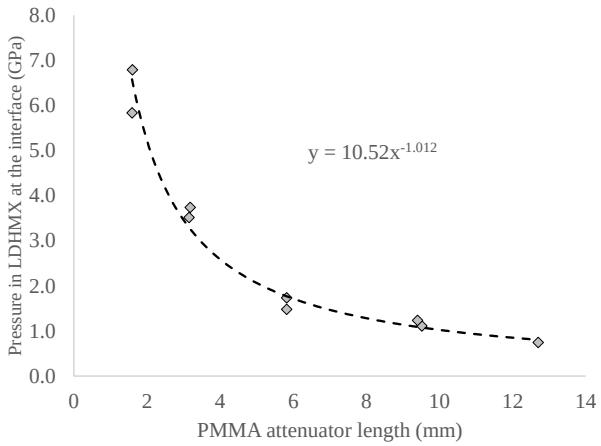

Figure C.3. Shock pressure at a PMMA/LDHMX interface, assuming no radial rarefaction wave affects the shock.

The pressure at the interface of PMMA and low density HMX (LDHMX; $\rho_0 = 1.24$ g/cm^3) is shown as a function of PMMA length in Fig. C.3, where the calculations were made based off of data from Cutting et al. [135] and shock Hugoniot parameters for LiF, PMMA, and LDHMX [113], [136].

D. THE FISHER INFORMATION

A summary of the expectations of the partial derivatives of the log-likelihood of various distribution functions.

D.1 General definitions

Define the log-likelihood as:

$$\begin{aligned} l &= \log(L) \\ &= \sum_{\mathrm{i}-1}^{n} \left[\log \binom{N_{\mathrm{i}} + M_{\mathrm{i}}}{N_{\mathrm{i}}} + N_{\mathrm{i}} \log(F_{\mathrm{i}}) + M_{\mathrm{i}} \log(Q_{\mathrm{i}}) \right], \end{aligned} \tag{D.1}$$

where L is the likelihood function. For simplicity of display, the binomial term and the summation in Eq. D.1 will be ignored from here on, noting that the binomial term will vanish with derivatives taken and that the summation will be easily and intuitively appended onto the functional forms displayed below. Additionally, the subscript 'i's are neglected below, again for simplicity.

$$Q = 1 - F,$$

and

$$z = \frac{x - \mu}{\sigma}$$

D.2 Normal distribution

Defining F as the normal Cumulative Distribution Function (CDF),

$$F(x; z) = \int_{-\infty}^{z} \frac{1}{2\pi} \exp\left[-z^2/2\right], \tag{D.2}$$

where μ is the mean of the distribution, and σ is the standard deviation.

For the purpose of calculating Maximum Likelihood Estimates (MLEs),

$$\frac{\mathrm{d}l}{\mathrm{d}\mu} = \frac{(x - \mu)^0}{\sigma^1} a_{nor} \tag{D.3}$$

$$\frac{\mathrm{d}l}{\mathrm{d}\sigma} = \frac{(x-\mu)^1}{\sigma^2} a_{nor} \tag{D.4}$$

where

$$a_{nor} = \frac{\exp\left[-\frac{1}{2}z^2\right]}{2\pi}\left(\frac{M}{Q} - \frac{N}{P}\right)$$

The following expectations apply:

$$E\left[\frac{\mathrm{d}l}{\mathrm{d}\mu}\right] = 0; \quad E\left[\frac{\mathrm{d}l}{\mathrm{d}\sigma}\right] = 0$$

$$E\left[\frac{\partial^2 l}{\partial\mu^2}\right] = -\frac{(x-\mu)^0}{\sigma^2} A_{nor} \tag{D.5}$$

$$E\left[\frac{\partial^2 l}{\partial\mu\partial\sigma}\right] = -\frac{(x-\mu)^1}{\sigma^3} A_{nor} \tag{D.6}$$

$$E\left[\frac{\partial^2 l}{\partial\sigma^2}\right] = -\frac{(x-\mu)^2}{\sigma^4} A_{nor} \tag{D.7}$$

where

$$A_{nor} = \frac{N+M}{4\pi^2 FQ} \exp\left[-z^2\right]$$

D.3 Logistic distribution

Redefining F as the logistic CDF,

$$F(x;\mu,s) = \frac{1}{1+\exp\left[-\frac{x-\mu}{\sigma}\right]}, \tag{D.8}$$

Where μ is the mean, and σ is a scale parameter proportional to the standard deviation.

For the purpose of calculating MLEs,

$$\frac{\mathrm{d}l}{\mathrm{d}\mu} = \left(\frac{1}{\sigma}\right)^1 (x-\mu)^0 a_{lg} \tag{D.9}$$

$$\frac{\mathrm{d}l}{\mathrm{d}\sigma} = \left(\frac{1}{\sigma}\right)^2 (x-\mu)^1 a_{lg} \tag{D.10}$$

where

$$a_{lg} = F\left(M\frac{F}{Q} - N\right)\exp\left[-z\right]$$

The following expectations apply:

$$E\left[\frac{\mathrm{d}l}{\mathrm{d}\mu}\right] = 0; \quad E\left[\frac{\mathrm{d}l}{\mathrm{d}\sigma}\right] = 0$$

$$E\left[\frac{\partial^2 l}{\partial\mu^2}\right] = -z^0 A_{lg} \tag{D.11}$$

$$E\left[\frac{\partial^2 l}{\partial\mu\partial\sigma}\right] = -z^1 A_{lg} \tag{D.12}$$

$$E\left[\frac{\partial^2 l}{\partial\sigma^2}\right] = -z^2 A_{lg} \tag{D.13}$$

where

$$A_{lg} = \frac{F^3(N+M)}{Q\sigma^2}\exp\left[-2z\right]$$

D.4 Log-logistic distribution

Redefining F as the log-logistic CDF,

$$F(x;\alpha,\beta) = \frac{1}{1+(x/\alpha)^{-\beta}}, \tag{D.14}$$

where the parameter α is a scale parameter and is also the median of the distribution, and the parameter β is a shape parameter. Both parameters are constrained to be greater than zero.

For the purpose of calculating MLEs,

$$\frac{\mathrm{d}l}{\mathrm{d}\beta} = \left(-\frac{\beta}{\alpha}\right)^0 \log\left(\frac{x}{\alpha}\right)^1 a_{ll} \tag{D.15}$$

$$\frac{\mathrm{d}l}{\mathrm{d}\alpha} = \left(-\frac{\beta}{\alpha}\right)^1 \log\left(\frac{x}{\alpha}\right)^0 a_{ll} \tag{D.16}$$

where

$$a_{ll} = \left(\frac{x}{\alpha}\right)^{-\beta} \left(NF - M\frac{F^2}{Q}\right)$$

The following expectations apply:

$$E\left[\frac{\mathrm{d}l}{\mathrm{d}\beta}\right] = 0; \quad E\left[\frac{\mathrm{d}l}{\mathrm{d}\alpha}\right] = 0$$

$$E\left[\frac{\partial^2 l}{\partial \beta^2}\right] = -\left(-\frac{\beta}{\alpha}\right)^0 \left[\log\left(\frac{x}{\alpha}\right)\right]^2 A_{ll} \tag{D.17}$$

$$E\left[\frac{\partial^2 l}{\partial \beta \partial \alpha}\right] = -\left(-\frac{\beta}{\alpha}\right)^1 \left[\log\left(\frac{x}{\alpha}\right)\right]^1 A_{ll} \tag{D.18}$$

$$E\left[\frac{\partial^2 l}{\partial \alpha^2}\right] = -\left(-\frac{\beta}{\alpha}\right)^2 \left[\log\left(\frac{x}{\alpha}\right)\right]^0 A_{ll} \tag{D.19}$$

where

$$A_{ll} = \frac{(N+M)F^3}{Q}\left(\frac{x}{\alpha}\right)^{-2\beta}$$

VITA

Nicholas Robert Cummock was born in 1989 in California to parents Brad and Debra Cummock. He graduated from Bolton High School in 2007 while living in Bartlett, Tennessee. After spending a year as a valet at the Peabody hotel, he began a journey which lasted from August 2008 to August 2010 in Rio Grande do Sul, Brazil as a volunteer missionary for the Church of Jesus Christ of Latter-day Saints, where he acquired fluency in Brazilian Portuguese. Upon returning to the United States, he attended college at Brigham Young University–Idaho, where he met a girl who eventually became his wife, and earned a BS in Mechanical Engineering in 2014. He soon after enrolled at Purdue University and earned a MS in Mechanical Engineering under Professor Steven F. Son in 2017, performing work associated with the Awareness and Localization of Explosive Related Threats (ALERT) program, sponsored by the Department of Homeland Security (DHS). During this time he spent one summer as a graduate research assistant at Los Alamos National Laboratory (LANL) under Dr. Scott Jackson. He then continued under the same advisor performing research to earn his Ph.D. at Purdue University, with funding through the Science, Mathematics And Research for Transformation (SMART) Fellowship for Service Program; through this program he spent three summers at the Air Force Research Laboratory (AFRL) at Eglin Air Force Base (AFB) in Florida. He hopes to fulfill his commitment to the SMART scholarship by working for the Department of Defense for at least four years post-graduation. Nick and his wife are parents to a daughter and two sons, born in 2014, 2016, and 2020, respectively.

PUBLICATIONS

- *Photoflash and laser ignition of select high-nitrogen materials.* Combustion and Flame – May 2016 – N.N. De, N.R. Cummock, B.C. Tappan, I.E. Gunduz, & S.F. Son
- *Reactive flow modeling of small scale detonation failure experiments for a baseline non-ideal explosive.* Journal of Applied Physics – March 2016 – D.E. Kittell, N.R. Cummock, & S.F. Son
- *Relating a small-scale shock sensitivity experiment to large-scale failure diameter in an aluminized ammonium nitrate non-ideal explosive.* Combustion and Flame – May 2018 – N.R. Cummock, J.O. Mares, I.E. Gunduz, & S.F. Son
- *Characterization of thermally and mechanically insulted PBX 9501 using micro-computed tomography.* Proceedings of the 16^{th} International Detonation Symposium – July 2018 – N.R. Cummock, C.G. Rumchik, & S.F. Son
- *The effect of the chosen distribution form on reaction probability estimates from drop-weight impact results.* Journal of Energetic Materials – August 2020 – N.R. Cummock, A.D. Casey, & S.F. Son
- *The influence of microstructure and conformational polymorph on the drop-weight impact sensitivity of δ-phase HMX.* **Accepted with minor revisions** Journal of Energetic Materials – December 2020 – N.R. Cummock, J.R. Lawrence, M. Örnek, & S.F. Son
- *The influence of microstructure and conformational polymorph on the shock sensitivity of δ-phase HMX.* **In preparation** – November 2020 – N.R. Cummock, J.R. Lawrence, C.J. Blum-Sorensen, V.S. Vuppuluri, & S.F. Son